Mirihana Arachchige Dona, Kalpani Anuradha (2023) ***Experimental and theoretical investigations of plasma liquid interactions.*** **Masters (Research) Thesis, James Cook University.**

https://doi.org/10.25903/qhpq%2Dt425

Experimental and Theoretical Investigations of Plasma Liquid Interactions

A Thesis submitted by

Kalpani Anuradha Mirihana Arachchige Dona
BSc (Hons)

in November (2023)

for the degree of Master of Philosophy

in the College of Science & Engineering

James Cook University

Statement of the Contribution

Apart from individual contributions mentioned in the acknowledgements, there have been several significant organizations or groups that have made direct contributions in support of this thesis.

Nature of Assistance	**Contribution**	**Names, Titles, and Affiliations of Co-Contributors**
Financial Support	Fee offset/waiver	James Cook University
	Travel bursary and sponsorship for attending conferences and training	College of Science and Engineering, James Cook University The Association of Molecular Modellers of Australasia (AMMA)
Laboratory experimental conduction and data collection	Technical assistance for experimental setup and instrument handling, and maintenance and/or sample collection	Prof. Mohan Jacob A/Prof. George Venomous Dr. Yang Liu Dr. Mark Barnes Dr. Dana Roberts Dr. Winnie Lie Alexander Guliza
Intellectual Support	Proposal writing, data analysis and editorial assistance	Prof. Ronald White A/Prof. George Venomous Dr. Gregory Boyle Dr. Yang Liu

Statement of access

I, the undersigned, the author of this thesis, understand that James Cook University will make this thesis available for use within the university library and allow access to other approved libraries after its submission. All users consulting this thesis will have to sign the following statement:

> In consulting this thesis, I agree not to copy or closely paraphrase it in whole or in part without the written consent of the author; and to make proper public written acknowledgment for any assistance which I have obtained from it.

Beyond this, I do not wish to place any restrictions on access to this thesis.

……………………………………. ……………………………………..

(Kalpani Mirihana Arachchige Dona) Date

Sources declaration

I declare that this thesis is my own work and has not been submitted in any form for another degree or diploma at any university or other institute of tertiary education. Information derived from the published and unpublished work of others has been acknowledged in the text, and a list of references is given.

> Every reasonable effort has been made to gain permission and acknowledge the owners of copyright material. Any copyright owner who has been omitted or incorrectly acknowledged can contact the author.

Kalpani Mirihana Arachchige Dona

Acknowledgements

Firstly, I would like to express my immense gratitude to my supervisors, Professor Ronald White, Dr Gregory Boyle, Dr Yang Liu and A/Prof Daniel Kosov. Ron, your unwavering support, trust, and encouragement throughout my studies have been more than I could ever ask for. I am incredibly grateful for all you have done for me as a supervisor and the countless opportunities you've provided me. And Greg, I'm incredibly appreciative of the continued guidance you've offered me.

I would also like to thank my three unofficial supervisors, Professor Prof Mohan Jacob, A/Prof George Vamvounis and Dr Mark Barnes. Thank you for all our detailed discussions that have allowed me to learn much about experimental setups and microplastics. Your expertise, patience, and mentorship have made my master's research experience much easier to manage. Working alongside you has been an absolute pleasure, and I can't express how much I appreciate the time you have invested in me.

My thanks are also extended to the chemistry staff, in particular the efforts of Prof. Peter Junk and Dr. Murry Davis for all your support and assistance. And for all the Junk Group Members.

I would also like to thank Dr. Dana Roberts, Dr. Winnie Lee and Shiyoh Nobile for having an open door for me to come and do my analysis and for seemingly endless patience when I needed obscure chemicals and instruments. Some of the fondest memories I have made at JCU have been in the teaching labs and the prep room with you all.

I would also like to thank Ron's transport theory group members, past and present. Each of you has made coming into the lab each day such a pleasure, and I am grateful for the lifelong friendships I have made. An extraordinary mention goes to Dr Daniel Cocks and Dr Stephen Sanderson. You've provided me with an unparalleled amount of support through my MPhil, and I can't thank you enough for that.

To all my good friends, with special mentions to Vidushi Vithana, Thimira Jayasiri and Townsville family, thanks for the many ways that you have supported me across our friendship and during my studies, whether it be in the form of a place to stay when I visit, or a piece of advice, I'm grateful for you all, and all you've done for me.

To my family, I could not have asked for a more supportive, kind and encouraging.

To Pamitha Gunaratne, thank you for your endless kindness and patience. It has meant so much to me.

Finally, I would like to acknowledge the financial support of James Cook University.

Abstract

The accurate understanding of the transport properties of charged particles in dense gases, liquids, and soft condensed matter holds significant importance for numerous technological applications such as plasma technology, PET scans, dark matter detection, and water treatments and is a key focal point for fundamental physics research. Many of these applications depend on the interactions between the low-temperature plasma with a liquid. The plasma–liquid interface is a complex system requiring a deep understanding of the physical and chemical processes in multiple phases. In this pursuit, we set up a plasma-liquid setup based on previously published research work to investigate the intricate mechanisms governing physical and chemical reactions at the plasma-liquid interface. We provide experimental evidence that plasma electrons participate in electrolytic reactions, converting protons (H^+) to hydrogen gas.

The developed plasma liquid system was then used to treat synthetic monodispersed microplastic since microplastic pollution has been attracting significant attention because of its widespread presence in various environmental systems, its potential harm to ecosystems and aquatic life, and its ability to accumulate in the food chain. Removal of these plastics is therefore very important to mitigate these ecological and health risks. In this study, liquid plasma process was employed to evaluate its effectiveness on microplastic degradation. To that end, solution concentration, exposure time, and electrolyte type were investigated as a function of microplastic degradation using analytical techniques. It was found that the plasma-based process emerges as a promising technology for degrading polystyrene microplastics. These findings provide a foundation for future research and the development of sustainable strategies to address the global issue of microplastic pollution. However, it is important to note that further research is required to explore the scalability, cost-effectiveness, and environmental implications of plasma-based degradation techniques for microplastics.

Simulations of the electron transport in liquids is sought to complement experiments, and, as a step towards future models, molecular dynamics simulations were performed to investigate electron transport in nonpolar liquid mixtures. Despite limited experimental data available for pure non-polar liquids, an entirely satisfactory theoretical framework to explain their behaviour still needs to be discovered. In this study, our primary focus is on pure and binary mixtures of argon (Ar), krypton (Kr) and xenon (Xe). MD simulations have been executed to ascertain the RDF for these systems. Our results demonstrate a strong alignment with existing molecular dynamics data, crucially validating our simulation methodology. As a prospect for future research, we aim to formulate a comprehensive theoretical model capable of explaining existing experimental observations pertaining to the transport of charged particles within non-polar liquids. Furthermore, we intend to extend our investigations to encompass calculating transport properties for charged particles within biological systems.

List of publications and presentations

Publications

- **Journal Article**: Boyle, G. J., Garland, N. A., McEachran, R. P., **Mirihana, K. A**., Robson, R. E., Sullivan, J. P., & White, R. D. (2024). Electron scattering and transport in simple liquid mixtures. Journal of Physics B: Atomic, Molecular and Optical Physics, 57, 015202. doi:10.1088/1361-6455/ad1d35

Presentations:

- **Poster Presentation:** ‘Providing structure inputs to charged particle transport models of nonpolar liquids”, MM2023, 07-10 December 2023, University of Wollongong, NSW, Australia

- **Poster Presentation:** ‘’Radial distribution functions of noble liquid mixtures”, Workshop on Theory and Simulation of Nonequilibrium Fluids’’, 11-15 September 2023, The University of Queensland, QLD, Australia

- **Oral presentation:** “Microplastic Degradation using plasma-liquid interactions”, Higher Degree by Research (HDR) Engineering Conference 2022, College of Science and Engineering, James Cook University, Townsville, Queensland, Australia

Abbreviations

AC	Alternative current
Ar	Argon
ATR-FTIR	Attenuated Total Reflection Fourier Transform Infrared Spectroscopy
CAP	Cold Atmospheric Plasma
CPE	Capillary Plasma Electrode
DBD	Dielectric Barrier discharge
DC	Direct Current
DFT	Density Functional Theory
DNA	Deoxyribonucleic Acid
EDX	Energy-Dispersive X-ray spectroscopy
FDG	Fluorodeoxyglucose
FF	Force Field
FTIR	Fourier-Transform Infrared Spectroscopy
GPC	Gel Permeation Chromatography
GROMACS	Groningen Machine for Chemical Simulations
GROMOS	GROningen MOlecular Simulation
GTCS	Grand Total Cross Section
Kr	Krypton
LJ	Lennard-Jones
M	Molarity
mA	Mili Amperes
MC	Monte Carlo
MD	Molecular Dynamics
MHCD	Micro Hollow Cathode Discharge
MIC	Minimum Image Convention
min	Minutes
MP	Microplastic

MPs	Microplastics
Mw	Molecular Weight
Ne	Neon
NMR	Nuclear Magnetic Resonance
OPLS	Optimized Potential for Liquid Systems
PBC	Periodic Boundary Condition
PDI	Polydispersity Index
PE	Polyethylene
PET	Positron Emission Tomography
PP	Polypropylene
PS	Polystyrene
Pt	Platinum
PT	Pulsed Townsend
PVC	Polyvinyl Chloride
QM	Quantum Mechanical
RON	Reactive Oxygen and Nitrogen
ROS	Reactive Oxygen Species
SEC	Size Exclusion Chromatography
SEM	Scanning Electron Microscopy
SI	Supplementary Information
SST	Steady State Townsend
TCS	Total Cross Section
TGA	Thermogravimetric Analyses
THF	Tetrahydrofuran
TIP4P	Model for water and its interactions
UV	Ultraviolet
Xe	Xenon
XPS	X-ray Photoelectron Spectroscopy
XRD	X-ray diffraction

Table of Contents

List of Figures

List of Tables

1

Introduction

1.1 Motivation and Aims

The accurate understanding of the transport properties of charged particles in dense gases, liquids, and soft condensed matter holds significant importance for numerous technological applications such as plasma technology, Positron Emission Tomography (PET) scans, dark matter detection, and water treatments and is a key focal point for fundamental physics research [2]. Many of these applications depend on the interactions between the low-temperature plasma with a liquid. The plasma–liquid interface is a complex system requiring a deep understanding of the physical and chemical processes in multiple phases.

The overarching objective of this thesis is to contribute to the understanding of charge particle transport phenomena occurring at the plasma-liquid interface. We experimentally investigate water electrolysis by plasma-liquid interactions, microplastic degradation using plasma-liquid interactions and then investigate the simulations of important structure effects, as a first step towards the development of models. By doing so, we aim to shed light on the underlying principles and mechanisms governing the behaviour of charged particles in this intricate environment. This thesis aspires to make a meaningful contribution to the interdisciplinary field, bridging physics, chemistry, and engineering while addressing the pressing challenges and opportunities presented by the plasma-liquid interface.

Investigate plasma-electrolytic mechanisms: The primary aim of this study is to delve into the intricate mechanisms governing physical and chemical reactions at the plasma-liquid interface. Specifically, we seek to understand how plasma electrons participate in electrolytic reactions, focusing on converting protons (H^+) to hydrogen gas. We aim to provide concrete evidence of this phenomenon through comprehensive experimental investigations by developing a plasma-liquid experimental setup.

Explore the applications of developed plasma-liquid setup: Building upon our understanding of plasma-liquid interactions, the next objective is to utilize the developed plasma electrolytic system to treat synthetic monodispersed microplastic suspensions. The aim is to assess the potential of this novel approach as an effective method for degrading microplastics in water. We will analyse and quantify the outcomes of this treatment process to evaluate its feasibility and efficacy.

Complement experiments with simulations: Our objective is to take the initial step in integrating structural effects into computational simulations, thereby augmenting our experimental findings. Our focus will be on understanding electron transport within the plasma-liquid interface, with an initial emphasis on structure factor calculation using radial distribution function. As a preliminary step towards future modelling efforts, molecular dynamics simulations will be conducted to investigate electron transport in nonpolar liquid mixtures. These simulations will deepen our theoretical understanding of the processes observed in experiments and may pave the way for more advanced models in the future.

1.2 Plasma

1.2.1 History and overview

Plasma consists of charged and neutral particles, which exhibit quasi-neutrality and collective behaviour, also named the fourth state of matter [3–5]. Almost 99% of the matter in the visible universe is in the plasma state. Plasma is produced through ionisation, with the atoms or molecules dissociated into electron’s positive and negative ions. Although there are free charges and ambipolar pairs in plasmas, positive and negative charges counterbalance each other, and hence, plasmas maintain quasi-neutrality [3]. A gas can be either completely ionised or weakly ionised. All particles have sufficient collisions at the same temperatures in the thermal equilibrium. The most common examples of thermal equilibrium plasma are arcs used in streetlamps and natural fusion reactors (the Sun) [3].

In low-temperature non-equilibrium plasmas, [6–8], the temperature of the heavy particles generally ranges from 300 K to 1000 K. However, the electron temperature can reach above 10,000 K to 50,000 K or 1 eV to 5 eV [4]. The power supplied to the plasmas prefers electrons. Therefore, the temperature of electrons is significantly higher than that of neutral ions. As a reason for the significant radiative de-excitation rate, the electron-induced de-excitation rate of the heavy particles is generally less than the corresponding electron-induced excitation rate [9]. Corona discharge [10] and glow discharge [11,12] are typical examples. Even though the electron has a high temperature, the kinetic energy of electrons is still low because of their small mass.

Low-temperature plasma can be divided into high-pressure plasmas and low-pressure plasmas. Generally, high-pressure plasma operates at pressures from above 100 Torr. Atmospheric pressure plasma is one of the widely used high-pressure plasma. In most low-temperature plasmas, the pressure varies from 1 mTorr to 1 Torr, and the corresponding electron density ranges from 10^8 to 10^{13} cm^{-3} [13]. A uniform plasma can be made in large volumes at low pressures. This production favours industrial applications like film deposition and wafer etching. Atmospheric plasmas have universal applications such as disinfection [14,15], surface functionalisation of materials [16,17], ozone production [18,19] and nanoparticle synthesis [20,21].

The dielectric barrier discharge (DBD) at atmospheric pressure is a broadly used type of atmospheric plasma [22–24]. The primary purpose of the dielectric barrier is to regulate the electric current and stop spark formation. Figure 1.1 shows the typical DBD configuration.

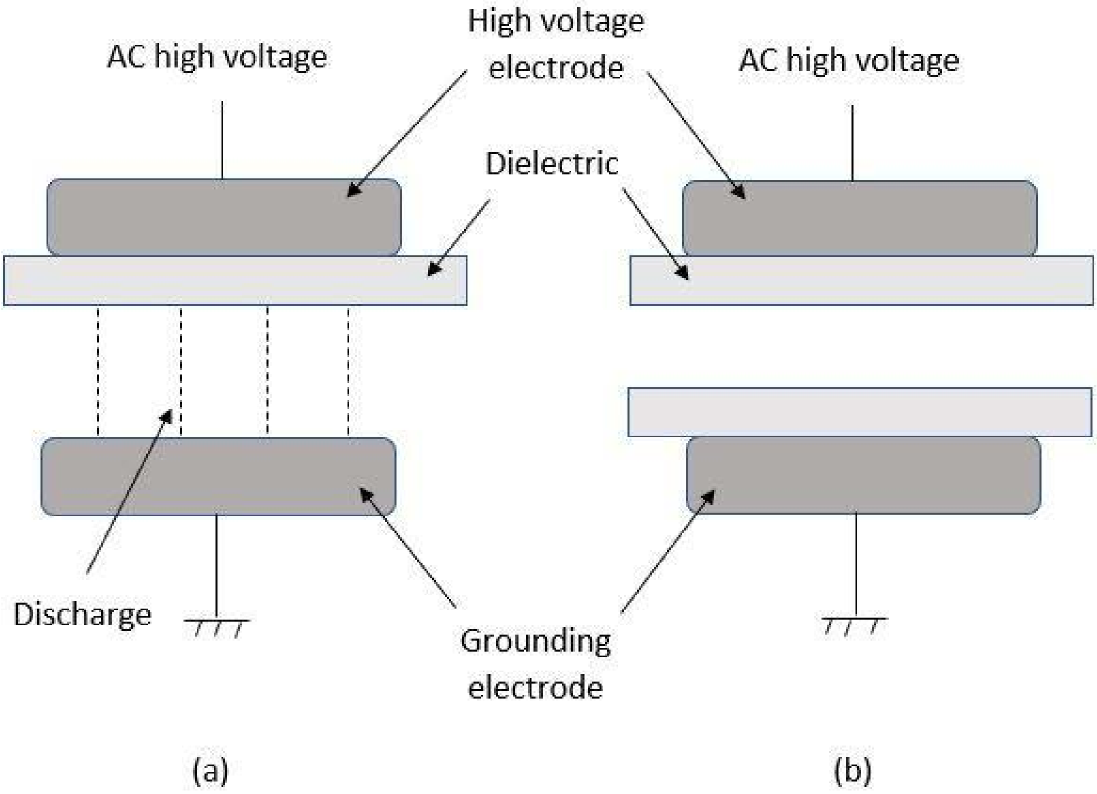

Figure 1.1: Typical DBD configuration. (a) DBD with one dielectric barrier covered the upper electrode and (b) with two dielectric barriers [22–24].

A typical DBD has one or more dielectric barriers between metal electrodes in the current path. The DB can be produced using glass, quartz, ceramics, water, or other materials with low dielectric loss and high breakdown strength. The gap between DBD usually ranges from 0.1 mm to 10 cm, and the driving frequencies are typically from 1 HZ to 10's MHz [22–24]. DBD are used to produce ozone (O_3) [25] and hydrocarbons [26,27], remove volatile organic and inorganic compounds [28,29], material processing [30–32] and as a UV/VUV photon source [33].

Generation of the non-thermal plasma at atmospheric pressure was a significant challenge for researchers [34] as the non-thermal glow discharge is very unstable. To counteract these issues, different approaches were taken by the researchers in designing the power system to limit the plasma duration to microseconds and, therefore, to reduce gas heating. Another method is to reduce the discharge diameter to the 100-micrometre range to increase the surface area to volume ratio and subsequently limit gas heating called micro plasma. Foest and colleagues [34] suggest it as a standard approach to non-thermal plasma production due to its relative simplicity in the generation method and its lesser limitations.

Schoenbach et al. [35] were the first to report a microdischarge's stable atmospheric pressure operation in a cylindrical hollow cathode geometry. These authors originated the term "micro hollow cathode discharge (MHCD)" for this type of micro discharge, which was subsequently used by several other groups [4,36–39]. Over the years, after several research studies, MHCD appeared in the late 1990s as a viable method to generate stable non-thermal atmospheric pressure plasmas. In MHCD, the anode and cathode are placed with a thin dielectric barrier layer between them. The hollow cathode has a small hole punctured through it. The anode is placed some distance from the hollow cathode where plasma is produced. Early experiments by Lan Yu and his team identified the possibility of creating stable plasma in atmospheric pressure Ar and Xe using a direct current power supply [37]. Due to a pendulum-like effect caused by the rapid movement of electrons between the walls of the micro hollow known as the "Pende" effect, hollow cathode discharge produces current densities that are orders of magnitude larger than what would be expected of a standard glow discharge [34]. Capillary plasma electrode (CPE) discharge is a modified version of the dielectric barrier discharge (DBD) operated via a pulsed DC or AC power source. In CPE discharge, the dielectric capillaries are placed on one or both electrodes of a discharge device. The capillaries, with diameters ranging from 0.01 to 1 mm and length-to-diameter ratios of 10:1, serve as plasma sources that produce jets of high-intensity plasma at atmospheric pressure under the correct operating conditions. The plasma jets emerge from the end of the capillary and form a “plasma electrode" for the primary discharge plasma. Under the right combination of capillary geometry, dielectric material, and exciting electric field, a steady state can be achieved [37].

Plasma electrochemistry refers to a system where one medium involved is plasma. Electrochemical systems show a charge transfer reaction through materials of different phases significant difference between non-thermal atmospheric plasma's electron temperature and the bulk material temperature allows electrochemical products to be formed at close to ambient temperatures, permitting the potential to overcome thermal limits on chemical reactions [40]. Other than that, it allows for electrochemical reactions to occur without the involvement of any solid materials [41] findings guided many studies on different applications like wastewater treatment [42,43] and nanomaterial synthesis [44,45].

1.2.2 Plasma – Liquid interactions

Most all plasma-based applications depend on chemical reactions initiated in the liquid phase by reactive species generated in the plasma phase, whose lifetimes vary greatly. Long-lived species include ozone (O_3) and various nitrogen oxides such as NO_2 and NO_3. On the other hand, short-lived species encompass oxygen atoms (O), superoxide radical anion ($O_2^- \bullet$), hydrogen atoms (H), hydroxyl radicals (•OH), and hydrated electrons ($e^-_{(aq)}$) [46]. These long-lived species can dissolve into water to drive oxidation reactions and change the solution environment by forming nitrous (HNO_2) and nitric acid (HNO_3). Shorter-lived species can be formed via plasma processes in the vapour above the water surface or via the bombardment of plasma species into the solution [46].

In addition to the chemical and physical interactions, the gas and liquid phases are coupled electrically through the motions of electrons and ions within the two phases and across the plasma-liquid interface. The exact scientific mechanism of electron transport across the plasma–liquid interface is poorly understood and has become a critical knowledge gap in the plasma field [47]. These knowledge gaps give rise to the number of research questions we focus on in this project. The project mainly focuses on understanding electrons' role across the plasma-liquid interface.

Plasma-liquid systems can be organised into three categories, as illustrated in Figure 1.2. The plasma can be generated with the liquid as a critical component of the plasma circuit, either by suspending the plasma electrode over the liquid surface or by submerging the electrode into the liquid. Both (a) and (b) processes are typically operated under direct current (DC) or pulsed DC conditions. In process (c), the plasma is generated 'remote' from the liquid, where the electrical circuit that forms the plasma is entirely independent of the liquid, and reactive species are introduced into the liquid primarily by advection and diffusion [46].

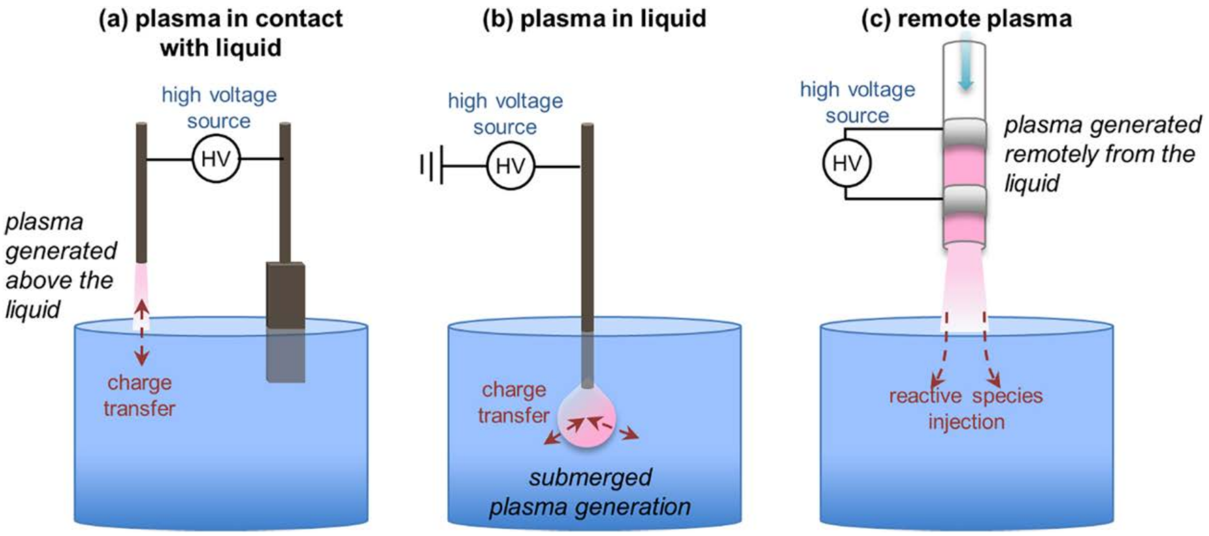

Figure 1.2: Schematics of three common strategies for plasma-liquid systems: (a) plasma generated in contact with the liquid (b) plasma generated in the liquid by a submerged electrode (c) remote plasma generated distinct from the liquid [46] .

When the plasma is in contact with the liquid configuration, the liquid itself plays an essential part in plasma generation by being a part of the plasma electrical circuit. Recent reviews have summarised the complex physics and various applications of plasmas-liquid interactions [8,48]. The solvated electron is a fascinating and highly reactive chemical species generated in the plasma phase, simple in many ways yet not completely understood [1]. Moreover, it is one of nature's most potent reducing agents. However, even today, open questions and scientific arguments exist about its basic structure and how it interacts with and arranges the surrounding solvent around itself. When a solvated electron is produced in a solvent such as water, it is referred to as a hydrated electron. Recently, hydrated electrons have been produced through a non-thermal atmospheric-pressure plasma contact with an aqueous solution [46]. The configuration depicted in Figure 1.2 (a) is directly related to my study. This specific plasma-liquid interface forms the basis for my research focus.

1.2.3 Applications

Plasma technology is an emerging field that addresses critical issues ranging from microbiology, biochemistry, biophysics, medicine, environmental applications, agriculture, and nanomaterials synthesis [8,42,49–51]. This is mainly due to the plasma's unique properties, easy access into the narrow spaces and potency to kill bacteria [52–55]. In recent years, low-temperature plasma (less than 40 ^{0}C), which still can drive plasma chemistry, has been developed. This Cold Atmospheric Plasma (CAP) has opened the door of plasma treatments to heat-sensitive objects.

In CAP, reactive oxygen and nitrogen (RON) species can react with biological targets for advantageous effects. Drug delivery and cancer treatment [56], plasma torches [57–60], plasma needles [55,61], inducement of blood coagulation [62], and contact-free sterilisation [48,50] are some of the intended applications of CAP. Researchers have paid considerable attention to the RONs and their effect on cells. However, the attention given to the role of electrons and positrons is very little, even with their importance in the applications mentioned above.

In our research, we investigated into the application of plasma-based techniques for the degradation of microplastics. Chapter 03 introduces a comprehensive literature review that synthesizes existing studies on the use of plasma-based approaches in addressing microplastic degradation within water treatment processes. This chapter aims to provide a thorough understanding of the current state of knowledge, highlighting key findings and methodologies employed in previous research endeavours. By examining the body of literature on plasma-based applications in microplastic degradation, we aim to identify gaps in knowledge, establish a foundation for our own investigation, and contribute to the evolving discourse on sustainable water treatment solutions.

The present need for water purification has surged due to increased pollution from industrial and agricultural activities, coupled with diminishing freshwater resources. Among the pollutants from industrial and agricultural sources, organic compounds represent a significant global concern, given their potential to substantially harm the environment and human health [63]. Nonetheless, traditional water treatment methods, encompassing sedimentation, filtration, and disinfection, do not specifically tackle eliminating organic compounds. Consequently, alternative advanced techniques are imperative for addressing organic pollutants and efficiently managing contaminants from chemical incidents or uncontrolled releases [64].

The seminal work of B.R. Locke and colleagues explored reactive species generated by plasma through point-plate discharges in contact with water [65–67]. In their experimental setups, the high-voltage electrode is submerged within the liquid medium, while the ground electrode is suspended above the liquid. This configuration generates significant quantities of short-lived radicals and hydrogen peroxide (H_2O_2) within the liquid phase, facilitating the removal of organic contaminants. Furthermore, the electrical discharge can also occur above the liquid's surface, which intensifies the production of active species and introduces ozone into an oxygen-enriched gas atmosphere, thereby enhancing the removal of contaminants by diffusion into the liquid phase. Consequently, hybrid gas-liquid reactors generally outperform both liquid discharge reactors and gas discharge reactors in the context of water treatment.

Artificial nitrogen fixation is crucial in agriculture and industry, particularly for ammonia production used in fertilizers. Current large-scale methods, such as the energy-intensive Haber-Bosch process, contribute significantly to greenhouse gas emissions [68,69]. Given the growing global population and the importance of on-site production, research focuses on low-energy approaches like plasma-based reactions to produce ammonia [70]. The H atoms of water molecules in the outermost surface of the water phase are directed towards the gas phase [71]. Researchers assumed that the discharged activated nitrogen species in the plasma gas phase tap H from water molecules exposed on the water surface, which eventually synthesised ammonia. Alternatively, activated nitrogen species can undergo an oxidation process to produce nitric acid.

1.2.4 Recent computational modelling of plasmas in contact with liquids

Developing precise computational models for plasmas interacting with liquids is paramount to comprehensively analyse experimental data in plasma-liquid interactions and evaluate the efficiency of different plasma–liquid setups. When considering the underlying physics, a notable challenge lies in comprehending the physical and chemical phenomena transpiring at the gas-liquid interface, where diagnostic techniques face limitations. Computational models are pivotal in bridging this knowledge gap, furnishing valuable insights into these interactions.

The intricacies of plasma-liquid interactions present a challenge for computational modelling due to the significant variations in both time and length scales, spanning from nanoseconds to minutes and from nanometres to centimetres [72–74].

Early on, various gas-phase models were developed to explore discharges with the inclusion of water vapour. A key focus was on ozone generation and its relationship with water, as well as hydrogen peroxide [75]. Peyrous [75] conducted a detailed investigation into the temporal evolution of O_3 and H_2O_2 through kinetic simulations of corona discharges, comparing and discussing the outcomes for dry and humid air. Notably, the presence of water vapour substantially augmented the density of H_2O_2, and humidity and temperature exhibited cumulative effects on O_3 production, reaching a saturation point during multiple pulses.

As plasma jets find extensive applications in interactions with liquids, a growing body of computational research has focused on modelling these plasma jets. For instance, Sakiyama and Graves [76] devised a 2-D model employing finite element analysis to simulate a plasma jet operating in a helium environment with trace amounts of nitrogen gas. Their study delved into the transition between the corona and glow modes of the discharge. Subsequently, they developed a 1-D plug-flow model to simulate a surface micro-discharge into the humid air, incorporating more than 50 species and 600 reactions [77]. Another comprehensive global plug-flow model, featuring over 2,000 reactions, was formulated by Gaens and Bogaerts [78] to represent an Ar plasma jet.

On the other hand, Norberg and Kushner [79] employed a 2-D fluid model to investigate the dynamics of plasma jets and the resultant plasma-produced species. Their research explored the impact of gas flow rates on these plasma-produced species, revealing a noticeable reduction in ozone density at higher flow rates. These models thoroughly examined plasma characteristics with diverse chemical reaction mechanisms, which can be applied across various discharge conditions.

The emerging challenge pertains to modelling interactions between plasmas and liquids, particularly at gas-liquid interfaces. Only a limited number of computational investigations have directly addressed these interactions. For instance, Babaeva and Kushner conducted computational analyses to explore the energy and angular distribution of ions impacting polymer surfaces, delivered by dielectric barrier discharges in air, employing a 2-D fluid model [80]. Norberg and Kushner undertook modelling endeavours to study the interactions of plasma jets with liquid surfaces in both remote and contact modes [81]. Liu, Kong, et al. developed a semi-1-D model to investigate interactions between plasma and biofilm or plasma and tissue. When modelling biofilm and tissue interactions, they introduced a reactive penetration model to describe the mass transfer of highly transient plasma species across the gas-liquid boundary. This model can be further integrated into molecular dynamics simulations. A few models have also focused on electric discharges directly occurring within liquids [82]. Such discharges often operate at high power levels, typically in the range of tens to hundreds of kilovolts and may involve or not involve arc-like sparks, leading to phase changes, shock waves, and the emission of UV light. The intricate coupling of physical phenomena with chemical reactions in these systems remains a complex and relatively underdeveloped study area.

1.3 Molecular Dynamics Simulation

1.3.1 History and Overview

Computational techniques are widely used to model complex molecular systems and are intensively applied in studying biochemical and biophysical processes in living organisms [83]. These techniques allow researchers to learn about molecular methods and onerous or paradoxical consequences to investigate experimentally. The main objective of computer simulations of molecular systems is to compute macroscopic behaviour from microscopic interactions [84]. This recent advancement in computer technologies gives rise to many advantages, such as multiscale modelling, which can decrease product development time by lessening costly trial-and-error iterations and reducing the number of expensive large-systems scale experiments. Multiscale modelling can help develop new materials and support medical practice in making diagnostic and prognostic evaluations related to the human body [85].

Alder and Wainwright made the first move in the molecular dynamics (MD) simulation method using hard 2D disks [86,87]. In 1960, Gibson and his team used MD techniques to study the damage of a copper crystal lattice by high-energy radiation [88]. Aneesur Rahman is often credited as the father of the MD simulation. This title is justified due to his contribution to methodology and elevated the use of MD simulation in the scientific field [84]. In 1964, Rahman simulated the behavior of liquid Ar interacting with a Lennard-

Jones potential and subsequently analyzed a range of its properties [89]. During the 1970s, Rahman and his team studied liquid water [90] and superionic conductor α-AgI [91].

1.3.2 Introduction to MD Methodology

Molecular simulations provide a way to generate thermodynamic data sets without any experimental contribution. The Molecular Dynamics (MD) and the Monte Carlo (MC) techniques are the two main approaches to such computer experiments. Monte Carlo (MC) simulation method involves the exploration of the energy surface by randomly probing the configuration space. This simulation method generates system configurations by applying random displacements to the species' positions. The number of molecules, the system's volume, and the system's temperature are constant [92].

In recent years, MD simulation has become an important and effective method for studying biomolecules. Unlike other experimental methods, such as NMR or X-ray diffraction, which only provide static images of molecules, MD can accurately capture the highly dynamic nature of biological molecules. This is primarily due to improvements in the accuracy of force fields, which are the models used to describe the interactions between molecules, as well as advancements in hardware and algorithms that have led to faster simulation times that better mimic real-life biological events [93].

In contrast to MC simulations, MD simulation is based on an exact time evaluation of the dynamic behaviour of a molecular system. In this method, successive configurations of the system are generated by integrating Newton's equations of motion (the atoms are treated like hard balls, and Newton's laws describe their motions) which results in trajectories that specify how the positions and velocities of the particles in the system change with time, typically in the nanosecond time scale [84].

Selecting a realistic and computationally efficient potential energy function E is essential for calculating the force exerted on each atom in MD simulation. A frequently employed version of this function is:

$$E(R) = \frac{1}{2} \sum_{bonds} K_b \, (b - b_0)^2$$

$$+\frac{1}{2}\sum_{bond\ angles} K_\theta\,(\theta-\theta_0)^2$$

$$+\frac{1}{2}\sum_{torsional} K_p([1+\cos(np-\delta)])$$

$$+\sum_{nb\ pairs}\left(\frac{A}{r^{12}}-\frac{B}{r^{6}}+\frac{q_1q_2}{Dr}\right) \qquad \text{Equation 1.1}$$

The above equation considers the interaction between molecules and within molecules. Intermolecular forces pertain to the attraction between non-bonded molecules, which arise from the electrostatic field generated by their protons and electrons. On the other hand, intramolecular forces occur within molecules and restrict the independent movement of bonded atoms. This potential energy function encompasses various phenomena within these two types of interactions.

Equation 1.1 comprises four sums; the first three sums illustrate the direct atomic bond interactions, while the fourth sum accounts for non-bonded intramolecular and intermolecular interactions like electrostatic and van der Waals interactions. These interactions vary with position $R \equiv (r_1, r_2, r_3, \ldots\ldots, r_N)$. The first sum, governed by Hooke's law harmonic potential, measures the deviation from the equilibrium bond length (b_0) with bond force constant (K_b) and instantaneous bond length by (b). The second term in the Equation represents the energy resulting from the perturbation of bond angles from the equilibrium angle (θ_0), where (K_θ) and (θ) are force constant and angle, respectively. The third term accounts for rotations around bonds and is a periodic potential that takes the form of a cosine function with parameters (n), (δ) and (ρ) representing multiplicity, phase difference, and torsion angle, respectively.

The energy contribution of non-bonded van der Waals interactions and electrostatic interactions between two atoms with charges q_1 and q_2 and separated by an interatomic distance r, described respectively by Lennard Jones and Coulomb potentials, are included in the final term, which is summed over all atoms. The dielectric constant (D) is also considered in this calculation.

The Lennard-Jones (LJ) potential accommodates two phenomena:

1. Van der Waals interactions, which arise at moderate distances.
2. Repulsion, a phenomenon that occurs if two atoms approach so closely that their electron shells overlap.

The Lennard-Jones potential (V_{LJ}) between two atoms is defined as:

$$V_{LJ}(r_{ij}) = \frac{C_{ij}^{(12)}}{r_{ij}^{12}} - \frac{C_{ij}^{(6)}}{r_{ij}^{6}} \qquad \text{Equation 1.2}$$

In the equation 1.2 the parameters $C_{ij}^{(12)}$ and $C_{ij}^{(6)}$depend on pairs of atom types obtained from a matrix of LJ parameters. Additional details and the derivation of this equation can be found in Appendix C of this thesis.

After selecting the potential energy function and establishing an excellent initial conformation through experimental or theoretical means, one can initiate a dynamic simulation. Initial velocities are obtained from a Maxwellian distribution based on the temperature. Newton's law of motion is used to determine the acceleration (a_i) of atom (i) by considering its atomic mass (m_i) and the force (F_i) derived from the of Equation 1.1 concerning the atom's present position and the positions of its neighbouring atoms [94]. Newton's Equation of motion can be integrated using various algorithms, but the simplest and often most effective is known as the Verlet algorithm [95,96]. The new position of the atom (r_i) at the new time $(t + \Delta t)$ is computed using a Taylor expansion of the coordinate (r) in both forward and backward directions in time can be represented as follows.

$$r_i(t + \Delta t) = r_i(t) + v_i \Delta t + \frac{1}{2} a_i(t) \Delta t^2 + \frac{\Delta t^3}{3!} \dddot{r}_i + O(\Delta t^4) \qquad \text{Equation 1.3}$$

and

$$r_i(t-\Delta t) = r_i(t) - v_i\Delta t + \frac{1}{2}a_i(t)\Delta t^2 - \frac{\Delta t^3}{3!}\dddot{r_i} + O(\Delta t^4) \qquad \text{Equation 1.4}$$

Summed up, this results in

$$r_i(t+\Delta t) + r_i(t-\Delta t) = 2r_i(t) + a_i(t)(\Delta t)^2 + O(\Delta t^4) \qquad \text{Equation 1.5}$$

or

$$r_i(t+\Delta t) \approx 2r_i(t) - r_i(t-\Delta t) + a_i(t)\Delta t^2 \qquad \text{Equation 1.6}$$

As a result of the integration of Newton's law of motion, the acceleration is determined by the following Equation in which the force (F_i) is dependent on the position $r_i(t)$ and is derived from the potential energy function [95].

$$a_i(t) = -\frac{1}{m}F_i\big(r_1(t), r_2(t), \dots, r_N(t)\big) \qquad \text{Equation 1.7}$$

We can determine the system's behaviour over time by integrating these equations for all atoms in the system at each time step [94].

Our simulations employed the isobaric-isothermal ensemble, also known as the constant-NPT ensemble. This ensemble maintains a constant number of atoms (N), pressure (p), and temperature (T) while allowing the total energy (E) and volume (V) to fluctuate around the thermal equilibrium. This ensemble is widely used as it resembles real experimental conditions [95]. A Berendsen thermostat was utilised to maintain a constant temperature, which weakly couples the system to an external bath set at the desired temperature [97]. This process involves rescaling the atom velocities to adjust the force and achieve the desired temperature (T_0).

$$m_i\dot{v}_i = F_i + m_i\gamma\left(\frac{T_0}{T} - 1\right)v_i \qquad \text{Equation 1.8}$$

The value of the coupling's strength is determined by the damping constant γ, which is defined as

$$\gamma = 1 + \frac{\Delta t}{2\tau_t}\left(\frac{T_0}{T} - 1\right) \qquad \text{Equation 1.9}$$

In Equation 1.8, we can observe the altered equation of motion, where the velocities of the atoms (υ_i) are rescaled in direct proportion to (γv_i) with a time constant of τ_t [97].

To simplify the simulation process and improve computational efficiency, certain simplifications and considerations are often made. The equations of motion for each atom can be computed using Taylor series approximations for velocity and position. This approach involves discretisation and solving the equations step-by-step in time. This method allows for easy parallelisation of the computation process, where each sampling point can be independently processed. However, after each step, the updated positions of all atoms need to be combined to calculate the new potential energy function. This computational strategy is commonly known as the *leap-frog* or *Verlet* algorithms.

In MD simulations system will not model a liquid in a simulation box since molecules cannot move freely. If the molecules move freely, some will leave the simulation box, resulting in a density fluctuation. To overcome these problems, the following methods were used.

1. Minimum image convention (MIC)
2. Periodic boundary condition (PBC)

To apply the above two methods, it is considered that identical images of the simulation box surround the simulation box.

In the MIC method, when calculating intermolecular interactions between two molecules or atoms as illustrated in Figure 1.3, "i" and "j", the distance between molecules/atoms i and j and the distance between molecule i and all the images of j (j` s) were considered respectively, and the shortest distance is taken to calculate the interaction between molecule i and j. Using this convention, the boundaries of the original simulation box are ignored. So now it appears that molecules can move freely through the box's boundaries. As visualised in the Figure 1.3 $r' < r''$, i.e. interaction is calculated through the periodic boundary.

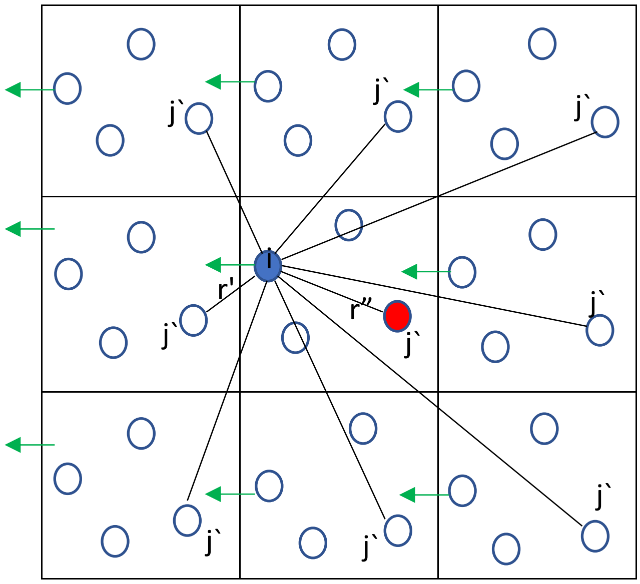

Figure 1.3: Schematic depicting MIC method in molecular dynamics. Molecules "i" and "j" within simulation box. Shortest distance (solid line) used for interaction calculation, ignoring box boundaries. Arrows denote unrestricted movement. r^' < r^" indicates periodic boundary interactions.

Due to the free movement of molecules, consider one molecule is moving out of the simulation cell through one face of the box. Then, its image in the adjacent box will move into the simulation box from the opposite direction with the same velocity and directions as before which we called as the periodic boundary condition. Therefore, the number of molecules in the simulation box will be constant, thus keeping the constant density throughout the simulation.

1.3.3 Limitations of Molecular Dynamics Simulation

While molecular dynamics has achieved broad utilization and notable achievements, it confronts inherent limitations. In the realm of simulations, there exist two primary hurdles: the precision of existing force field models and the constraint on simulation duration, which is presently confined to around one microsecond due to the substantial computational resources required [98].

It is essential to recognize that force field parameters, encompassing factors like partial charges, van der Waals interactions, and bond/angle values, are primarily derived through empirical methods, drawing from either experimental spectroscopy or quantum mechanical (QM) calculations. These parameters are inherently approximations rather than exact representations, thus introducing potential inaccuracies into simulation results. Force fields serve as only an approximation of the intricate quantum mechanical reality, demanding further refinement to faithfully capture the behavior of macromolecules, especially when quantum effects exert significant influence. This challenge can be mitigated by integrating quantum mechanical elements into the force fields, particularly for specific system components, as demonstrated, for instance, by Hong et al. [99]. Moreover, recent efforts have focused on the development of novel and enhanced force fields, characterized by more extensive validation against experimental data. Consequently, the choice of an appropriate force field tailored to the specific application becomes pivotal to faithfully replicate molecular behavior under the simulated conditions [93].

A notable aspect currently absent from most simulations is electron polarization. In conventional practice, charges assigned to atoms remain static and are typically centered on the atoms themselves. However, electron clouds exhibit flexibility, continuously adapting their positions among bonded atoms in response to their environmental context. Although efforts have been devoted to crafting polarizable force fields [100,101], their widespread application and success have thus far been limited. Nonetheless, the ongoing endeavors in this direction hold promise for enhancing the accuracy of simulations in the future [98,102].

The computational demands associated with molecular simulations often impose limitations on simulation time, potentially leading to inadequate conformational sampling. This limitation, in turn, may yield non-representative results and restrict access to specific states due to the presence of high energy barriers. A fundamental issue arises from the fact that the accessible time scale in simulations is typically orders of magnitude shorter than the time frame in which most significant biological events occur—typically spanning microseconds to milliseconds.

Addressing this challenge can take two principal approaches. First, it is possible to lower the energy barriers for specific events, such as facilitating protein unfolding through the application of exceptionally high temperatures [103]. Alternatively, advancements in specialized hardware, like the dedicated parallel supercomputer, offer the potential to expedite molecular simulations and extend their time scale. For instance, supercomputers allow classical molecular dynamics simulations to operate on a millisecond-scale. With the extension of simulation time, the likelihood of sampling rare events increases significantly.

This extended time scale for simulations empowers researchers to delve into a broad spectrum of biochemical phenomena at the atomic level. This includes in-depth exploration of phenomena such as protein-protein interactions, structural alterations driven by functional changes, and the intricate process of protein folding [104].

The integration of equations of motion for interacting atoms within a MD program is accomplished through a time integration algorithm, which relies on finite difference methods. This integration takes place in discrete time steps, denoted as Δt. The outcome of each iteration yields approximations, which inherently carry a certain level of error stemming from factors like truncation of Taylor expansions, rounding-off errors in computational procedures, or specified cutoffs for non-bonded interactions. While the magnitude of these errors can be diminished by selecting a smaller time step Δt, it is essential to recognize that this decision invariably entails a trade-off between the precision of the calculation and the speed or duration of the simulation [105].

Furthermore, a successful simulation hinges on the availability of a high-quality starting model, the theoretical underpinnings of which must undergo rigorous validation. It is crucial to emphasize that only a starting model of the highest quality can yield dependable results in a simulation. Despite the acknowledged limitations, the sheer number and accomplishments of molecular dynamics simulations to date underscore their pivotal role in modern structural biology. Ongoing research efforts and solutions aimed at addressing these challenges, both presently and in the future, exhibit significant progress toward overcoming these constraints [98].

1.4 Structure of the thesis

Chapter 02 presents the significant findings and experimental results about the capacity of atmospheric-pressure micro plasmas to instigate and regulate electron-transfer reactions within aqueous solutions. Our research, inspired by the work of Witzke and colleagues [1,106], highlights the significant influence of atmospheric-pressure micro plasmas on electron dynamics in liquid environments.

Chapter 03 addresses the pressing contemporary concern of microplastic (MP) pollution within aqueous environments. A systematic exploration of an innovative approach that deploys a liquid plasma system to address this formidable environmental challenge. We commence with a introduction to the burgeoning issue of microplastic pollution within aqueous domains. Further, this section examines the multifarious factors influencing microplastic degradation. Factors of particular interest include the nature of the electrolyte employed and the temporal duration of the treatment. A rigorous analytical investigation provides insight into the resultant morphological and crystalline changes observed in polystyrene microplastics (PS-MPs) following the degradation process. Employing an array of analytical techniques, including microscopy and Fourier-transform infrared spectroscopy, we substantiate the transformative journey of microplastics into smaller particulate forms and their eventual conversion into gaseous constituents. The chapter culminates in a holistic assessment of the nascent field of plasma-liquid interactions as a potent method for ameliorating MP pollution in aqueous milieus. It posits this novel approach as a promising avenue for effectively mitigating MP contamination in water bodies.

In Chapter 04, we explore the complex interactions between plasma and liquid, with a specific focus on understanding the transport properties of charged particles using structure factor calculations, particularly electrons, in this intricate process. Recognizing the inherent complexity of these phenomena, we initiate our inquiry by addressing the theoretical side. Initially, we embark on a theoretical study, starting with calculating microscopic inputs. These inputs serve as the building blocks for our subsequent efforts. Our primary focus is developing charge particle transport models tailored to nonpolar liquids. In doing so, we endeavour to unravel the intricate transport properties of electrons within nonpolar pure liquids and liquid mixtures. This theoretical groundwork contributes to advancing our understanding of how charged particles navigate and influence the behaviours of both plasma and nonpolar liquids, forming the basis for future exploration into plasma-liquid interactions and microplastic degradation in previous chapters of this thesis.

2

Development of a Plasma-Liquid Setup

This work presents setting up a plasma-liquid setup based on previously published research works [1,107] and the details regarding the behaviour of the developed system. We provide experimental evidence that plasma electrons participate in electrolytic reactions, converting protons (H^+) to hydrogen gas. This is confirmed by pH measurements, which indicate an increase in basicity. These discoveries provide valuable insights into the fundamental involvement of plasma electrons in interactions between plasma and liquid, carrying significant implications for diverse applications, including plasma medicine and plasma-liquid materials synthesis.

2.1 Introduction

Electrochemical systems involve exchanging charges between different phases, particularly at the interfaces of solid and liquid components. In a typical electrochemical cell, a pair of metallic electrodes are positioned apart, with an electrolyte present to facilitate the conduction of ions in an aqueous solution [108]. The presence of an electric potential difference between the electrodes triggers charge-transfer reactions at the interfaces where the metal electrodes interact with the ionic electrolyte. However, electrochemical reactions are not restricted solely to the interfaces between solid metals and liquids. Insulating materials, for instance, can acquire a charge through contact electrification and serve as independent electrodes to induce various charge-transfer reactions in a solution. These reactions may encompass processes such as the generation of hydrogen gas and the deposition of metals. There have been limited investigations in this area [109–111]. The research conducted by Gubkin in 1887 investigated the concept of gaseous electrodes, where the transfer of charge to an electrolyte occurs through an electrical discharge known as plasma [112–114]. Despite having a long historical background, there is a minimal understanding of the fundamental aspects of charge-transfer reactions at the interface between a plasma and a liquid.

Plasmas are typically operated at pressures below the atmospheric level, which has constrained previous studies to solvents with exceedingly low vapour pressures, such as ionic liquids and polymers [115]. Furthermore, the complex circumstances within a plasma, characterized by elements such as ultraviolet radiation, radicals, electrons, and ions, give rise to non-Faradaic processes that challenge discerning and characterizing charge-transfer reactions with clarity [116–118].

This study is about the charge-transfer reactions at the plasma-liquid interface, an area of interest for various technological applications, such as water purification, food preservation, nanomaterial synthesis, plasma medicine, and power transformers for high voltage switching [119–127]. One aspect of interest is initiating electrochemical reactions using gaseous electrodes [128–130]. This is significant because traditional electrodes made of metals like Pt are expensive and limited in supply. As a result, there has been growing interest in finding alternative approaches that eliminate or reduce the reliance on such materials. Plasma-assisted electrochemistry offers potential advantages in terms of cost, availability, and mitigation of electrode fouling.

There remains a necessity to gain a comprehensive understanding of the mechanisms underlying the interaction between gas-phase electrons and ions within a solution at the interface between plasma and liquid. This holds particular significance when considering the distinctions from traditional electrochemical systems that involve metal electrodes. In conventional electrochemical systems, the charge transfer between the electrode surface and the electrolyte occurs through direct contact between the metal electrode and the solution. This interface involves adsorption, desorption, and diffusion of ions and electron transfer across the electrode-electrolyte interface [131,132].

The literature has documented the existence of plasmas in liquids since the late 19th century [112,133]. However, recent advancements in non-equilibrium, atmospheric-pressure plasmas, also known as cold plasmas, have made it easier to conduct experiments with liquids [134–136]. As a result, there has been a growing interest in this scientific field. Plasmas contain highly energetic species, including electrons, ions, radicals, photons, and hot gases. These species can react at or near the surface of wet electrodes. For example, there have been numerous studies on reactive oxygen species (ROS) generated in plasmas operating in the air and their effects on biological materials [137–139]. However, the influence of plasma electrons on solutions is not as well understood.

Electrons have the potential to become solvated within a solution and initiate intricate reactions either on its surface or throughout its bulk. Plasma electrons can engage in different kinds of reactions when present in a solution. Firstly, the exchange of electrical charge between the plasma and the solution can trigger electrolytic reactions [140], like the conventional electrochemistry that employs solid metal electrodes. Another possibility is that electrons can directly break apart molecules like water through electron-impact dissociation [141–144]. In most experiments, the discharge has been operated as the anode, resulting in the direction of energetic gas ions into the liquid instead of electrons. This leads to distinct chemical phenomena. In contrast, other experiments involve immersing the electrodes in water, causing water vapour in the plasma. In such instances, the reactions primarily occur under the influence of gas-phase mechanisms, which have been extensively studied and documented in the literature [145]. To study the influence of plasma electrons on reactions that occur within a solution in this study, we developed an electrochemical setup utilizing an atmospheric pressure microplasma as the cathode to investigate the impact of plasma electrons on reactions in solution. This microplasma is generated at the surface of an aqueous solution. Charge transfer reactions were initiated at the plasma/liquid interface by directing plasma electrons towards the solution surface. In previous works, Richmonds and team employed this method to examine the reduction of ferricyanide [$Fe(CN)_3^{-6}$] to ferrocyanide [$Fe(CN)_4^{-6}$], a model electrochemical reaction [106].

In conventional electrochemical systems, water electrolysis commonly occurs at elevated potentials, splitting water molecules into hydrogen and oxygen gas at the cathode and anode, respectively. In acidic environments, the process of water electrolysis involves two primary reactions:

Reduction at the cathode:

$$2H^{+}_{(aq)} + 2e^{-} \rightarrow H_{2(g)} \qquad \text{Equation 2.1}$$

And oxidation at the anode:

$$2H_2O_{(l)} \rightarrow O_{2(g)} + 4H^{+}{}_{(aq)} + 4e^{-} \qquad \text{Equation 2.2}$$

Our study demonstrates the capability of plasmas to electrolyse water through the reactions mentioned above. The reactions were investigated by monitoring changes in the pH of the solution. To effectively observe electrochemical reaction, we employed a split cell configuration that separates the cathodic and anodic reactions. Additionally, spatial, and temporal variations in pH were visualized by introducing an indicator that is responsive to pH changes into our experimental setup. While this research shares similarities with the study conducted by Witzke et al., [1], the focus of this experiment was to characterize our plasma–electrochemical setup precisely before applying this to complex aqueous systems, which will be discussed in the next chapter.

2.2 Experimental Section

2.2.1 Materials

Materials and solvents were obtained from the following suppliers, and all the solutions were used as received: Hydrochloric acid (HCl, Unichrom), universal indicator solution (pH 3 – 11, Chem-supply). All the solutions were prepared using ultra-pure water (Resistivity – 18.2 megaohm). A Pt counter electrode made with Pt wire (length: 70 mm, electrode diameter 0.5 mm) was used as a counter electrode. A stainless-steel needle which was prepared at the James Cook University (JCU) mechanical workshop used to ignite the plasma. The salt bridge was made using a Whatman 1, 18.5 cm filter paper. After every experiment, the needle was cleaned by polishing the outside surface with sanding sheets of 800 grits (IRWIN). The power was obtained by an extra high voltage power supply (Industrial Equipment & Control PTY. Ltd., 6000V. DC. 3mA. Max.). The pH measurements were taken by using a digital pH meter (AQUApHz).

2.2.2 Experimental Setup

Plasma-electrochemical reactions were carried out in opened glass cell configurations schematically depicted in Figure 2.1. The setup included a split glass cell with a salt bridge that prevented mixing the electrolytes on the cathodic and anodic sides. The utilization of a split cell configuration was necessary for accurately measuring the local pH change. This is because in water electrolysis, there is no overall (global) change in the pH of the entire system. The split cell arrangement allowed for quantitative measurement of the pH change specifically in the vicinity of the electrode reactions, providing localized information about the electrolysis process. All the experiments were performed at room temperature using a constant discharge current (3 mA). Using a laboratory stand, a stainless-steel needle was positioned

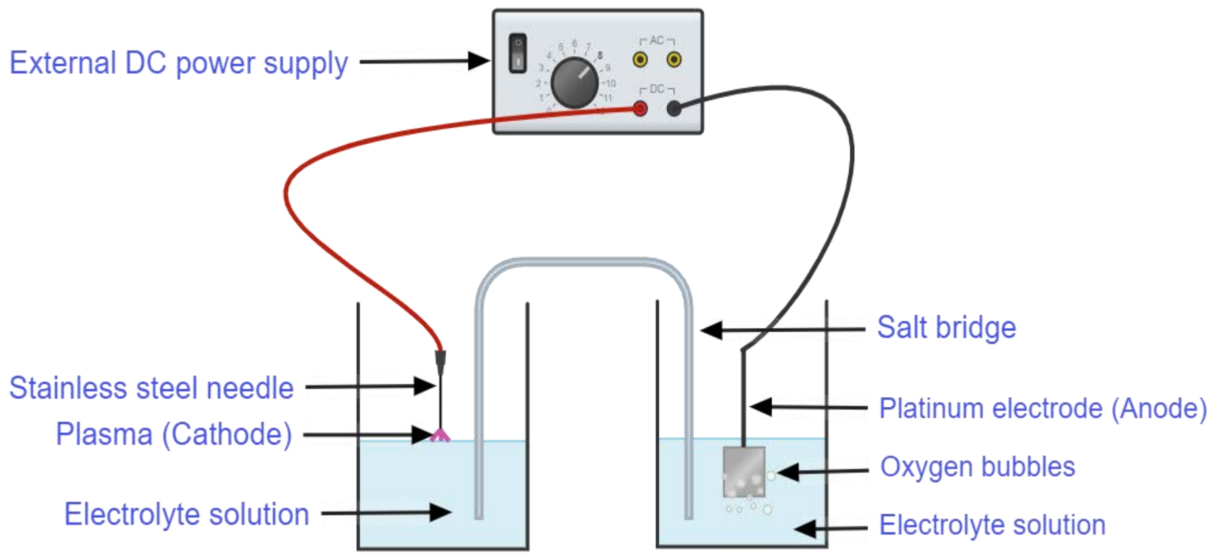

Figure 2.1: Illustration of the electrochemical configuration with a plasma cathode and Pt anode.

approximately 1 mm and 3 mm away from the electrolyte's surface on the cathode side. The anode was constituted by immersing a Pt foil into the solution. A DC power supply was connected to the experimental set-up, as illustrated in Figure 2.1.

To investigate water electrolysis, we created a microplasma by utilizing acidic solutions with suitable conductivity for electric current to flow. The solutions were prepared using MiliQ water, along with $1.0\,mM$ hydrochloric acid (HCl) and $1.0\,M\,KCl$ was included in the solution to maintain conductivity while reducing the concentration of H^+ ions. We employed two different methods to characterize water electrolysis: Firstly, we measured the pH in the cathode bath using a digital pH meter, after subjecting the cell to a constant discharge current for a specific duration. Secondly, we utilized a pH-sensitive dye called universal indicator and an iPhone 14 Pro camera to capture the images of pH changes after the operation of the cell similar to the method described by Go et al., [107].

The processing parameters, including the processing time duration, the distance between the plasma discharge needle tip, the electrolyte solution's surface, and the electrolyte solution's volume, were determined based on discussions in the existing literature and practical considerations [1]. All the experiments were conducted at room temperature.

2.2.3 pH measurements

In the initial experimental series, the catholyte and anolyte employed were 1 mM HCl and 0.1 M KCl, respectively. These electrolyte solutions were prepared in 15 mL of deionized water. The primary objective of this series was to explore the optimal value for the distance between the needle tip and the electrolyte's surface on the cathode side. Subsequently, a second experimental series was conducted, utilizing an electrolyte solution volume of 180 mL. This second series aimed to investigate the influence of the electrolyte solution volume on the plasma-induced changes in pH.

The initial pH of the solution was approximately 3.0, and the exact pH was recorded for each experiment. (Raw data presented in Tables S2.1, S2.2 and S2.3 of SI – APPENDIX A). Experiments were run for time increments between 2 and 30 min. The catholyte and anolyte were collected at each experiment's end, and the pH was measured. After every experiment, the needle was cleaned by polishing the outside surface with sandpaper and sonicating it in acetone. The Pt anode was also cleaned using acetone after every experiment.

The pH of the solutions before and after was measured using a digital pH meter (AQUApHz Rev3.1). The number of hydrogen ions produced in each experiment was calculated from these pH measurements.

$$\left[H^{+}_{(aq)}\right] = 10^{-pH} \qquad \text{Equation 2.3}$$

$$No.H^{+} = 10^{-pH} \times N_A \times V \qquad \text{Equation 2.4}$$

In this experiment, N_A is Avogadro's number (6.022×10^{23}), and V is the catholyte volume, which is $15\ mL$. The number of H^{+} reduced was then calculated by taking the initial and final H^{+} difference, by assuming that the volume remained constant throughout the experiment:

$$No. H^{+}\ reduced = Initial\ H^{+}\ - Final\ H^{+}$$ Equation 2.5

The experimental change in the H^{+} concentration can be calculated using the following equation:

$$\left(\Delta\left[H^{+}_{(aq)}\right]\right) = -\frac{No. H^{+} reduced}{V \times N_A}$$ Equation 2.6

The experimental change in H^{+} concentration was compared with the expected H^{+} concentration change, derived from Faraday's law of electrolysis:

$$N = \frac{it}{e}$$ Equation 2.7

Where N is the number of electrons involved in the reaction, i is the current, t is the time for which the current is applied, and e is the charge of an electron $(1.602 \times 10^{-19}\ \ C)$. It was assumed that the number of electrons involved in the reaction is equivalent to the number of H^{+} ions reduced, assuming 100% conversion of the discharge current and considering only the hydrogen evolution reaction occurring in the catholyte:

$$2H^{+}_{(aq)} + 2e^{-} \rightarrow H_{2(g)}$$ Equation 2.8

2.3 Results and Discussion

A summary of averaged pH measurements in the cathode compartment of the plasma electrochemistry setup operated at a constant discharge current of 3 mA, at the experimental series 01 (using an electrolyte solution volume of 15 mL) and the needle was positioned approximately 1 mm and 3 mm away from the electrolyte's surface on the cathode side, is

According to Figure 2.2, in experimental series 02 (Raw data available in Table S2.3 and S2.6 of SI – APPENDIX A), when the volume of the electrolyte solution is increased compared to series 01, it has been observed that the pH of the solution did not change throughout the experiment compared to the initial pH (approximately 3.0). Therefore, increasing the volume of the electrolyte solution tends to reduce the intensity of the plasma-solution interaction, resulting in a relatively constant pH value indicate a more acidic environment than situations involving a low volume of electrolyte solution.

However, it is essential to consider uncertainties associated with the pH measurements. These uncertainties may stem from several factors such as environmental fluctuations, and variability in experimental conditions. The pH measurement device's precision and calibration procedures' accuracy are crucial factors influencing the reliability of the pH measurements obtained. Additionally, variations in experimental conditions, such as electrode positioning and electrolyte volume, may introduce uncertainty in the observed pH values.

In the three trials of 1 mm distance, the average standard deviation (refer to Tables S2.4 of SI – APPENDIX A), was found to be 0.076, and the relative error appears to decrease from 2 minutes to 30 minutes. The percentage error of 2.2% was observed at the lower end. In comparison, a 0.6% percentage error was noted at the maximum exposure time. All results appear to fall within a 2% variation range. In the three trials of 3 mm distance, the average standard deviation (refer to Tables S2.5 of SI – APPENDIX A), was found to be 0.064, and the relative error appears to decrease from 2 minutes to 30 minutes. The percentage error of 2.4% was observed at the lower end. In comparison, a 0.5% percentage error was noted at the maximum exposure time. All results appear to fall within a 2% variation range.

For the Hydrogen ion concentration in 1mm, the average standard deviation (refer to Tables S2.9 of SI – APPENDIX A), was found to be 1.17 x 10^{-4} M, and the relative error appears to decrease from 2 minutes to 30 minutes. The percentage error of 36% was observed at the lower end. In comparison, a 19% percentage error was noted at the maximum exposure time. In 3 mm distance, the average standard deviation (refer to Tables S2.10 of SI – APPENDIX A), was found to be 0.60 x 10^{-4} M, and the relative error appears to decrease from 2 minutes to 30 minutes. The percentage error of 4.8% was observed at the lower end. In comparison, a 4.7% percentage error was noted at the maximum exposure time.

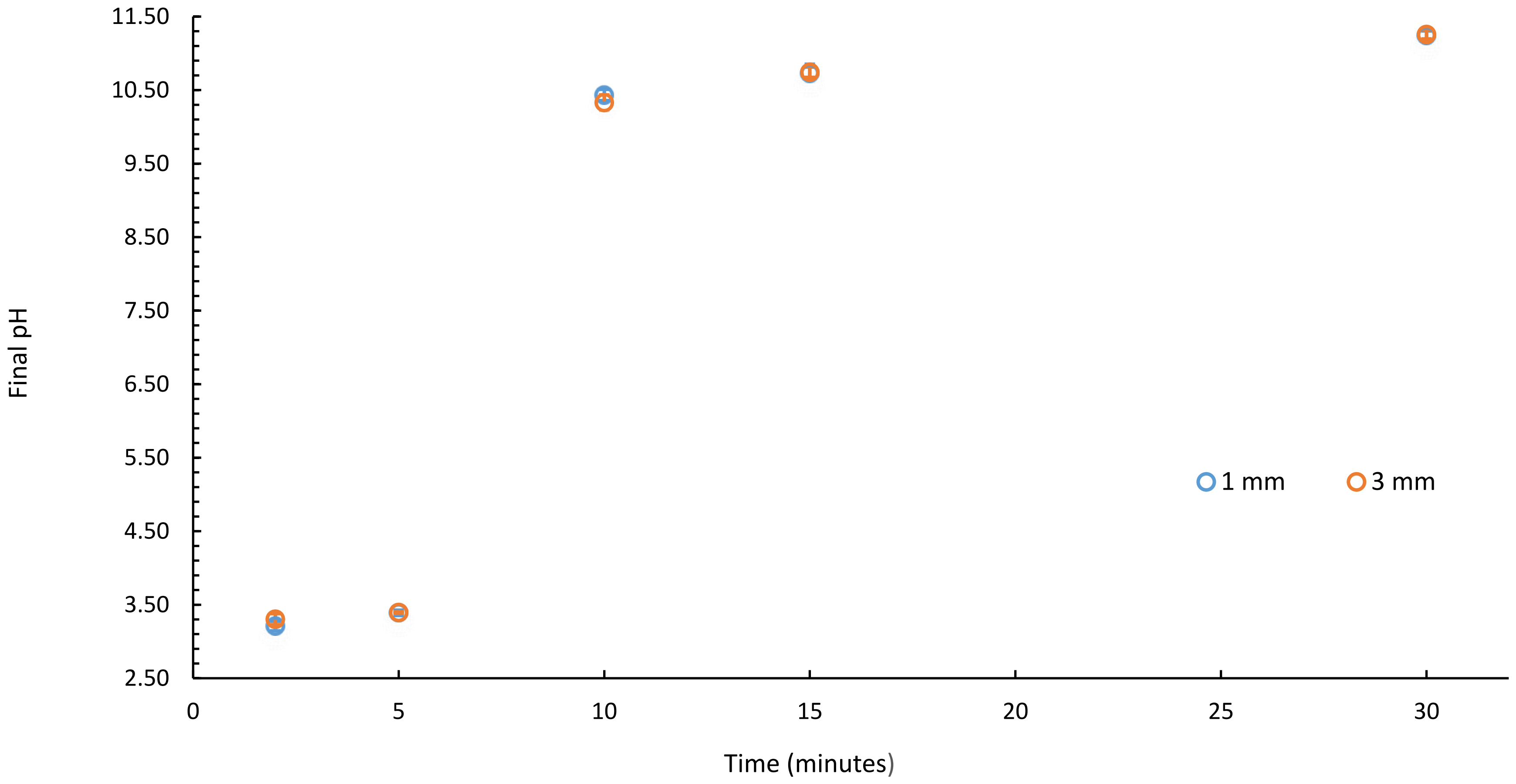

Figure 2.2: The average final pH as a function of time in the cathode compartment of the plasma electrochemistry setup maintained at a consistent discharge current of 3 mA, when the needle was positioned approximately 1 mm and 3 mm away from the electrolyte's surface on the cathode side. Error bars represent the standard error associated with the recorded measurements.

Using equation 2.4 initial and final H^+ ions were calculated to find the number of H^+ ions reduced during the process using equation 2.5. To calculate the experimental change in the H^+ ions concentration during the process, equation 2.6 was utilized and all the calculated data available in tabulated in Tables S2.7 and S2.8 of supplementary information in Appendix A.

The average change in the H^+ ions concentration over the selected time interval was calculated (Calculated data available in Table S2.9 and S2.10 of SI – APPENDIX A), and Figure 2.3 illustrates the average change in the concentration of H^+ ions as a function of time in the cathode compartment of the plasma electrochemistry setup maintained at a constant discharge current of 3 mA when the needle was positioned approximately 1 mm and 3 mm away from the electrolyte's surface on the cathode side and the experimental work done by Witzke et al., [1] at two different discharge current of 2 mA and 4 mA is also presented in this figure (Data available in Table S2.12 and S2.13 of SI – APPENDIX A).

In our study, from Figure 2.3, we can observe that the change in concentration of hydrogen ions gradually increases over time at a consistent pace, specifically for time intervals shorter than 15 minutes. Furthermore, we note that the rate at which the change in concentration of hydrogen ions decreases becomes more pronounced after 15 minutes.

According to Figure 2.3, when the distance between the needle tip and the solution interfaces is decreased, the plasma discharge is closer to the solution. This closer interaction results in a higher concentration of energetic electrons reaching the solution. These energetic electrons can react with H^+ ions present in the solution, leading to their reduction (Equation 2.1) and subsequent decrease in concentration. As a result, the pH of the solution may increase, indicating a decrease in acidity. Conversely, increasing the distance between the needle tip and the solution interfaces reduces the intensity of the plasma-solution interaction. This reduced interaction leads to a lower concentration of energetic electrons reaching the solution. Consequently, the reaction between electrons and H^+ ions are less pronounced, and the concentration of H^+ ions may remain relatively higher.

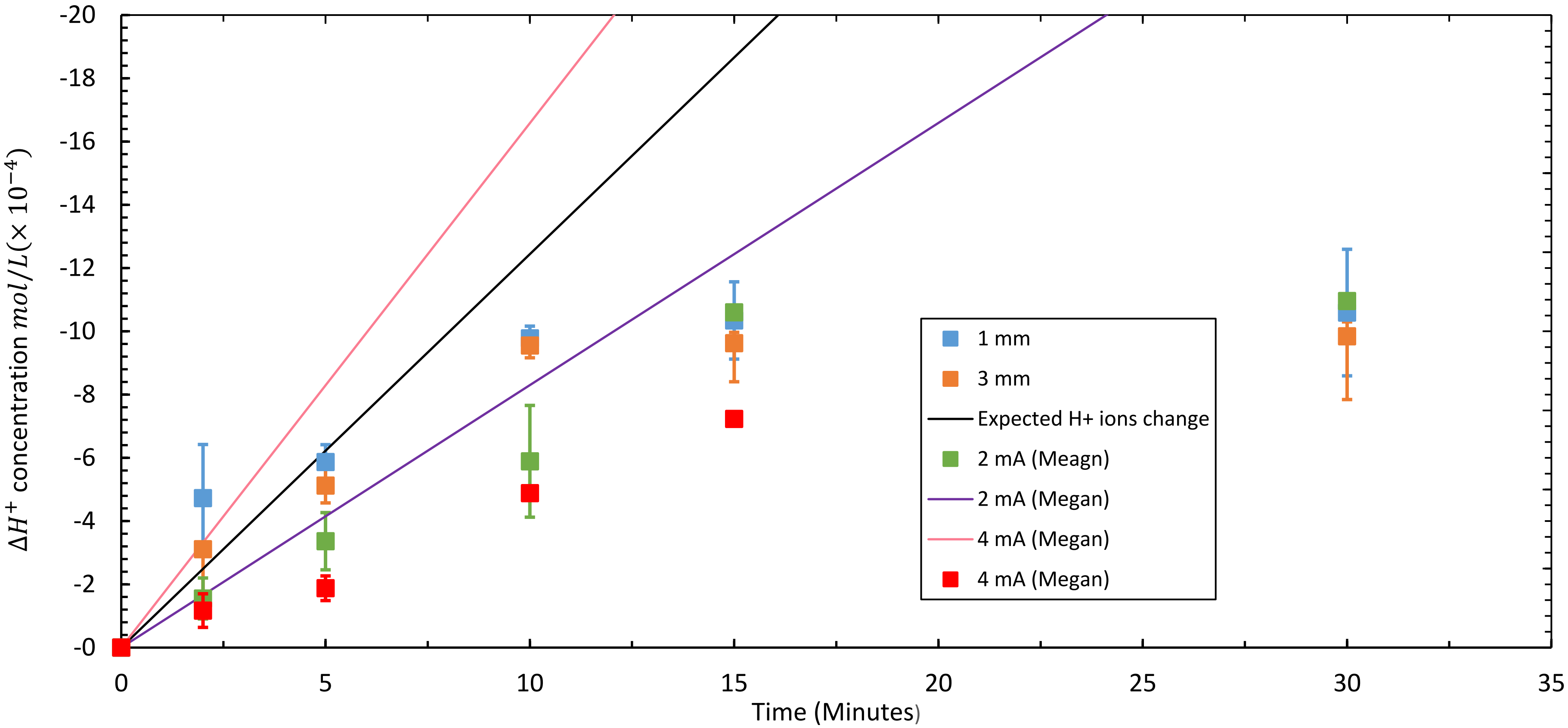

Figure 2.3: Comparison of the average change in the concentration of H^{+} ions as a function of time in the cathode compartment of the plasma electrochemistry setup maintained at a consistent discharge current of 3 mA, when the needle was positioned approximately 1 mm and 3 mm away from the electrolyte's surface on the cathode side with the experimental work done by Witzke et al., [1] at two different discharge current of 2 mA and 4 mA. Error bars represent the standard error associated with the three recorded measurements, and the solid lines represent the change in the concentration of H^{+} ions as predicted by Faraday's law.

Upon thorough examination of the experimental data, I have collected and the previously conducted experiment data by Witzke et al., [1], and according to Figure 2.3 it became evident that the distribution of my data remarkably aligns with Witzke's data. This synchronization in the distribution pattern substantiates the reliability and validity of my experimental findings. Furthermore, the distribution of my data exhibits a remarkable congruence with that identified in Witzke's data. This concordance strengthens the consistency and generalizability of the outcomes derived from my research.

We conducted a comparison between these findings and the expected outcomes derived from the assumptions of water electrolysis and Faraday's law (Equation 2.7 and 2.8), considering the discharge current. Figure 2.3 (Data available in Table 2.11 of SI – APPENDIX A) illustrates that the observed alteration in H^+ concentration aligns well with Faraday's law during shorter run times. However, discrepancies emerge at longer run times, where the measured change is less than the corresponding predicted value. Witzke [1] (Expected data of Witzke’s work available in Table 2.14 of SI – APPENDIX A) well explained that these discrepancies is due to the processes of diffusion and/or electromigration of H^+ occurring between the cell compartments, resulting in a net pH change smaller than expected. Further details can be found in her work, providing comprehensive insights into these phenomena.

According to the Figure 2.2, in experimental series 02, (Raw data available in Table S2.3 of SI – APPENDIX A), when the volume of the electrolyte solution is increased from 15 mL to 180 mL, it has been observed that the relative intensity of the plasma-solution interaction decreases. This reduction in interaction diminishes the concentration of energetic electrons reaching the solution. Consequently, the reaction between these electrons and H^+ ions become less pronounced. As a result, the concentration of H^+ ions may remain relatively constant throughout the experiment. Therefore, increasing the volume of the electrolyte solution tends to reduce the intensity of the plasma-solution interaction, resulting in a relatively constant concentration of H^+ ions and a consequent lower pH value indicate a more acidic environment than situations involving a low volume of electrolyte solution.

The setup was further demonstrated to be operational by qualitatively visualizing the pH variations caused by an aqueous electrode-generated microplasma, involving the utilization of a pH-sensitive dye named universal indicator (A colour chart based on the pH value of the universal indicator is illustrated in Figure S2.1 of SI – APPENDIX A). This approach enables the observation of pH changes in both space and time during microplasma operation.

Figure 2.4 illustrates the visual representation of the microplasma generated by an electrolyte solution containing pH-sensitive dye. The reduction reaction occurs at the interface between the microplasma and the liquid, leading to a pH increase. This is evident from the noticeable alteration in the dye's colour, which shifts to blue. Conversely, the oxidation reaction occurs at the anode, resulting in the generation of O_2 gas bubbles and a concurrent decrease in pH, according to equation 2.2 and as indicated by the change in colour to pink (Figure S2.2 of SI – APPENDIX A illustrates a visual depiction of the solution containing the pH-sensitive dye before and after the treatment at various intervals). According to equation 2.1, reducing hydrogen ions leads to a pH increase. The change in colour to blue after 10 minutes signifies a significant shift towards a more alkaline pH. The maintenance of the blue colour after 15 and 30 minutes indicates a relatively stable alkaline pH. This blue colour suggests that the substance reached a pH level in the alkaline range, typically around pH 10 or higher.

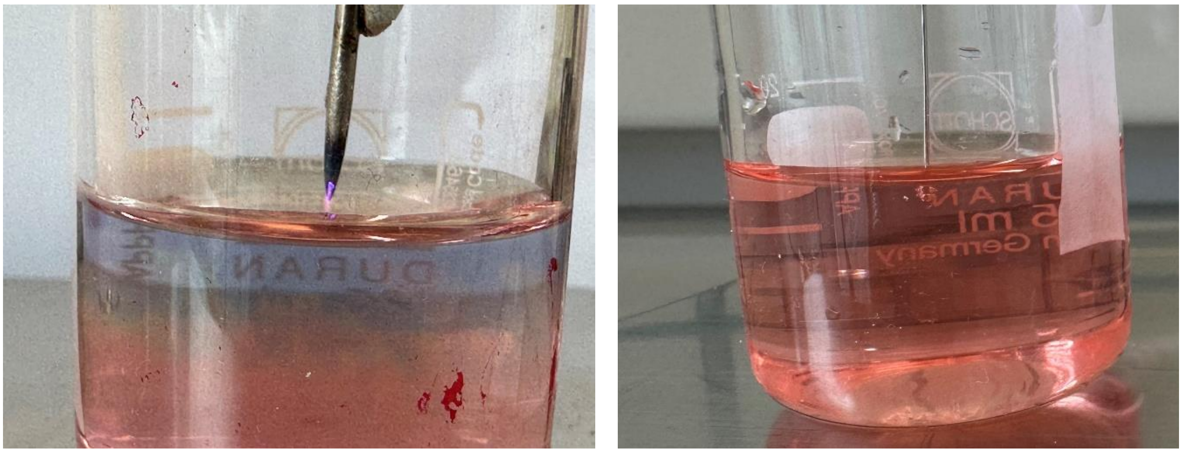

(a) (b)

Figure 2.4: A visual representation shows a microplasma generated by an electrolyte solution containing pH-sensitive dye. The reduction reaction occurs at the interface between the microplasma and the liquid, leading to a pH increase. This is evident from the noticeable alteration in the dye's colour, which shifts to blue. Conversely, at the anode, the oxidation reaction takes place, resulting in the generation of O_2 gas bubbles and a concurrent decrease in pH, as indicated by the change in colour to pink.

2.4 Conclusion

In conclusion, this study investigated the charge-transfer reactions at the plasma-liquid interface using an atmospheric-pressure microplasma as a metal-free gaseous electrode. The study provided experimental evidence that an atmospheric-pressure microplasma can serve as a gaseous electrode, initiating and controlling electron-transfer reactions in aqueous solutions. This study further confirms previous research studies highlighted earlier in this chapter and the new possibilities for electrochemistry by leveraging the interplay between electrons in the gas phase and ionic solutions, offering potential advantages in terms of cost and availability compared to traditional metal electrodes, which will be discussed in the next chapter where plasma – liquid interactions involving in microplastic degradation.

Obtained pH measurements demonstrated that plasma electrons participate in electrolytic reactions, reducing protons (H^+) to hydrogen gas which provides the fundamental involvement of plasma electrons in interactions between plasma and liquid, with significant implications for diverse applications, including microplastic degradation, plasma medicine and the synthesis of plasma-liquid materials.

The results demonstrated that the change in concentration of hydrogen ions gradually increased over time, with a more pronounced decrease after 15 minutes. The distance between the plasma discharge needle tip and the solution interfaces played a role in the intensity of the plasma-solution interaction and the concentration of energetic electrons reaching the solution. Decreasing the distance resulted in a higher concentration of energetic electrons and a subsequent decrease in acidity while increasing the distance reduced the intensity of the interaction and maintained a relatively higher concentration of hydrogen ions.

Comparisons with previous research conducted by Witzke et al., [1] provided further validation and support for the findings of this study. The distribution and trend of the experimental data aligned with the previous study, strengthening the reliability and generalizability of the outcomes. However, there are still uncertainties surrounding the exact characteristics and mechanisms of the interactions occurring at the interface between the plasma and the liquid.

The results from this chapter are important for guiding the setup of the experimental apparatus in the next chapter. The upcoming modifications will include reducing the distance between the needle tip, and the solution interfaces to 1 mm and decreasing the volume of the electrolyte solution. These adjustments enhance the interaction between the plasma discharge and the solution, leading to a greater concentration of energetic electrons.

3

Microplastic degradation using plasma-liquid interactions – A Case Study for Polystyrene

Microplastic (MP) pollution has been attracting significant attention because of its widespread presence in various environmental systems, its potential harm to ecosystems and aquatic life, and its ability to accumulate in the food chain. Removal of these plastics is therefore very important to mitigate these ecological and health risks. In this study, a novel liquid plasma process was employed to evaluate its effectiveness on microplastic degradation. To that end, solution concentration, exposure time, and electrolyte type were investigated as a function of microplastic degradation using analytical techniques such as Gel Permeation Chromatography (GPC), Fourier-Transform Infrared Spectroscopy (FTIR) and spectroscopy. It was found that the liquid plasma treatment significantly reduced the microplastic particles in the tested solutions, indicating its potential as an effective method for microplastic removal. In conclusion, the results of this study suggest that the novel liquid plasma process shows promising method for mitigating microplastic pollution, offering a potential solution to combat this environmental issue and safeguard our ecosystems and

health. Further research is needed to optimize the process and assess its scalability and environmental impact in real-world applications.

3.1 Introduction

Every year, a substantial quantity of plastic is discharged by human society into aquatic environments. Therefore, plastic pollution is widespread and has garnered significant global recognition [140]. Approximately 10% of the plastic produced is estimated to end up as fragmented particles in the marine environment [146]. Plastics can undergo decomposition and size reduction through natural processes such as physical, chemical, and biological environmental mechanisms. This leads to the formation of plastic particles, specifically those with a diameter smaller than 5 mm, commonly called microplastics (MPs) [147–149]. MPs exhibit distinctive features: a large specific surface area and strong adsorption capacity [150]. These qualities empower MPs to absorb and accumulate persistent pollutants, including heavy metals and polycyclic aromatic hydrocarbons (PAHs) [151]. Furthermore, MPs are prone to ingestion by organisms and can be transferred to higher trophic levels through the food chain, resulting in diverse toxicological consequences for animals and humans [152–160].

Polypropylene (PP), polystyrene (PS) and polyethylene (PE) make up approximately 42% of all plastic products ever produced, and it is not surprising that these materials are the most widespread form of plastic pollution worldwide [161,162]. Polystyrene is a highly utilised plastic in various industries worldwide, making it one of the most employed commercial plastics [163,164]. Consequently, it is also one of the most frequently encountered polymers in marine environments [165,166] and a plastic material extensively studied and suggested to have toxic properties [167–169].

Removing MPs in wastewater primarily involves biological [170,171], physical, and chemical methods [150,172]. When microorganisms ingest MPs, they can cause harm to their digestive systems, leading to suffocation or death [150] in biological methods. Therefore, the effectiveness of biological methods in treating MPs is limited. Chemical methods rely on redox reactions [173] to eliminate MPs; however, a substantial amount of reactive chemicals is required for removal due to their chemical stability. Storing and transporting these chemicals can be costly and carries the risk of leakage. Physical methods, such as air flotation [174], flocculation, and membrane filtration, offer rapid and efficient removal of MPs [175]. However, these methods remove MPs through phase transfer, without ongoing elimination, which poses a risk of secondary pollution from MPs. Finding effective solutions for managing the collected MPs from air flotation, flocculation, membrane filtration, and others remains a significant challenge.

Electrical discharge plasma is being increasingly utilised to eliminate organic pollutants from gas, water, and soil [176–179]. By employing high voltage discharge, electrical discharge plasma generates reactive species such as energetic electrons, radicals, and oxidising molecules with high efficiency and environmental friendliness [180–183]. Notably, these reactive species are produced in situ, eliminating the need for storing and transporting chemical reagents. The reactive species generated by electrical discharge plasma can quickly break down the chemical bonds of organic pollutants, leading to their degradation into smaller molecules and eventually forming CO_2 and H_2O [184,185]. Hence, in theory, electrical discharge plasma has the potential to remove MPs since MPs primarily consist of C and H atoms, and it has been demonstrated that electrical discharge effectively disrupts C-H bonds [179,185]. The advantages of utilising electrical discharge plasma for MPs removal are that it decomposes MPs at the molecular level, thereby overcoming the issue of secondary leakage that commonly occurs in phase transfer methods, and the decomposition of MPs through electrical discharge plasma eliminates the need for complex post-processing steps like separation and landfilling [186]. The efficiency and the ways electrical discharge plasma removes microplastics are interesting subjects that still need more exploration and understanding.

Zhou and his team [187] investigated the effects of electrical discharge plasma on the aging behaviours of polyvinyl chloride microplastic (PVC-MP) in complex simulated environments. Their study aimed to understand how the presence of electrical discharge plasma accelerates the aging processes of MPs. The combined findings from their various analytical techniques, including Scanning Electron Microscopy (SEM), Energy-Dispersive X-ray spectroscopy (EDX), X- ray diffraction (XRD), Fourier-Transform Infrared Spectroscopy (FTIR), X-ray Photoelectron Spectroscopy (XPS), and thermogravimetric analyses, have confirmed that the reactive oxygen species (ROS) generated in the plasma system, along with intense UV irradiation, collaboratively contribute to the dissociation of cellulose acetate and C-H bonds present in the PVC-MP structure. Consequently, they discovered that the PVC-MP undergoes aging and exhibits distinct characteristics, such as a reduced particle size, an increased specific surface area, enhanced hydrophilicity, and heightened crystallinity. Their study introduces a novel perspective on accelerating the aging process of MPs through plasma oxidation, enabling a better understanding of the environmental behaviours and risks associated with MPs in natural and complex conditions.

Miao and team [188] successfully utilised electrolytic fluorination (EF)-like technology based on a TiO_2/C cathode to degrade PVC microplastics. The process involved potentiostatic electrolysis at -0.7 V vs. Ag/AgCl at a temperature of 100 ℃ for 6 hours. Their results showed that their approach achieved a 56 wt % removal of PVC microplastics and a 75 % dichlorination efficiency. The temperature was found to play a vital role in the dichlorination process, with higher temperatures favouring the degradation of PVC. They summarised that the dichlorination of PVC microplastics mainly occurred through direct reduction facilitated by the applied cathode potential. Additionally, the oxidisation of hydroxyl radicals led to the oxidation and breakage of the PVC backbone.

Furthermore, they successfully investigated that shedding organic compounds during the degradation process indirectly promoted further PVC microplastic dichlorination. Their findings also show that some macromolecular organics were shed during the PVC degradation process and decomposed into smaller macromolecules. Their technology not only provides a feasible and eco-friendly strategy for the degradation of PVC microplastics but also has the potential to be applied to other chlorinated species or plastics such as 2,4-dichlorophenol, polyethylene, polypropylene, and polystyrene [188].

A study by Ren et al., [189] proposed a dielectric barrier discharge (DBD) plasma to eliminate PVC. Moreover, their results eliminated that DBD plasma demonstrated excellent performance in removing PVC, with a removal efficiency of 85.9 % achieved under optimal conditions where increasing the discharge voltage benefits PVC removal. Further, they investigated that a moderate amount of water benefited PVC removal. This is because water facilitated the formation of hydrated electrons $\left(eq_{aq}^{-}\right)$ and helped immobilise PVC within the discharge zone. However, according to their findings, excess water hindered the reaction between PVC and reactive species, decreasing PVC removal efficiency. Among the reactive species generated by DBD plasma eq_{aq}^{-} was found to be the most effective substance for PVC removal.

This study aimed to explore the degradation of PS MPs using plasma-liquid interactions. An experimental approach using a plasma–liquid system was employed to determine the optimal parameters for plasma degradation to effectively break down MPs in water. Various operating parameters were systematically investigated, including electrolyte type and time. In order to assess the extent of degradation of microplastics (MPs) degradation after undergoing plasma treatment, a microscopy technique was used to visually examine their characteristics, such as size, shape, and colour. However, this visual analysis is qualitative and often inconclusive or misleading [190]. Alternatively, quantitative methods called Fourier transform infrared spectroscopy (FT-IR) [191] and gel permeation chromatography (GPC) [192] were used. The following sections will discuss a detailed description of the experimental setup used in this study. The findings of this study will provide valuable insights and recommendations regarding the degradation of PS MPs from plasma-liquid interactions.

3.2 Experimental Section

3.2.1 Materials

Materials and solvents were obtained from the following suppliers: Polystyrene (Sigma Aldrich, average molecular weight = 220K gmol^{-1}), tetrahydrofuran (THF) (Unichrom, HPLC grade), Sodium Chloride (NaCl, Sigma Aldrich), Sodium Sulphate ($NaSO_4$, Sigma Aldrich). All the solutions were prepared using ultra-pure water (Resistivity – 18.2 megaohm). A Pt counter electrode made with Pt wire (length: 70 mm, electrode diameter 0.5 mm) was used as a counter electrode. A stainless-steel needle which was prepared at the JCU mechanical workshop used to ignite the plasma. The salt bridge was made, and samples were filtered through a Whatman 1, 18.5 cm filter paper. After every experiment, the needle was cleaned by polishing the outside surface with sanding sheets of 800 grits (IRWIN). The power was obtained by an extra high voltage power supply (Industrial Equipment & Control PTY. Ltd., 6000V. DC. 3mA. Max.).

3.2.2 Experimental Setup

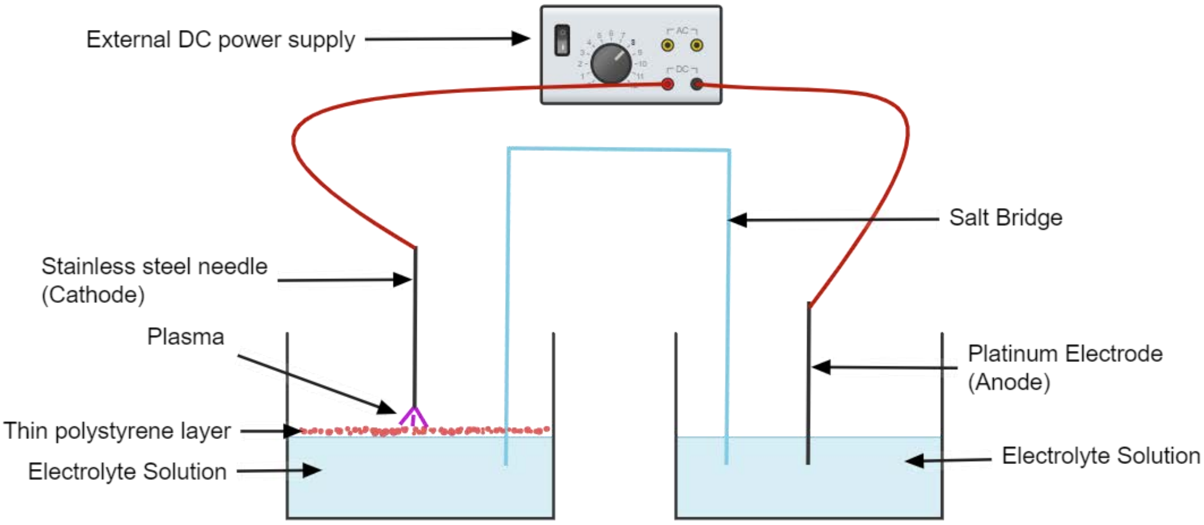

Figure 3.1: The diagram of plasma - electrochemical setup

Plasma-electrochemical reactions were carried out in opened glass cell configurations schematically depicted in Figure 3.1. The setup included a split glass cell with a salt bridge that prevented mixing the electrolytes on the cathodic and anodic sides, which was pretested in the previous chapter. All the experiments were performed at room temperature using a constant discharge current (3 mA).

Using a laboratory stand, a stainless-steel needle was positioned approximately 1 mm away from the electrolyte's surface on the cathode side. The anode was constituted by immersing a Pt wire into the solution. A DC power supply was connected to the experimental setup, as illustrated in Figure 3.1. All the experiments were conducted at room temperature.

3.2.3 Preparation of microparticles

PS from white transparent PS beads with an average diameter of 5 mm was processed into even small MPs using a Magic Bullet-Nutribullet 900 series blender and sieved over a stainless-steel screen sieve (Glenamer Sieves) to collect the MPs within the size range of 200 to 300 µm. Before and after each utilization, blenders underwent a cleansing process using white cotton tissues and tap water, intending to prevent any potential spread of contaminants. Stainless steel sieves were also washed and oven dry before and after each usage to prevent any potential spread of contaminants [193].

MPs were irregularly shaped with smooth surface area, and Figure 3.3 (a) shows the surface of the MPs. The shape and colour characteristics of PS MPs were recorded through microscopy. Before usage, MPs underwent an analysis using Attenuated Total Reflection Fourier Transform Infrared Spectroscopy (ATR-FTIR) with a PerkinElmer Spectrum 100 FTIR spectrometer to ensure accuracy.

3.2.4 Processing parameters and treatment conditions

The processing parameters, including the duration of the processing, reagent concentration, and laboratory temperature were determined based on practical considerations. An amount of 15 mL of reagent used to process 1 gram of microplastics.

0.15 g of polystyrene MPs (200 – 300 micrometre) was evenly distributed on the electrolyte solution. Then, the MPs were exposed to 06 different treatment conditions using NaCl and $NaSO_4$ (Table 3.1). Each experiment was performed at room temperature using a constant discharge current (3 mA). All experiments were repeated three times to ensure the reliability of the results. Following plasma treatments, degraded MPs were air-dried overnight under ambient conditions.

Table 3.1: Treatment conditions used in this study (Different electrolytes and time intervals)

Electrolyte Solution	Treatment Time (min)
NaCl (0.6 M)	10, 30, 60
Na_2SO_4 (0.3 M)	10, 30, 60

3.2.6 Analysis

3.2.6.1 FTIR Analysis

FTIR (Fourier Transform Infrared) analysis is a widely used technique for identifying and characterising chemical compounds based on their infrared absorption spectra. FTIR analysis serves as a pivotal tool in this experiment, providing valuable insights into the chemical composition and structural changes of the samples before and after plasma treatment. FTIR analysis is widely employed for identifying and characterizing chemical compounds based on their infrared absorption spectra, which offer information about the functional groups and chemical bonds present in the samples. It provides information about a sample's functional groups and chemical bonds. The principle behind FTIR analysis involves the interaction of infrared radiation with a sample. When infrared light passes through a sample, specific wavelengths of the radiation are absorbed by the sample's molecules. The absorbed wavelengths correspond to specific vibrational modes of the chemical bonds in the molecules [194].

Infrared spectra of the samples were collected using a Thermo Scientific Nicholet^{TM} is^{TM} 5 FTIR spectrometer equipped with an attenuated total reflectance crystal head attachment. The obtained spectrums were compared with the reference spectrum recorded with MPs before plasma treatment. The scanning range was 500 to 4000 cm^{-1}, and the collection time was 16 s [194,195].

3.2.6.2 Microscopy Analysis

For the evaluation of microplastics (MPs) before and after plasma treatments, a ZEISS Discovery V8 microscope fitted with a ZEISS Axiocam 208 colour / 202 mono camera was employed. The microscope was properly calibrated, and the scale was checked to ensure the accuracy of the measurements. Images captured during the analysis included a scale for size reference.

3.2.6.3 Gel Permeation Chromatography (GPC) Analysis

Gel permeation chromatography (GPC), or size exclusion chromatography (SEC), separates and analyses macromolecules, such as polymers and biopolymers, based on their size or molecular weight. The weight-average molecular weight (Mw), which represents the average molecular weight in grams per mole, and the polydispersity index (PDI), which indicates the heterogeneity in polymer chain lengths, were utilized to gain insights into the distribution of molecular weights in the sample. PDI stands for Polydispersity Index. It is a term commonly used in polymer science and refers to a measure of the molecular weight distribution of a polymer sample. In a polymer sample, the molecular weight can vary, and the PDI provides information about the breadth of this distribution. A PDI value of 1 indicates a monodisperse polymer sample where all the polymer chains have the same molecular weight. On the other hand, a higher PDI value indicates a broader distribution, with a range of molecular weights present in the sample [196].

Microplastics (2 mg) were dissolved in 1.5 mL of tetrahydrofuran (THF) and mixed until no solid particles remained. A small volume of the resulting solution (50 µL) was injected into a 1260 Infinity II Multi-Detector GPC system (Agilent Technologies), which consisted of an ultraviolet (UV) absorbance detector and a refractive index detector. The GPC system was equipped with two PLgel 5 µL MIXED-C columns (300×7.5 mm) from Agilent Technologies. Before the analysis, the GPC columns were calibrated using narrow standards of PS in THF at a temperature of 35 °C. This calibration allowed for the accurate determination of the molecular weight distribution of the sample based on its elution time.

3.3 Results and Discussion

Additive-free and virgin Polystyrene (PS) was specifically chosen for several reasons. Its commercial availability ensured easy reproducibility and facilitated chemical manipulation during the study. Furthermore, previous studies have demonstrated that the extent of polymer degradation is not influenced by the molecular weight of PS, as evidenced by relevant reports [193,197–199]. Hence, PS with an average molecular weight was chosen to represent both high and low molecular weight PS, ensuring that the selected material adequately represented the range of PS commonly encountered in environmental contexts.

Microscopic analysis of grounded 5 mm microplastics (MPs) beeds showed that the particles exhibited an irregular size ranging from 200 to 300 micrometres (Figure 3.4a). The Fourier-transform infrared spectroscopy (FT-IR) spectra of the untreated control microplastics exhibited characteristics consistent with pure polystyrene (PS) (Figure 3.5) [200].

3.3.1 GPC Analysis

The GPC analysis (Figure 3.2; Figures S3.1 and S3.2 I APPENDIX B) revealed notable changes in the microplastics' molecular weight and PDI values following plasma-liquid interactions. In the untreated PS samples, the average molecular weight was 172,438, with a PDI of 2.53. Comparatively, the microplastics treated for 30 minutes in NaCl exhibited a slightly reduced average molecular weight of 151,214 and a decreased PDI of 2.285. Similarly, the 60-minute treatment in NaCl resulted in an average molecular weight of 150,184 and a PDI of 2.293.

Interestingly, using Na_2SO_4 as the electrolyte solution further decreased the average molecular weight, with values of 138,241.67 and 126,984 observed after 30 and 60 minutes of treatment, respectively. The corresponding PDI values for Na_2SO_4 treatments were 2.363 and 2.49. These findings (Figure 3.2; Figures S3.1 and S3.2 I APPENDIX B) suggest that plasma-liquid interactions, especially in the presence of Na_2SO_4 facilitate microplastic degradation, resulting in a decrease in molecular weight and a slight narrowing of the molecular weight distribution.

Figure 3.3 illustrates the average molecular weight (Mw) of the PS MPs sample after undergoing treatment under different degradation conditions (Raw data presented in Table S3.1 of SI - APPENDIX B). The line graph represents the average distribution of polydispersity index (PDI) values corresponding to the PS MPs sample.

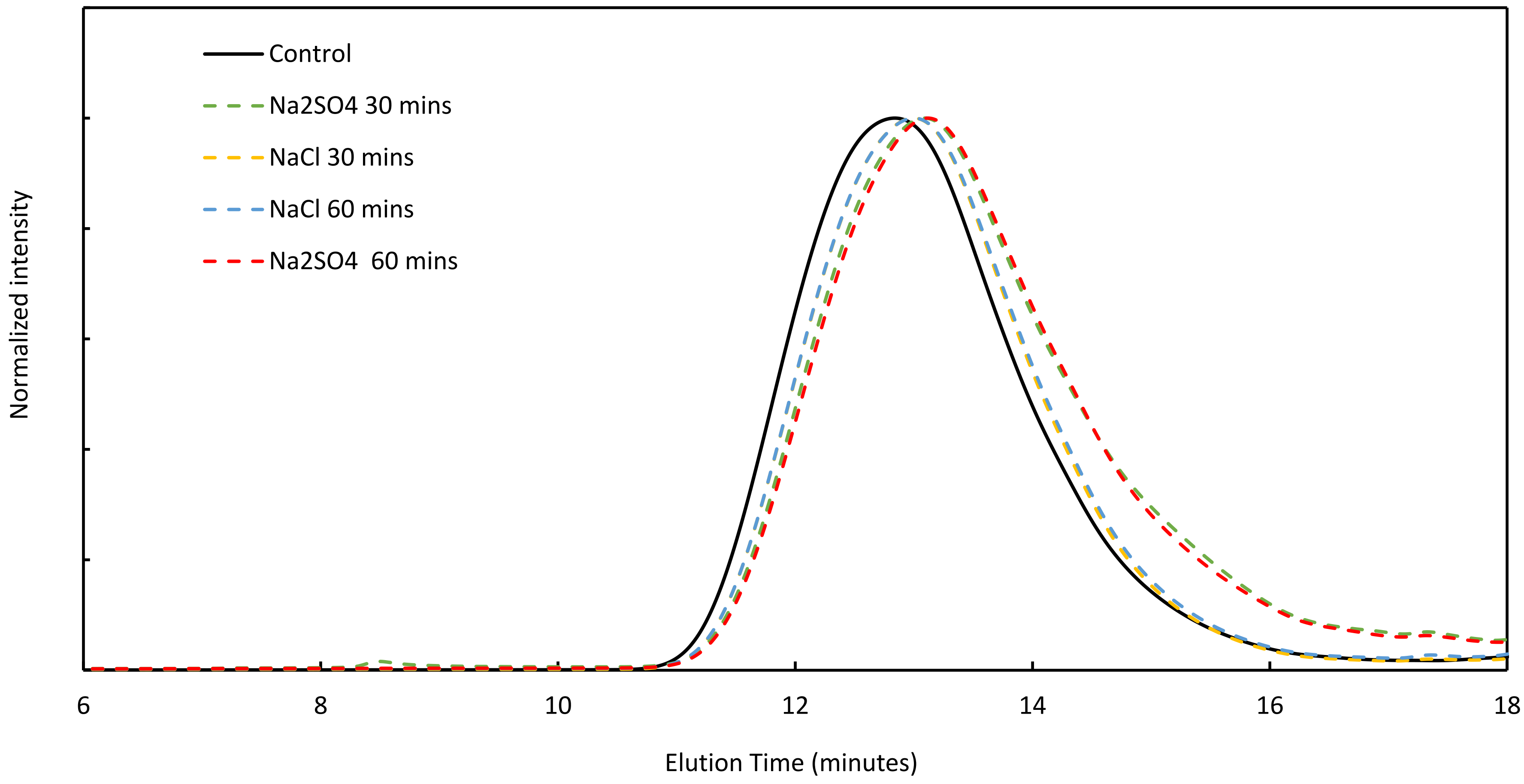

Figure 3.2: Gel permeation chromatography traces for pure polystyrene (PS) (control), and PS treated under the following digestion conditions: 30 minutes and 60 minutes with 0.3M Sodium Sulphate (Na_2SO_4) and 0.6 M Sodium chloride (NaCl).

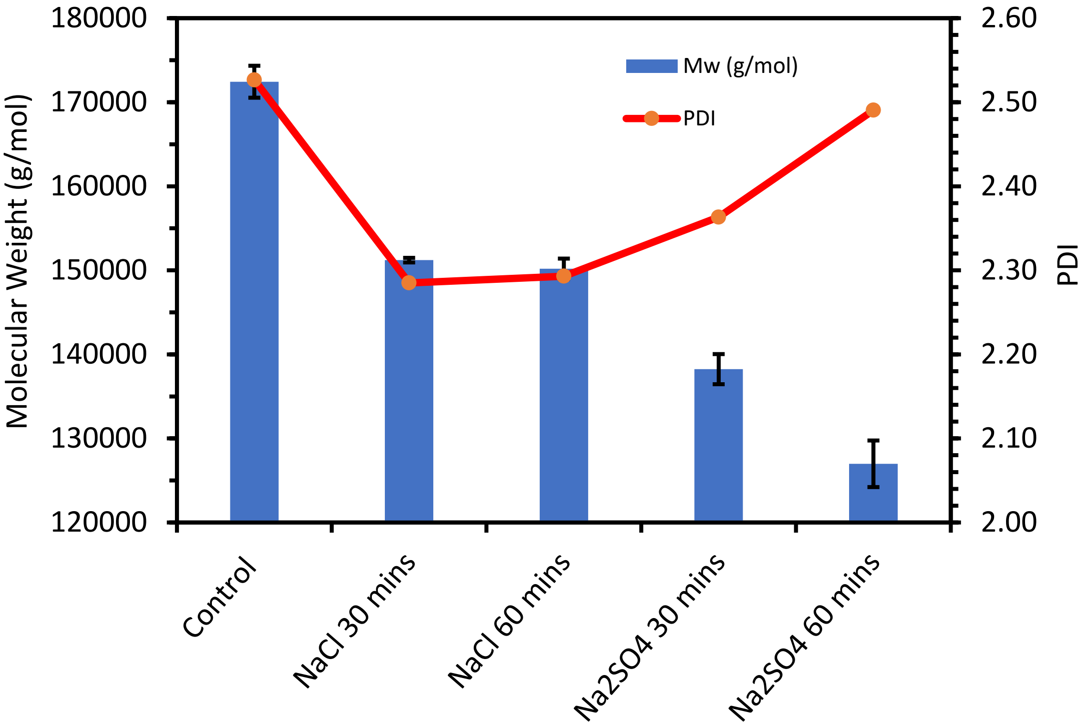

Figure 3.3: Comparison of Average Molecular Weight (Mw) and Polydispersity Index (PDI) of polystyrene microplastics (PS MPs) under varied degradation conditions.

The PDI curve in Figure 3.3 (Raw data presented in Table S3.2 of SI - APPENDIX B) showed that the control samples have a relatively broad molecular weight distribution. When the microplastics are treated with NaCl for 30 minutes (PDI 2.285), and 60 minutes (PDI 2.293), the PDI values decrease compared to the control samples. This suggests a narrowing of the molecular weight distribution. The PDI values remain relatively similar for both treatment times. When the microplastics are treated with Na_2SO_4 as the electrolyte solution, the PDI values increase compared to the NaCl treatments. The PDI values are 2.363 for the 30-minute treatment and 2.49 for the 60-minute treatment. This indicates a slight widening of the molecular weight distribution compared to the NaCl treatments.

In the three trials of finding molecular weight distribution, the average standard deviation (refer to Tables S3.1 of SI – APPENDIX B), was found to be 1714.9 g/mol, and the relative error appears to decrease from control test to 60 minutes treatment with Na_2SO_4. The percentage error of 1.1% was observed for the control sample. In comparison, a 2.6% percentage error was noted for the 60 minutes treatment with Na_2SO_4. In the three trials of finding PDI distribution, the average standard deviation (refer to Tables S3.2 of SI – APPENDIX B), was found to be 0.0774, and the relative error appears to decrease from control test to 60 minutes treatment with Na_2SO_4. The percentage error of 3.2% was observed for the control sample. In comparison, a 6.2% percentage error was noted at for the 60 minutes treatment with Na_2SO_4.

The observed changes in molecular weight and PDI indicate that plasma-liquid interactions can induce the breakdown of microplastic polymers, potentially leading to the generation of smaller fragments. The higher degradation efficiency observed in the Na_2SO_4 treatment may be attributed to the unique chemical properties of the solution, promoting the generation of reactive species that enhance the degradation process. Utilizing Na_2SO_4 as a supporting electrolyte leads to its dissociation into hydrogen sulphate ions (HSO_4^-). Consequently, persulfate ions ($S_2O_8^{2-}$) are formed through a chemical reaction (Equation 3.1). It is well-established in previous studies [201–203] that these persulfate ions possess high reactivity. This reactivity enables them to degrade microplastics (MPs) indirectly by oxidation.

$$2HSO_4^-(aq) \rightarrow S_2O_8^{2-}(aq) + 2H^+(aq) + 2e^- \qquad \text{Equation 3.1}$$

3.3.2 Microscopy Analysis

No noticeable differences were observed in the appearance of microplastics (MPs) treated with NaCl for 10 minutes and Na_2SO_4 for 10 minutes. Upon treatment for 30 minutes in NaCl, noticeable surface irregularities and signs of etching were observed, suggesting the initiation of degradation (Figure 3.4 (b)). This was consistent with the decrease in molecular weight observed in the corresponding GPC analysis described in the next part. Moreover, the microplastics treated for 60 minutes in NaCl showed more pronounced morphological alterations, including surface roughness and fragmented regions (Figure 3.4 (c)). These observations aligned with the further decrease in molecular weight detected by GPC. The microscopic examination provided visual evidence of the degradation process, indicating the progressive breakdown of the microplastic structure.

Similarly, the microplastics treated with Na_2SO_4 for 30 and 60 minutes exhibited significant morphological changes (Figure 3.4 (d) and (e), respectively). The light microscopy images revealed surface erosion, formation of pits, and fragmentation, consistent with the degradation observed in the GPC analysis. The distinctive alterations in microplastic morphology observed under different treatment conditions reinforced the notion that treatment time and solution composition play crucial roles in microplastic degradation.

3.3.3 FTIR Analysis

The FTIR spectra before and after plasma treatment for extreme treatment conditions are compared in Figure 3.5. According to that, unlike a previous study on photo-oxidation, no detection of a peak at 1712 cm^{-1}, corresponding to C=O bonds, was observed [201,204].

This suggests the possibility of direct oxidation of microplastics on the anode; however, a comprehensive conclusion awaits the results of water analyses, including assessments of dissolved organic and inorganic C. This outcome might indicate that the primary mechanism responsible for the degradation of microplastics is the direct oxidation occurring on the anode's surface. Further scientific research is needed to confirm this mechanism in a more rigorous and scientific manner.

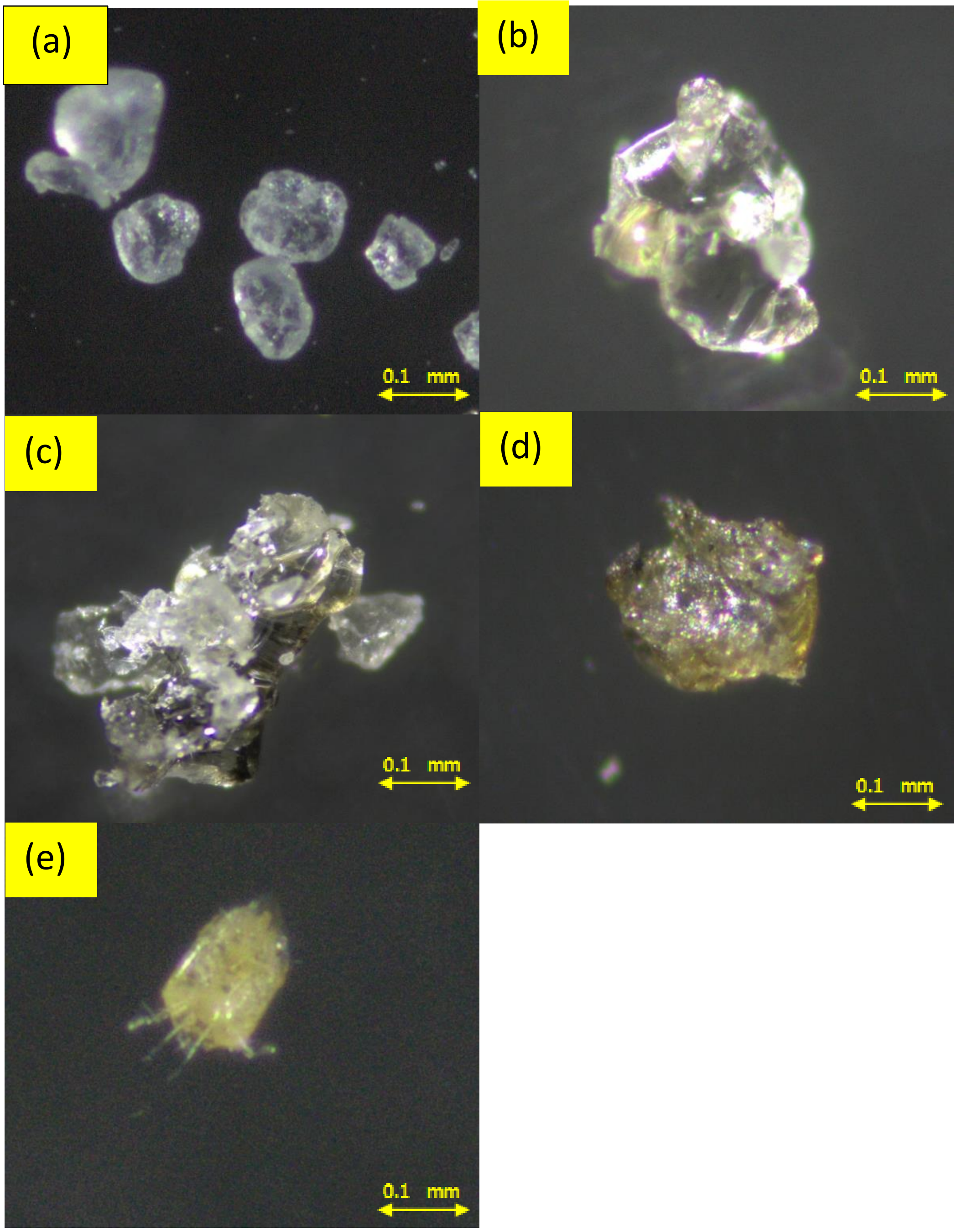

Figure 3.4: Microscope images of the treated and untreated polystyrene (PS) microplastics (a) untreated polystyrene 80x (b) PS treated for 30 minutes with 0.6 M NaCl 80x (c) PS treated for 60 minutes with 0.6 M NaCl 80x (d) PS treated for 30 minutes with 0.3 M Na_2SO_4 80x and (e) PS treated for 60 minutes with 0.3 M Na_2SO_4 80x.

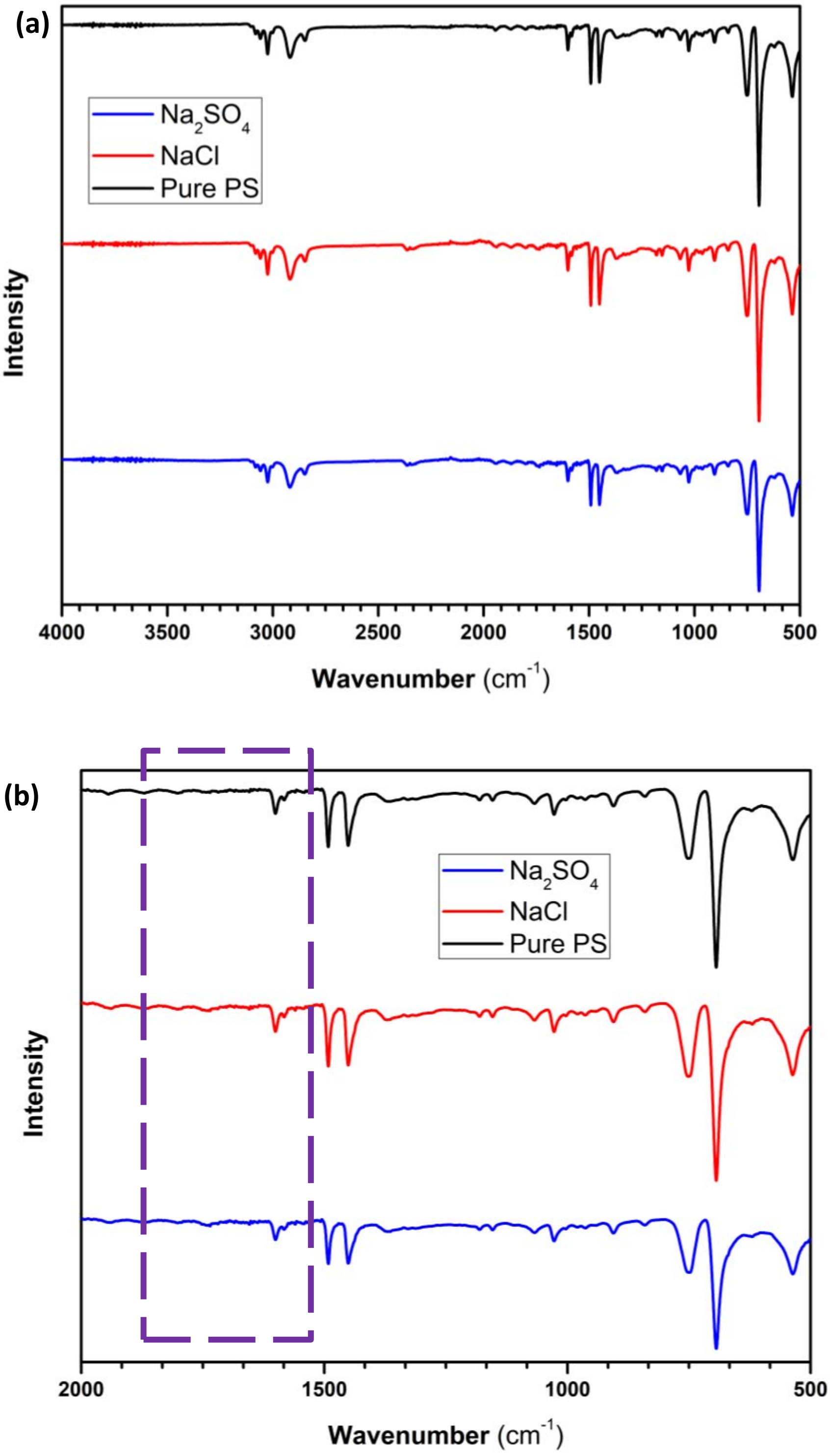

Figure 3.5: FTIR Spectrum of untreated polystyrene (Pure PS), and PS under the following treatment conditions: 60 mins with 0.6 M NaCl solution and 60 mins with 0.3 M Na_2SO_4 solution. (a) full spectrum from 4000 cm^{-1} to 500 cm^{-1}. (b) selected spectral range from 2000 cm^{-1} to 500 cm^{-1}. The purple box indicates the region where previous studies observed photo-oxidation, characterised by a peak at 1712 cm^{-1} corresponding to C=O bonds.

3.4 Conclusion

The plasma-based process emerges as a promising technology for degrading PS MPs. The high degradation efficiency of PS MPs can be achieved by employing a supporting electrolyte of Na_2SO_4 (0.3 M) and applying a current intensity of 3.0 mA over 60 minutes. The GPC analysis results indicate that plasma treatment promotes chain scission and the formation of smaller molecular fragments. Furthermore, microscopy and Fourier-transform infrared spectroscopy (FTIR) analyses provide additional evidence supporting the mineralization of MPs. This transformation signifies the effective mineralization of MPs during the application of the plasma process. These analyses reveal intact MPs and no observable oxidized functional groups following the MPs' degradation process.

Based on these findings, the plasma–liquid interaction techniques hold potential as a reliable method for degrading MPs. These findings provide a foundation for future research and the development of sustainable strategies to address the global issue of microplastic pollution. However, it is important to note that further research is required to explore the scalability, cost-effectiveness, and environmental implications of plasma-based degradation techniques for microplastics. Additionally, the effects of plasma treatment on other types of microplastics and the potential byproducts resulting from the degradation processes should be thoroughly investigated. Understanding and addressing these factors are essential for optimizing the plasma treatment technique process and ensuring its successful implementation in the degradation of MPs in practical degradation applications.

4

Providing structure inputs to charged particle transport models of nonpolar liquids.

The accurate understanding of the transport properties of excess electrons in dense gases, liquids, and soft condensed matter holds significant importance for numerous technological applications. Non-polar liquid mixtures are considered fundamental for investigating the transport properties of charged particles due to their theoretical simplicity. Despite limited experimental data available for pure non-polar liquids, an entirely satisfactory theoretical framework to explain their behaviour still needs to be discovered. In liquids with high mobility, such as Ar, Kr, or Xe, it is assumed that the excess electrons can be considered nearly free to move.

The Radial Distribution Function (RDF) of noble liquid mixtures is essential for these calculations. In this study, our primary focus is on pure and binary mixtures of Ar, Kr and Xe. MD simulations have been executed employing the GROMACS [205] software package to ascertain the RDF for these systems. Our results demonstrate a strong alignment with existing molecular dynamics data, crucially validating our simulation methodology. As a prospect for future research, we aim to formulate a comprehensive theoretical model capable of explaining existing experimental observations pertaining to the transport of charged particles within non-polar liquids. Furthermore, we intend to extend our investigations to encompass calculating transport properties for charged particles within biological systems.

4.1 Introduction

The radial distribution function (RDF), also called the pair distribution function or pair correlation function (g(r)), provides information on how, on average, the atoms/molecules in a system are radially packed around each other, where it relates to the probability of finding another atom/molecule at distance "r" from a central reference atom/molecule. It is valuable for characterizing the typical structure of disordered molecular systems like liquids, where atoms are in constant motion, and a single snapshot reveals only instantaneous disorder. Having the ability to analyse the average structure is highly advantageous in such systems. RDF can be derived experimentally from X-ray or neutron diffraction studies, enabling a direct comparison between experimental observations and simulations. Moreover, when combined with the interatomic pair potential function, it allows for calculating the system's internal energy.

Calculating an RDF is a straightforward process. Begin by selecting an atom within the system and create a sequence of concentric spheres around it, with a fixed small distance (dr) between each sphere (Figure 4.1). At regular intervals, capture a snapshot of the system and tally the number of atoms within each shell, storing the results.

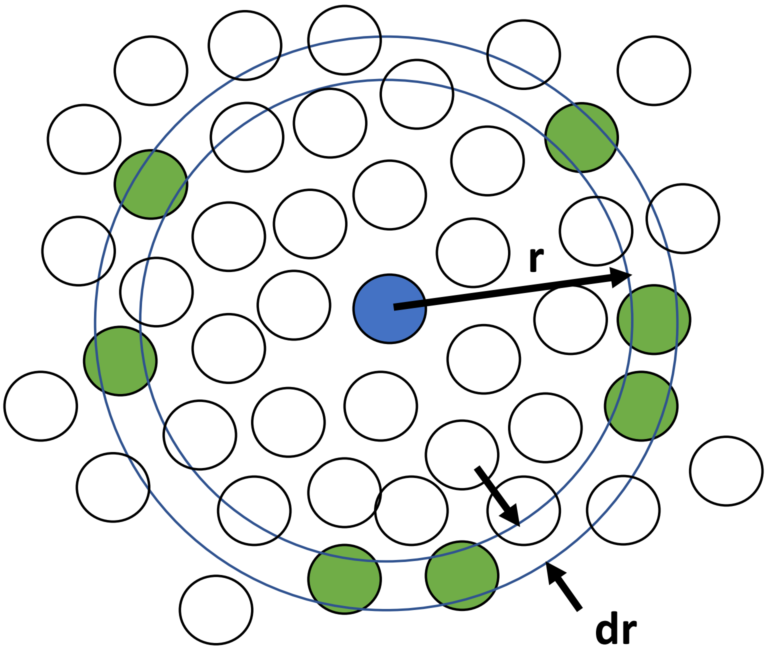

Figure 4.1: A schematic representation of an example of particle distribution in the radial distribution function measurement.

Upon completing the simulation, compute the average number of atoms within each shell. This average count is divided by the volume of each shell and the average density of atoms in the system. The outcome of this calculation represents the RDF.

In a binary component mixture, the composition and arrangements of the mixture can be described by examining the partial pair distribution functions, denoted as $g_{ab}(r)$, via [206].

$$x_a x_b n_0 g_{ab}(r) = \frac{1}{N_a + N_b} \langle \sum_{i=1}^{N_a} \sum_{j=1}^{N_b} \delta(r + r_i - r_j) \rangle \qquad \text{Equation 4.1}$$

Where r_i (r_j) represent the positions of the i^{th} (j^{th}) molecules of type (a) and (b), respectively, with N_a and N_b molecules of each type in total, the overall number density of the mixture is denoted as n_0. The relative number densities of the two species are determined by [206],

$$x_a = \frac{N_a}{N_a + N_b} \qquad \text{Equation 4.2}$$

and

$$x_b = \frac{N_b}{N_a + N_b} \qquad \text{Equation 4.3}$$

respectively.

Simply the distribution of atoms/molecules, *n(r)*, at a distance *"r"* from a central atom/molecule in volume V and total N atoms/molecules in a system can be expressed as:

$$g(r) = \frac{n(r)/dv}{N/V} \qquad \text{Equation 4.4}$$

where $dv = 4\pi r^2 dr$ and $\rho = N/V$.

The RDF offers insights into the spatial arrangement of particles within the liquid and serves as a crucial ingredient for the modification of scattering potentials, ultimately facilitating the determination of structure factors [206].

By defining the pair correlation function as;

$$h_{ab}(r) = g_{ab}(r) - 1 \qquad \text{Equation 4.5}$$

we can establish a connection between the partial pair correlation functions and the partial static structure factors, denoted as $S_{ab}(k)$, using a fourier transform;

$$S_{ab}(k) = x_a\delta_{ab} + x_a x_b n_0 \int \exp(-ik.r) h_{ab}(r) dr \qquad \text{Equation 4.6}$$

Where k is a wavevector [206].

In the case of an isotropic system, the function $S_{ab}(k)$ depends solely on the magnitude of the wavenumber, represented as $k = |k|$ and as a result, it can be expressed as [206]

$$S_{ab}(k) = x_a\delta_{ab} + x_a x_b 4\pi n_0 \int_0^{\infty} h_{ab}(r)\frac{\sin{(kr)}}{kr}r^2dr \qquad \text{Equation 4.7}$$

Scattering cross-sections, integral in determining essential transport coefficients such as drift velocity, mean energy, and longitudinal and transverse diffusion coefficients within the framework of a multi-term solution of Boltzmann's equation, are informed by microscopic inputs provided by structure factors. These structure factors contribute significantly to defining scattering cross-sections, offering essential insights into the intricate dynamics of the system. In this chapter study, our primary focus is on pure and binary mixtures of Ar, Kr and Xe. Molecular Dynamics simulations have been executed employing the GROningen MAchine for Chemical Simulations (GROMACS) software package to ascertain the RDF for these systems.

Figure 4.2 presents the flowchart detailing the complex process of calculating transport coefficients using RDF data. The RDF plays a key role in understanding how particles are arranged in a liquid, and it's instrumental in calculating the structure factor and modification of scattering potentials. This calculation and modifications, in turn, enables the calculation of scattering cross sections, which provide the microscopic information needed to compute essential transport coefficients such as drift velocity, mean energy, and longitudinal and transverse diffusion coefficients. This comprehensive approach is conducted within the framework of a multi-term solution of Boltzmann's equation.

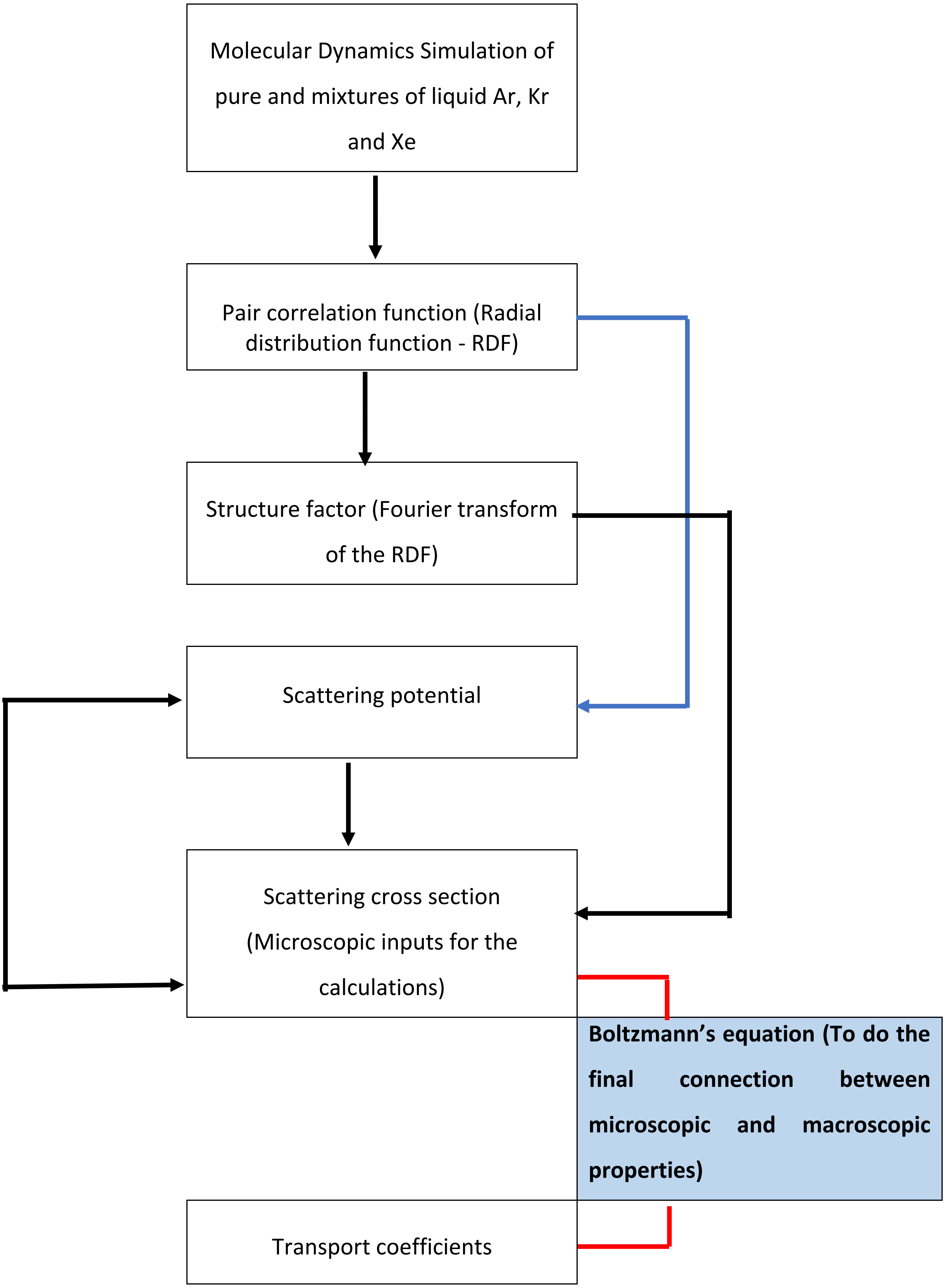

Figure 4.2: Flow chart of transport coefficient calculation using RDF.

The transition from modelling electron transport in a gaseous phase to addressing its application in the context of biological soft-condensed matter for simulating plasma-tissue interactions presents an intricate challenge. One of the most basic approximations involves scaling the findings from dilute gas phase experiments to match liquid densities. However, experimental evidence underscores the significantly greater complexity inherent in characterizing electron transport within liquid phases, even in the case of relatively simple atomic liquids and especially when considering low-energy interactions [207–210].

While there have been some experimental studies on pure non-polar liquids, it is essential to note that the available data is limited. An entirely satisfactory theoretical framework to explain their behaviour is yet to be established. Several theoretical methodologies have been devised for simulating electron transport within atomic liquids, as documented in the literature [207–214]. These theoretical frameworks typically exhibit specific limitations and are categorized into distinct models, contingent upon the intrinsic electron mobility characteristics exhibited within the dielectric liquid medium. In liquids with high mobility, such as Ar, Kr, or Xe, it is assumed that the excess electrons can be considered nearly free to move. This is because they possess relatively long mean-free paths, even though they navigate through a densely populated environment of closely packed atoms that would typically act as effective scattering centres in the gas phase [215].

The study of excess electrons in dense gases and fluids is a complex problem. The primary reasons for the complexity are the close distances between individual particles (atoms or molecules) and the strong correlations in their separations. Essentially, particles in dense systems are much closer together, and their positions are interrelated, influencing excess electrons' behaviour. De Broglie wavelengths are associated with the wave-like behaviour of particles, particularly in quantum physics. In dense systems, excess electrons, even at typical thermal energies, have de Broglie wavelengths that are much larger than the distance between atoms (interatomic spacing). This means that the electrons exhibit quantum-like behaviour due to their wave-like nature, which is significant in dense systems. In some cases, scientists use a semi-classical model that treats excess electrons as if they were point-like particles (particles with no size or extent). However, even in this simplified representation, no specific volume of space can be attributed to a single atom. In other words, in dense systems, the electrons interact with multiple atoms simultaneously, and individual atoms have no clear "ownership" of space [216].

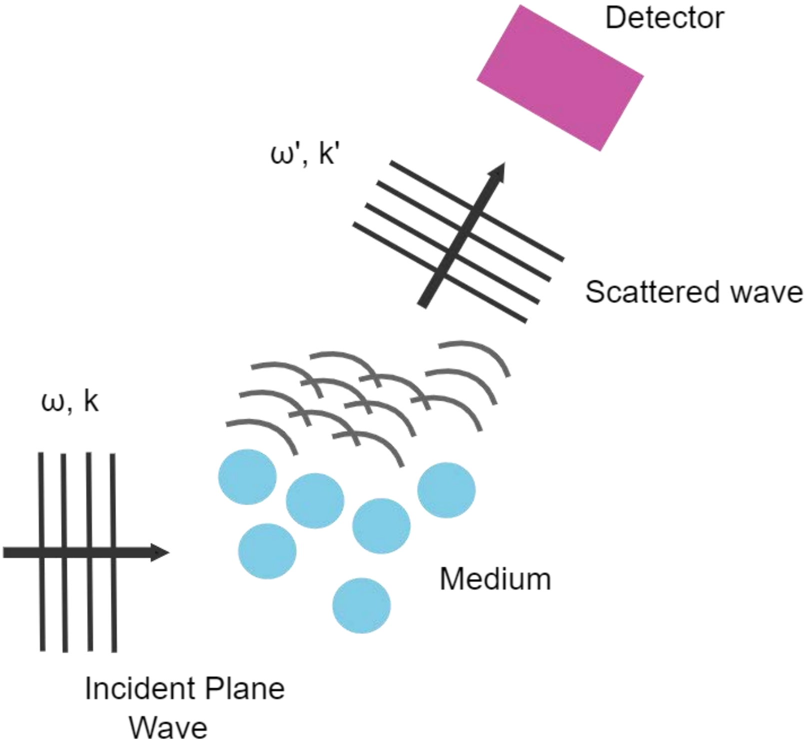

Figure 4.3: Coherent scattering of a particle (represented as plane wave of de Broglie wavelength) from a soft-condensed matter medium with shortrange order. If the average particle spacing $d \sim \lambda$; waves scattered from individual molecules interfere to produce a “diffraction” pattern at the detector [218].

In dilute gases, the movement of particles is often described as a series of individual collision events separated by the mean-free path, a measure of how far particles travel before colliding. However, this typical picture no longer holds true in dense gases and fluids. Instead, it's essential to consider the multiple scattering effects (Figure 4.3), where electrons interact with and scatter from many atoms simultaneously. This complex interaction pattern is a significant departure from the simpler collision model in dilute systems. Therefore, in liquids, correlations among the atoms cannot be ignored, and their inclusion is studied by the Cohen and Lekner [216,217].

When studying excess electrons in dense liquids, researchers need to pay special attention to two key factors: coherent scattering, which involves maintaining the phase of electron waves during scattering, and the pair correlations of the liquid, which describe how particles tend to be arranged in pairs. These factors play crucial roles in understanding the complex behaviour of excess electrons in dense systems and can have broader implications for various effects and phenomena in such environments. For the sake of simplicity, many past calculations and models have ignored the effects specific to liquids, and instead, they have represented these dense fluids as if they were dilute gases. This simplification involves making a single adjustment: increasing the density of the system [216].

Electrons, neutrons, or gamma rays as they transport through a material are subject to scattering interactions with atoms, which are inherently interconnected and thus exhibit correlations. In the realm of microscopically describing such scattering, the initial approximation employed is the "single-scatterer approximation." This approximation entails that the amplitude of scattering at any given point results from the coherent summation of amplitudes scattered by individual atoms, with the collective effect of amplitudes scattered by different atoms being considered negligible [217].

The incident wave upon each atom is approximated as a plane wave. A crucial condition for the validity of the single-scatterer approximation is that the average distance between scattering events, denoted as the mean free path (Λ), should significantly exceed the de Broglie wavelength (λ) of the electron. This same condition is evidently sufficient for the Boltzmann equation to hold. Whether the smallness of λ/Λ is a sufficient condition for the former case or a necessary condition for the latter is currently unknown. From a broader perspective, when a particle wave propagates through a liquid or a solid, it imparts energy to collective excitations within the system [217].

Within the framework of the single-scatterer approximation, all essential information regarding these excitations can be derived from the Van Hove space-time pair correlation function $G(\mathbf{R},t)$, or more directly from its Fourier transform, $S(\mathbf{K},\omega)$ [218]. The probability of an electron, neutron, or gamma ray undergoing scattering while losing momentum **K** and energy ω, is proportional to the product of the single-atom differential cross section and the spectral function $S(\boldsymbol{K},\omega)$. The determination of the spectral function typically necessitates measuring the flow of neutrons. These neutrons initially possess a certain momentum p and ϵ and subsequently emerge with modified momentum (p - K) and energy (ϵ - ω). However, S(K,ω) exhibits certain fundamental characteristics that apply universally to all quantum-mechanical systems. Among these properties, one key feature is the detailed balancing condition, which is expressed as [217].

$$S\,(-K,-\omega) = \,e^{-\beta\omega}S(K,\omega) \qquad \text{Equation 4.8}$$

Where β is equal to $1/kT$.

Although the fundamentals of incorporating temporal and spatial correlations within the liquid were well-established by Lekner and Cohen in 1967 [217], diverse approaches are available for computing the effective scattering potential perceived by electrons within the liquid medium, as evidenced by a range of methodologies outlined in previous research studies [207–209,211,212]. The foundational work was initiated by Lekner [207], who constructed the effective potential by integrating the electron-single atom potential with the pair correlation function.

Following the derivation given in Robson, White and Hilderbrandt [219] which was then generalized to mixtures by our research group to give expression for total differential scattering cross section with respect to binary mixtures including structure effects;

$$\begin{aligned}\frac{d\sigma}{d\Omega_{k'}} &= n_0\left(\frac{d\sigma}{d\Omega_{k'}}\right)_a^{lab} S_{aa}(|\Delta\mathrm{k}|) + n_0\left(\frac{d\sigma}{d\Omega_{k'}}\right)_b^{lab} S_{bb}(|\Delta\mathrm{k}|) \\ &\quad + 2n_0\sqrt{\left(\frac{d\sigma}{d\Omega_{k'}}\right)_a^{lab}\left(\frac{d\sigma}{d\Omega_{k'}}\right)_b^{lab}}\, S_{ab}(|\Delta\mathrm{k}|)\end{aligned} \qquad \text{Equation 4.9}$$

where S_{aa}, S_{bb} and S_{ab} are partial structure factors calculated from the radial distribution function data and $\frac{d\sigma}{d\Omega_{k'}}$ is the bulk differential cross-section for all molecules in the region, per unit volume. We have used the fact that $S_{ab} = S_{ba}$, and where the total number density n_0 of scattering centres has been made explicit for consistency with the normalisation of the structure factors to unit particle number.

The gas-kinetic model is developed upon the observation that excess electrons tend to travel relatively long distances without collisions in non-polar liquids, and the electric field's influence on mobility (μ) in these pure non-polar liquids closely resembles that observed in hard-sphere gases, such as helium. Therefore, this model is rooted in solving the Boltzmann equation for the momentum distribution function of excess electrons. This solution involves an expansion into Legendre polynomials centred around the direction determined by the electric field. In this approach, the collision term within the Boltzmann equation is treated using a single-scattering perspective, implying the utilization of a differential scattering cross-section throughout the analysis [215,220]. The response of electrons within a gaseous or liquid medium, when perturbed from their equilibrium state by an electric field E, can be elucidated by solving Boltzmann's equation for the phase-space distribution function, denoted as 'f' :

where,

$$\frac{\partial f}{\partial t} = v.\nabla f + \frac{eE}{m_e}.\frac{\partial f}{\partial v} = -J(f) \qquad \text{Equation 4.10}$$

Here, the variables 'v,' and 'e' and m_e represent the electron's velocity, charge and mass respectively. The collision operator $J(f)$ is responsible for modeling interactions between the electrons and the surrounding material.

The total structure modified differential scattering cross-section is given by following equation;

$$\begin{aligned}\sum(v,\theta) = \sigma_a(v,\theta)S_{aa}\left(\frac{2m_e v}{\hbar} sin\frac{\theta}{2}\right) + \sigma_b(v,\theta)S_{bb}\left(\frac{2m_e v}{\hbar} sin\frac{\theta}{2}\right) \\ + 2\sqrt{\sigma_a(v,\theta)\sigma_b(v,\theta)}S_{ab}\left(\frac{2m_e v}{\hbar} sin\frac{\theta}{2}\right)\end{aligned} \qquad \text{Equation 4.11}$$

where S_{aa}, S_{bb} and S_{ab} are partial structure factors calculated from the radial distribution function data. For more detailed information on the kinetic theory equation, please refer to works [206,207,216,217,219].

We address the impact of the high density of the liquids in our calculations through various modifications to the gas scattering properties. The initial modification involves considering the screening phenomenon, wherein the induced dipoles of all other atoms contribute to screening a single induced atomic dipole [216]. The methodology presented in this section closely parallels the approach introduced by Lekner [207].

In the dilute gas limit, the mobile electron experiences collisions with individual gas atoms, essentially operating in isolation from the remaining gas atoms. Within this collision, the electron induces a series of multipole moments in the atom. These induced moments interact with the electron through a charge-multipole potential, giving rise to the polarization potential, denoted as $U_p(r)$. In a dilute gas, the potential's range, produced by these induced multipole moments, is relatively small compared to the significant interatomic spacing. Hence, it is a reasonable approximation to disregard their impact on other atoms. However, at higher gas or liquid densities, numerous atoms can possess a non-negligible induced set of multipole moments originating from both the mobile electron and all other atoms in the bulk. The effective charge-multipole polarization potential experienced by the electron at any specific location (r_e) is then the cumulative sum of the polarization potentials originating from all atoms [216].

Boyle and colleagues [216] considered the impact arising solely from the induced dipoles of atoms by extending the work done by Lekner, establishing the effective polarization of an individual atom in a self-consistent manner. Initially, they assumed that the induced dipole strength for each atom in the bulk can be expressed as $f(r)\alpha_d(r)e/r^2$ where *r* represents the distance between the electron and the atom, $\alpha_d(r)$ denotes the external dipole polarizability resulting from the electron interaction, and $f(r)$ incorporates polarization screening, necessitating determination. This straightforward multiplicative factor remains valid as long as average over the atomic distribution. In the dilute-gas scenario, a safe approximation is $f(r) = 1$, while in the dense case, a self-consistent expression for $f(r)$ becomes imperative. By selecting a specific "focus atom" i at the position r_i defining $r = r_e -$

r_i, and assuming the coefficient $f(r)$ is known for all other atoms denoted as $f_{bulk}(r)$, they subsequently calculated the dipole strength for atom i and can be given as follows [216],

$$f_i(r) = 1 - \pi N \int_0^{\alpha} ds \frac{g(s)}{s^2} \int_{|r-s|}^{r+s} dt \Theta(r,s,t) \frac{\alpha_d(t) f_{bulk}(t)}{t^2} \qquad \text{Equation 4.12}$$

Derived through bipolar coordinates, denoted as *s* and *t*, the expression involves *N*, the density of the bulk, *g(s)*, representing the isotropic pair correlator of the bulk, and an additional factor [216]:

$$\Theta(r,s,t) = \frac{3}{2} \frac{(s^2 + t^2 - r^2)(s^2 + r^2 - t^2)}{s^2} + (r^2 + t^2 - s^2) \qquad \text{Equation 4.13}$$

The origin of this factor stems from the configuration of the electric field of a dipole. The integrations over *s* and *t* encapsulate the influence of an atom positioned at a distance s from atom *i* and a distance *t* from the electron. The likelihood of locating an atom is dictated by $g(s)$, highlighting that Equation 4.12 approximates the precise polarization through an ensemble average across all atomic configurations, with one atom positioned at r_i. In this approximation, the polarization consistently aligns along the vector $\hat{r}$ connecting the focus atom and the electron [216].

The self-consistent resolution of Equation 4.12 is achieved by equating $f_{bulk}(r) = f_i(r)$ and iteratively solving for $f_i(r)$. The central component in Equation 4.12 is the pair correlator, representing the subsequent order in the particle distribution within the bulk beyond the average density. In Lekner's [207] computation, the pair correlator adopted the analytical solution of the Percus-Yevick model for computational simplicity. In the approach given by Boyle and colleagues [216], they extended this by utilizing Yarnell's experimental measurements [221] for a more precise depiction of correlations [216].

Using the pair correlator, then we can calculate a self-consistent computation of the screening function, denoted as $f(r)$. While this screening factor technically pertains to the dipole term alone, Boyle and his team's [216] treatment involves a more intricate form of the polarization term compared to Lekner's [207] initial consideration. However, recognizing that the dominant contribution to the polarization stems from the dipole term, they have opted to extend the screening factor $f(r)$ to the entire polarization potential. Consequently, accounting for the screening effect, the modified polarization potential, denoted as $\widetilde{U}_p(r)$, for an electron interacting with a single atom in a dense fluid is expressed as

$$\widetilde{U}_p(r) = f(r)U_p(r) \qquad \text{Equation 4.14}$$

It's worth noting that, unlike Lekner [207], who exclusively employed the static dipole polarizability Boyle's [216] more accurate depiction of the atom-electron interaction, as detailed in their paper, has already introduced a radial dependence in the polarization potential $U_p(r)$ extending beyond a potential with asymptotic behavior r^{-4}. The screening effect has therefore induced a density-dependent further adjustment to $U_p(r)$.

To input data into the kinetic theory, it is imperative to have appropriate cross-sections that account for the scattering of electrons from a single "focus atom" within the bulk. As discussed in the Boyle's [216] work, the polarization interaction between the electron and the focus atom is influenced by the presence of other atoms, leading to screening effects. However, there is a more apparent consequence arising from the neighbouring atoms in the bulk: their interaction with the electron remains substantial even when the electron is near the focus atom. Following the approach outlined by Lekner [207] Boyle and colleagues [216] construct an effective potential that the electron encounters throughout a single scattering event and delineate the definition of "a single scattering event." While adhering to the foundational principles of Lekner [207], they [216] adopted a distinct methodology for calculating the cross-sections.

The composite effective potential can be denoted as $U_{eff} = U_1 + U_2$ consists of two components: $U_1(r)$, representing the direct interactions with the focus atom, and $U_2(r)$, accounting for the interaction between the electron and the remaining bulk. Given the impracticality of precisely handling configurations of atoms in the bulk, the external potential $U_2(r)$ can be expressed by once again computing the ensemble average [216];

$$U_2(r) = \frac{2\pi N}{r}\int_0^{\infty} dtU_1(t)\int_{|r-t|}^{r+t} ds\, sg(s) \qquad \text{Equation 4.15}$$

The rearrangement of the integration order in Equation 4.15 for numerical convenience differs from that in Equation 4.12. It's worth noting that utilizing the ensemble average brings the advantage of ensuring the spherical symmetry of the total effective potential, U_{eff}. Throughout the computation of Equations 4.12 and 4.15 we incorporate the parameter σ_{core}, representing the hard-core exclusion diameter for the distribution of atoms in the bulk. Specifically, the probability for two atoms to approach within a distance σ_{core} is extremely small [216]. For Ar, $\sigma_{core} \approx 6a_0$. Furthermore, Boyle and colleagues [216] beyond Lekner's [207] analysis by incorporating the influence of exchange terms in the bulk.

Then they solved the scattering properties, specifically the cross-sections, arising from such a collision process. They assumed it is reasonable to derive cross-sections through the phase shifts in a partial wave expansion. To determine these phase shifts, Lekner [207] opted to shift the effective potential by an amount U_0 such that $U_{eff}(r_m) + U_0 = 0$. Subsequently, Lekner set the potential $U_{eff}\ (r > r_m) = 0$, matching it to the asymptotic form of each partial wave conventionally. In contrast, Boyle choosed to maintain the potential unaltered but calculate the phase shift at the point r_m. This approach is equivalent to computing the "phase function" at the point r_m, which involves setting $U_{eff}\ (r > r_m) = 0$ and matching it to the asymptotic form of the wavefunction. They believed this method more accurately represents the available energy states in the bulk. This cross-section, encompassing external contributions and screening effects, is denoted as $\sigma^{SCT}(\epsilon, \chi)$ [216].

According to the assumption that $g(s) = 0$ for $s < \sigma_{core}$ the calculation of the potential limited to a distance of $r_m \approx \frac{2}{3}\sigma_{core}$, the integral over *t* in Equation 4.15 is non-zero only for $t \geq \frac{1}{3}\sigma_{core \approx 2a_0}$.Within these ranges, the predominant contribution to the potential arises from the polarization component. It's important to note that the values of $\overline{W}_{P,2}$ and $\overline{W}_{Q,2}$ are not well behaved at larger distances, prompting to set them to zero for $r > \sigma_{core}/2$. Calculations are conducted neglecting the contribution of of $\overline{W}_{P,2}$ and $\overline{W}_{Q,2}$ to the bulk and compared them to the full calculations. The results indicated minimal differences in the high-energy regime of the resulting cross-sections and a modest discrepancy of up to *5%* otherwise. While this alteration had a small impact, it was not negligible, especially concerning the deviation in transport properties [216].

In this study, our primary objective was to employ advanced computer simulation techniques to model electron mobility within non-polar liquid mixtures. We aimed to provide a precise and comprehensive depiction of charged particle transport phenomena in soft condensed matter systems. To confirm the accuracy of our simulations and their real-world usefulness, we are in the process of comparing our findings with the documented experimental data by Borghesani and colleagues [215]. This fusion of computer modeling and real-world observations will be a central component of our research, with the potential to provide valuable insights into the complex behaviors of electron mobility in non-polar liquid mixtures.

Over numerous decades, computer simulation has evolved into an essential instrument for investigating fluid behaviour. A notable focus of simulation research has been anticipating thermodynamic characteristics in mixtures. The convenience of conducting numerical simulations with noble gases and their combinations is facilitated by their spherical shape, simplicity, and stability. Notably, experimental data related to the thermodynamic and structural attributes of noble gas-involved mixtures is either scarce or entirely absent, thereby imposing additional constraints on simulation investigations concerning these mixtures.

The Molecular Dynamics study of binary mixtures originated in the 1960s. Rotenberg conducted the first computer simulation investigation for the equation of state pertaining to an equimolar binary mixture characterized by nearly identical hard spheres, employing the Monte Carlo method [222]. Subsequently, during the 1970s, a comprehensive series of computations was undertaken to assess the excess thermodynamic properties of mixing in Lennard-Jones mixtures [223,224]. Following this, numerous molecular dynamics studies on transport coefficients within binary fluid mixtures have been documented. Pas and Zwolinski [225] employed molecular dynamics simulations to investigate binary combinations involving Ar-Kr, Ar-Xe, and Kr-Xe in a liquid state. Their simulations assumed that these fluids consisted of Lennard–Jones (6–12) particles. Balcells et al. [226] conducted molecular dynamics (MD) simulations of an Ar and Kr mixture at conditions of 12 MPa and 135 K. In most of these investigations, the outcomes were juxtaposed with prior theoretical studies, with no corresponding comparisons drawn to experimental data. These studies consistently yielded a favourable agreement, thereby affirming the establishment of a fundamental approach for calculating transport coefficients via molecular dynamics simulations.

In this study, we conducted a benchmarking analysis using molecular dynamics simulations to assess the existing experimental data pertaining to liquid Ar-Kr and Ar-Xe mixtures. Our focus was explicitly on comparing our results with the experimental findings of Borghesani [215]. Building upon the foundational contributions of Lekner previously mentioned, particularly regarding the pair correlation function as outlined previously, the determination of the pair correlation function (Radial Distribution Function - RDF) becomes paramount in our calculations concerning noble liquid mixtures. The RDF is a fundamental tool in unravelling the intricate spatial arrangements and intermolecular correlations within these mixtures, enabling a deeper understanding of their thermodynamic and structural characteristics.

4.2 Methodology

4.2.1 Molecular Dynamics Simulation of pure and mixtures of liquid Ar, Kr and Xe

Molecular Dynamics (MD) has been performed to compute the Radial Distribution Function (RDF, Pair Correlation function) of pure and binary mixtures of Ar, Kr, and Xe as the primary species of interest at different temperatures and compositions using Lenard-Jones (LJ) potentials in the liquid phase. The mixture interactions between unlike atoms are treated by using the Lorentz-Berthelot mixing rules. These noble gases were deliberately chosen as they represent ideal model systems for investigating fundamental liquid behaviours due to their simplicity and ease of modelling. The rationale underpinning

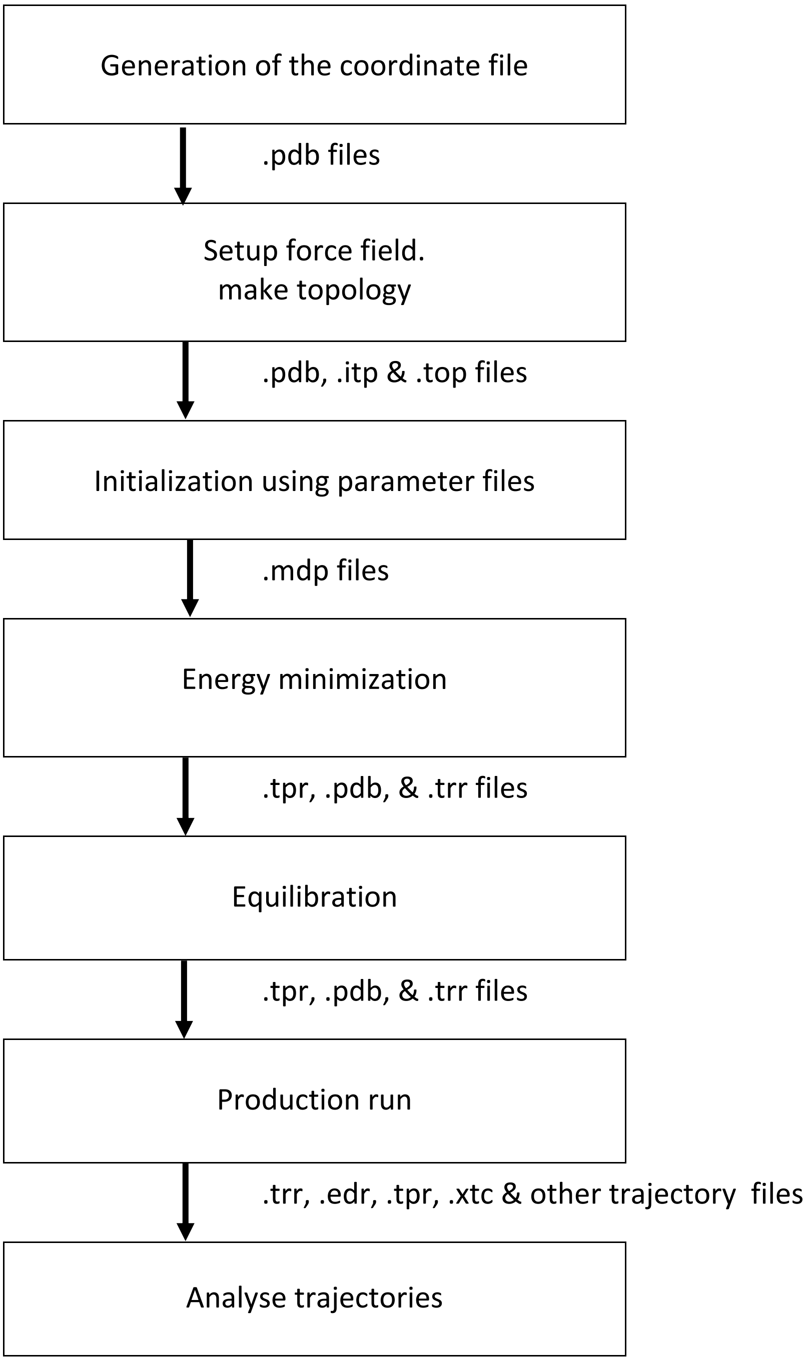

Figure 4.4: Basic steps of molecular dynamics simulation with GROMACS and the most important file types that are generated along the steps.

this choice is to establish a robust foundation, commencing with elemental systems of minimal intricacy, such as Ar, Kr, and Xe, before embarking upon more intricate investigations involving complex fluids, including aqueous and biological systems. Subsequently, we intend to extend our investigations to more intricate systems, such as water and biological substances, thus allowing for a comprehensive exploration of molecular dynamics across a spectrum of complexities. All the systems contain a unique number of atoms. The particles were located randomly to ensure the system was mixed. A set of twelve different models was utilized to derive accurate simulation models aligned with previously available experimental data. Detailed information on the simulation models is tabulated in Table 4.1. A run time of 50,000-time steps was used to equilibrate the mixture. The production run of the simulation consists of 5 000 000-time steps to give a total run of 5 050 000-time steps.

Figure 4.4 overviews the fundamental molecular dynamics simulation process using GROMACS (version 2021.2). This process generates several important file types during its various stages. It is worth noting that the primary output of molecular dynamics (MD) simulations is the positions and velocities of all atoms obtained through the solution of motion equations. Subsequently, these trajectory data are the basis for calculating thermodynamic properties during the subsequent analysis phase. Molecular simulations follow a relatively straightforward procedure, although they require careful consideration of numerous details. The subsequent sections will explain the steps involved and describe relevant commands.

4.2.1.1 Generation of the coordinate files

The initial step in this simulation was involved with the generation of the system's coordinates. The atomic system's initial coordinates were obtained using the FORTRAN code in this work (relevant FORTRAN code can be found in lattice.f of SI - APPENDIX C). As the output of this code, the .pdb file contains vital information regarding atom types, their positions, and connectivity within the system.

4.2.1.2 Setup force field and make topologies.

The subsequent stage involved the set-up of the force field and the creation of the "topology," which is a critical step in preparing the simulation as it dramatically impacts the results' quality. The Optimized Potentials for Liquid Simulations (OPLS) (1.3.2 Introduction to MD Methodology) force field was used in this study. Setting up the force field entails defining the parameters in the OPLS potential function for each "atom type". The .pdb file created in the previous step was read in this step and converted the coordinates file to a topology file.

Table 4.1: Summy of key parameters of the simulation setup, including the number of atoms, number density, the ratio of atoms, temperature, and the simulation cell size.

Number of Atoms	Number Density (N) / cm^{-3}	The ratio of the atoms	Temperature / K	Simulation cell size/nm
2744	2.13×10^{22}	100% Ar	85	5.0505 x 5.0505 x 5.0505
1728	1.42×10^{22}	100% Xe	165	4.9555 x 4.9555 x 4.9555
2197	1.72×10^{22}	100% Kr	120	5.036 x 5.036 x 5.036
2744	2.13×10^{22}	1 Xe : 2743 Ar	87.4	5.0505 x 5.0505 x 5.0505
2744	2.13×10^{22}	5% Xe : 95% Ar 137 Xe : 2607 Ar	87.4	5.0505 x 5.0505 x 5.0505
2744	2.13×10^{22}	50% Xe : 50% Ar 1372 Xe : 1372 Ar	87.4	5.0505 x 5.0505 x 5.0505
2744	2.13×10^{22}	2.5% Xe : 97.5% Ar 69 Xe : 2675 Ar	87.4	5.0505 x 5.0505 x 5.0505
2744	2.13×10^{22}	1% Xe : 99% Ar 27 Xe : 2717 Ar	87.4	5.0505 x 5.0505 x 5.0505
2744	2.13×10^{22}	1 Kr : 2743 Ar	87.4	5.0505 x 5.0505 x 5.0505
2744	2.13×10^{22}	10% Kr : 90% Ar 274 Kr : 2470 Ar	87.4	5.0505 x 5.0505 x 5.0505
2744	2.13×10^{22}	50% Kr : 50% Ar 1372 Kr : 1372 Ar	87.4	5.0505 x 5.0505 x 5.0505
2744	2.13×10^{22}	20% Kr : 80% Ar 549 Kr : 2195 Ar	87.4	5.0505 x 5.0505 x 5.0505

The GROMACS library contains several files, namely atomtypes.atp (atp = atom type parameter file), ffnonbonded.itp (itp = include topology), and ffbonded.itp, (Exemplary files for the atomtypes.atp and ffnonbonded.itp are given in Figure S4.2 of SI - APPENDIX C) provide a collection of force field parameters from the literature. These files play a crucial role in the simulation setup. Atomtypes.atp describes the different atom types, with each type assigned a distinct name or number and corresponding mass (a.m.u.), while ffnonbonded.itp and ffbonded.itp lists the parameters for non-bonded and bonded potential functions, respectively. The set of non-bonded parameters includes van der Waals parameters V ($c6$ or σ, depending on the combination rule) and W ($c12$ or ϵ), specified in the file ffnonbonded.itp. A detailed description of the combination rule can be found in Chapter 01.

The topology (.top) file is a comprehensive dataset encompassing all constant attributes relevant to a molecular system. These attributes include references to force field parameter files, the functional terms of the force field, and the quantities of all species. In contrast, dynamic attributes like positions and velocities generated during the simulation are stored separately in coordinate and trajectory files. Figure S4.2 (SI - APPENDIX C) visually represents the references in the topology file, aiming to facilitate a more comprehensive understanding of the topology file structure in GROMACS. In this step, it becomes necessary to determine the number of molecules/atoms to be simulated. Modifying this quantity alters the statistical impact on the outcomes, affecting the overall quality of the generated data. Conversely, employing more molecules/atoms will result in longer computation times. Consequently, this choice always involves striking a balance and requires informed judgment and refinement studies.

The dimensions of the box were systematically reduced until the graphical representations exhibited minimal sensitivity to alterations, while maintaining alignment with the available experimental data. This was satisfactory for our purposes rather than any strict convergence testing. Future iterations of this study may incorporate an automated iterative process to evaluate subsequent computations, ensuring conformity within predefined tolerance thresholds.

The LJ parameters (ϵ and σ) for pure Ar, Kr and Xe have been given in Table 4.2. The mixture interaction requires the use of the Lorentz-Berthelot combining rules (Chapter 01 – equation 1.12 and 1.13) to determine the cross-interaction parameters, namely ϵ_{ij} and σ_{ij}.

Table 4.2: Lennard-Jones potential parameters used in this work [227].

Liquid	**ϵ/k (K)**	**σ (Å)**	**Mass (a.m.u.)**
Ar	117.7	3.401	39.94800
Kr	159.5	3.624	83.79800
Xe	217.9	3.935	131.29300

4.2.1.3 Initialization using parameter files

Molecular Dynamics (MD) simulations can be conducted under various conditions, for different time scales, and employing diverse algorithms to solve the equations of motion, among other factors. GROMACS provides the flexibility to specify multiple parameters to cater to specific simulation requirements. These parameters are to be included in a designated file known as the Molecular Dynamics parameters file (.mdp file), which is a straightforward text file with the .mdp extension. Subsequently, this .mdp file serves as input to the gmx grompp module, facilitating the compilation of a .tpr file, which is essential for executing the MD simulation. A sample .mdp file is given in SI – APPENDIX C.

4.2.1.4 Energy minimization

Despite efforts to avoid overlapping atom shells, the insertion procedure may still lead to undesirable arrangements of molecules. Therefore, performing an energy minimization, a specific type of concise and robust simulation, proves beneficial in identifying an optimal starting point for the actual MD simulation.

This energy minimization process utilized the steepest descent method. This algorithm guides the movement of atoms along the direction of the most substantial forces until one of the specified stopping criteria is met. As the minimization continues, the potential energy quickly drops and becomes significantly negative. This is a positive sign, indicating that the atoms have reached the right distances from each other. This means the system is now ready for the molecular dynamics simulation.

4.2.1.5 Equilibration

Equilibration is a setup trial for the molecular dynamic simulation process. Once the three consecutive energy minimization steps were done this equilibration run was carried out for about 50 ps. This is a short MD run. The main idea of this step is to introduce intermolecular forces to the system and equilibrate it to the desired temperature and pressure. At the same time, the single atoms establish a proper orientation around each other.

This step was carried out by doing some modifications to the .mdp file. The integrator was modified to 'md' from 'steep' to indicate the beginning of the MD run.

4.2.1.6 Production run

The data gathered during this step serves as the basis for our analysis. To begin with, an initial molecular dynamics (MD) simulation was performed on the equilibrated system, extending over a period of ten nanoseconds (10 ns). This simulation comprised 5,000,000 steps, each lasting 0.001 picoseconds (ps).

4.2.1.7 Analyze trajectories

In addition to conducting molecular simulations, GROMACS offers tools for the analysis of generated trajectory and energy data. Some key functions include 'gmx_mpi energy' and 'gmx_mpi density.' Furthermore, advanced analysis capabilities, such as pair correlation functions, are also available. 'gmx_mpi energy' allows for the computation of various quantities, including pressure, temperature, total density, and energies. On the other hand, 'gmx_mpi density' calculates the time-averaged density distribution of a specific component within the simulation box, providing insights into parameters like mole fractions and distribution coefficients. For a comprehensive understanding of GROMACS' analysis functions, a detailed overview is available in [205].

4.3 Results and Discussion

To establish the credibility of our RDF calculations, we have generated plots representing the RDF of a mixture containing equal amounts of Ar and Kr, employing the LJ potential with parameters set at 115.8K and σ* = 0.80004 for Ar–Ar, Ar–Kr, and Kr–Kr interactions. These plots are presented in Figure 4.5 – 4.7, and we have compared our findings with results obtained through conformal-solution theory [228], Percus-Yevick [229], molecular dynamics computations as reported by Jacucci and McDonald [230] and molecular dynamics data reported by Moosavi and Goharshadi [229]. It is evident from the figures that our results exhibit a high level of concurrence with the outcomes reported by Jacucci and McDonald [229] and Moosavi and Goharshadi [228].

In contrast to previous molecular dynamics simulations, specifically those conducted by Jacucci and McDonald [229] and Moosavi and Goharshadi [228], our results show differences. These variations might be due to the use of different force fields in their research compared to ours. We were unable to obtain detailed information about the specific force field they used. As part of our future research, we intend to undertake a benchmarking process, employing alternative force fields to compare our results with those of their work. This effort aims to shed light on the sources of variation and enhance the understanding of the underlying molecular dynamics.

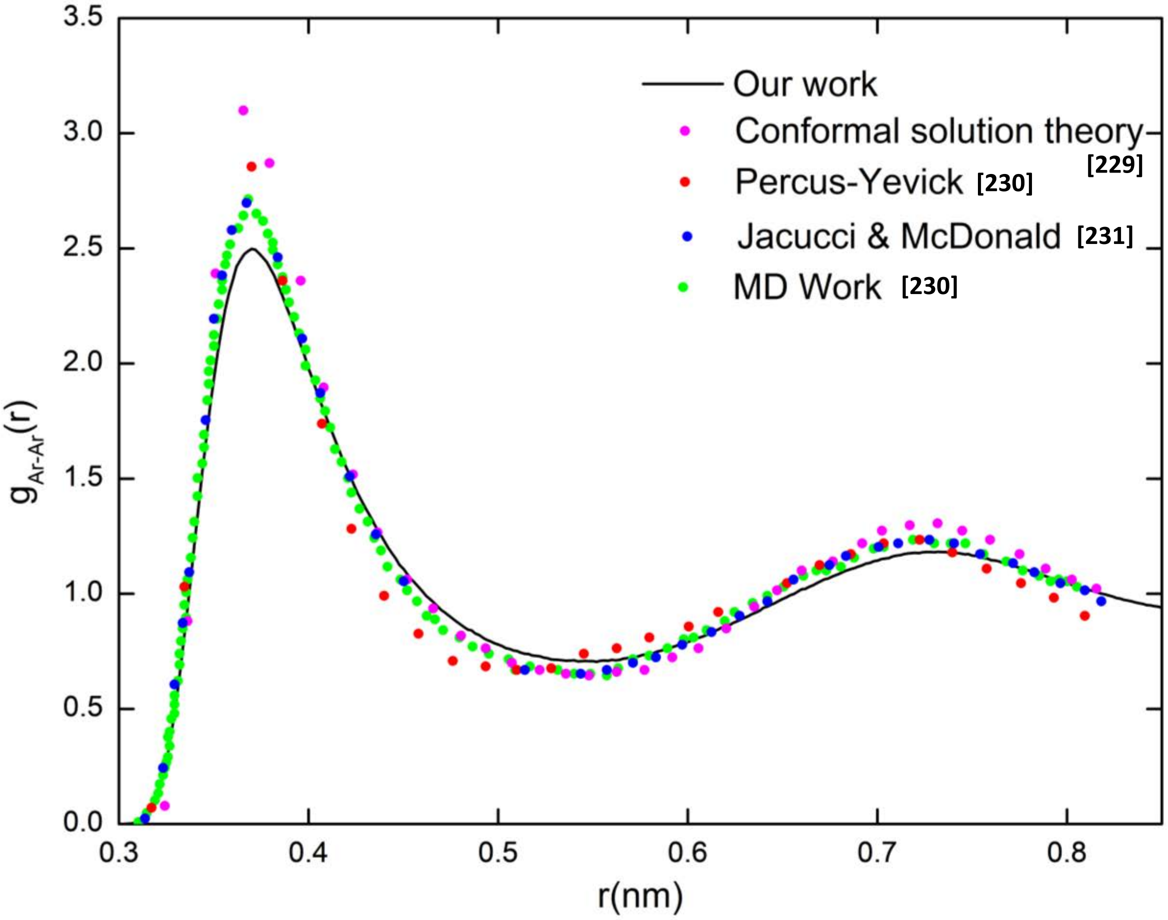

Figure 4.5: RDF of an equimolar mixture of Ar–Kr at 115.8 K for Ar–Ar, obtained by different methods: conformal-solution theory [227], Percus-Yevick [228], molecular dynamics computations as reported by Jacucci and McDonald [229] and molecular dynamics data reported by Moosavi and Goharshadi [228].

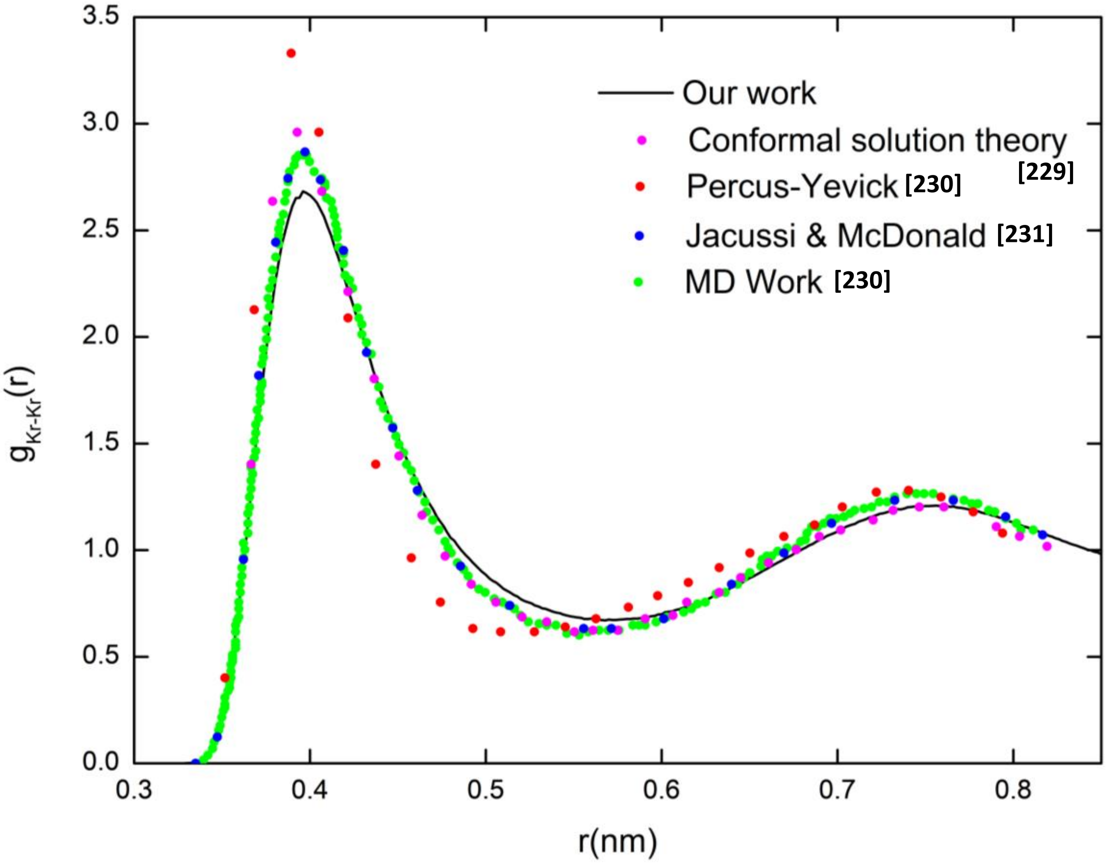

Figure 4.6: RDF of an equimolar mixture of Ar–Kr at 115.8 K for Kr–Kr, obtained by different methods: conformal-solution theory [227], Percus-Yevick [228], molecular dynamics computations as reported by Jacucci and McDonald [229] and molecular dynamics data reported by Moosavi and Goharshadi [228].

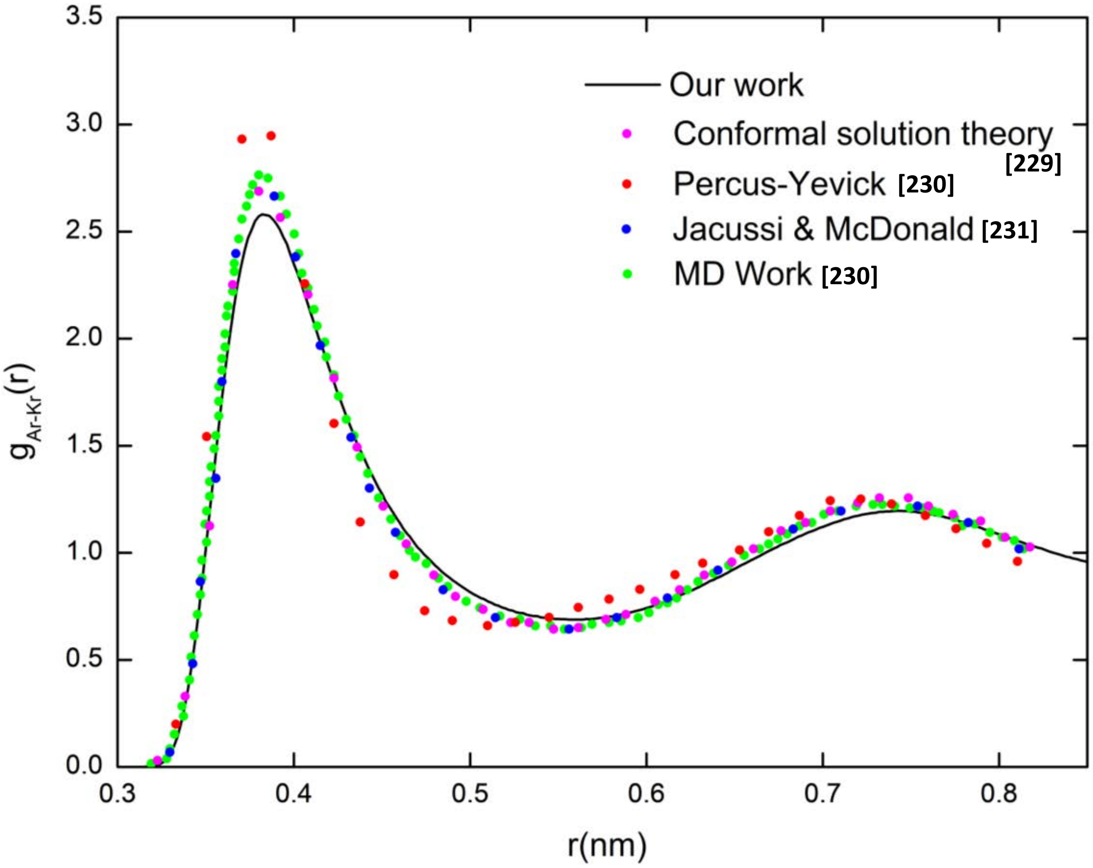

Figure 4.7: RDF of an equimolar mixture of Ar–Kr at 115.8 K for Ar–Kr, obtained by different methods: conformal-solution theory [227], Percus-Yevick [228], molecular dynamics computations as reported by Jacucci and McDonald [229] and molecular dynamics data reported by Moosavi and Goharshadi [228].

Figures 4.8 to 4 .10, we present our research findings pertaining to radial distribution functions (RDFs), which were calculated using the Lennard–Jones potential. The primary aim of our investigation is to conduct a benchmarking analysis through molecular dynamics simulations, with the purpose of evaluating existing experimental data concerning mixtures of liquid Ar-Kr and Ar-Xe.

For instance, in Figure 4.8, we showcase the RDFs for pure Ar, Kr, and Xe at three different temperatures. The peaks in the Radial Distribution Function (RDF) plot are visibly moving towards the greater interatomic distances. This shift is primarily attributable to the larger σ (Lennard-Jones parameter) values associated with Xe when compared to Kr, and the larger σ value of Kr in comparison to Ar (as detailed in Table 4.2).

Elevated maxima and reduced minima in the RDF peaks of Figure 4.9 and Figure 4.10 indicate a more ordering of liquid particles in the system, which becomes apparent as the mole fraction of Ar decreases while maintaining a constant temperature and density. This observed phenomenon underscores the ordering influence of Xe and Kr on the spatial distribution of atoms, primarily attributed to the greater depth of the Xe and Kr potential well compared to that of Ar.

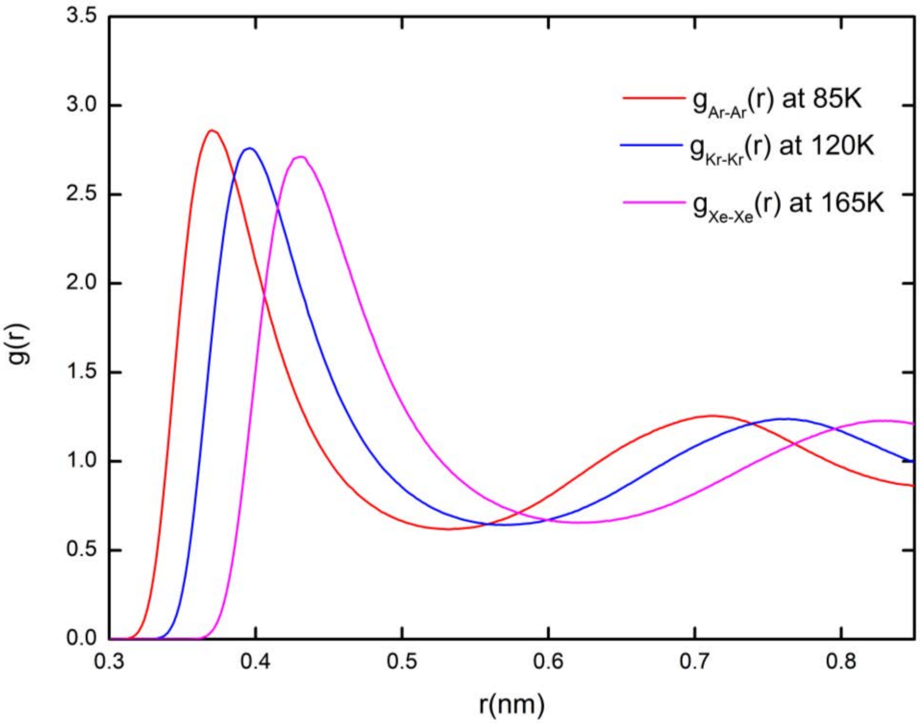

Figure 4.8: Radial Distribution Function of Pure mixtures of Ar (85 K), Kr (120 K) and Xe (165 K) calculated using Lennard–Jones potential.

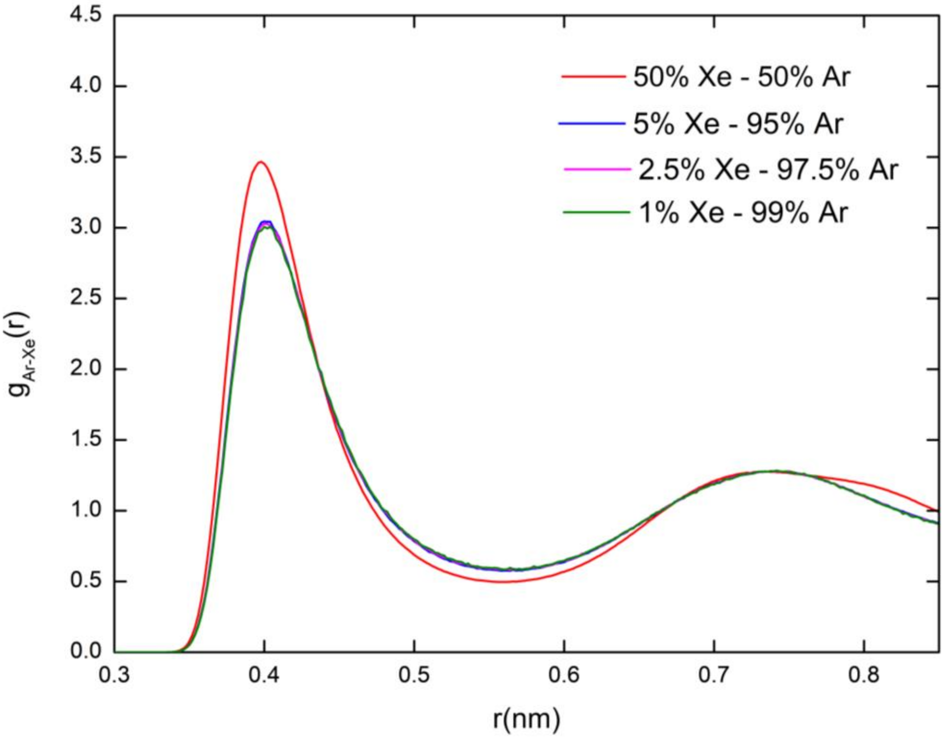

Figure 4.9: $g_{Ar–Xe}$ versus r (nm) at temperature 87.4 K at different compositions calculated using Lennard–Jones potential.

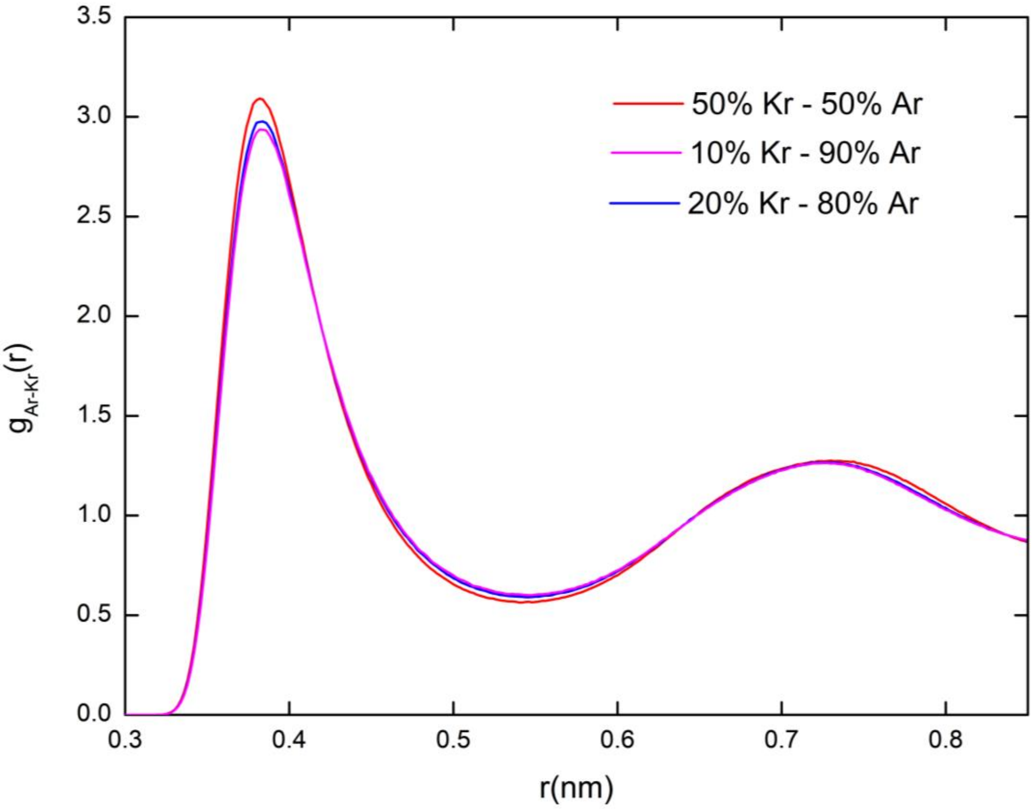

Figure 4.10: g_{Ar-Kr} versus r (nm) at temperature 87.4 K at different compositions calculated using Lennard–Jones potential.

Furthermore, as depicted in Figure 4.9 and 4.10, it becomes evident that the positions of the RDF peaks remain unaffected by changes in the mixture composition when temperature and density are held constant. In essence, the shifts in peak locations are negligible in this scenario due to the relatively similar sizes of Ar and Xe. It appears that noticeable peak displacements only occur in mixtures comprising molecules with significantly contrasting interactions. This observation aligns with the research conducted by Hoheisel and Deiters [230], who investigated a mixture of Ne and Kr. Their findings indicated a distinct shift in the RDF peaks, particularly in the second peak of the RDF of this mixture. This shift can be attributed to the substantial disparity in the sizes of the components in this mixture and is notably positive, causing the peaks to move towards greater interatomic distances with an increasing mole fraction of Kr.

4.4 Conclusion

We carried out molecular dynamics simulations to investigate the radial distribution function (RDF) for a variety of noble gas combinations, such as Ar-Ar, Kr-Kr, Xe-Xe, as well as mixtures like Ar-Xe and Ar-Kr. These simulations were built upon Lennard-Jones potentials and encompassed a spectrum of compositions. Particularly, our analysis of the RDF for Ar-Kr and Ar-Xe blends revealed that modifications to different parameters had varying impacts on the positions and amplitudes of the RDF peaks. These observations shed light on the ordering tendencies within these fluid mixtures. Future works will be carried out to develop a satisfactory theoretical explanation for the available experimental data of the charged particle transport in nonpolar liquids and calculate transport properties of charged particles in biological systems.

Reference

[1] M. Witzke, P. Rumbach, D. B. Go, and R. M. Sankaran, *Erratum: Evidence for the Electrolysis of Water by Atmospheric-Pressure Plasmas Formed at the Surface of Aqueous Solutions*, J Phys D Appl Phys **46**, 129601 (2013).

[2] P. E. Grabowski et al., *Review of the First Charged-Particle Transport Coefficient Comparison Workshop*, High Energy Density Phys **37**, 100905 (2020).

[3] F. F. Chen, *Introduction to Plasma Physics and Controlled Fusion*, 3rd ed. (Springer International Publishing, 2016).

[4] A. Ferdman and L. A. Kennedy, *Plasma Physics and Engineering*, First (CRC Press, Boca Raton, 2014).

[5] J. A. Bittencourt, *Fundamentals of Plasma Physics*, 3rd ed. (Springer New York, New York, NY, 2004).

[6] M. Laroussi, *Low-Temperature Plasmas for Medicine?*, IEEE Transactions on Plasma Science.

[7] B. M. Penetrante[2], R. M. Brusasco, B. T. Merritt, and G. E. Vogtlin, Environmental Applications of Low-Temperature Plasmas*, 1999.

[8] I. Adamovich et al., *The 2017 Plasma Roadmap: Low Temperature Plasma Science and Technology*, J Phys D Appl Phys **50**, 323001 (2017).

[9] M. D. Calzada, M. Moisan, A. Gamero, and A. Sola, *Experimental Investigation and Characterization of the Departure from Local Thermodynamic Equilibrium along a Surface-wave-sustained Discharge at Atmospheric Pressure*, J Appl Phys **80**, 46 (1996).

[10] J.-S. Chang, P. A. Lawless, and T. Yamamoto, *Corona Discharge Processes*, IEEE Transactions on Plasma Science **19**, 1152 (1991).

[11] T. C. Montie, K. Kelly-Wintenberg, and J. R. Roth, *An Overview of Research Using the One Atmosphere Uniform Glow Discharge Plasma (OAUGDP) for Sterilization of Surfaces and Materials*, IEEE Transactions on Plasma Science **28**, 41 (2000).

[12] S. Y. Moon, W. Choe, and B. K. Kang, *A Uniform Glow Discharge Plasma Source at Atmospheric Pressure*, Appl Phys Lett **84**, 188 (2004).

[13] P. K. Chu and X. Lu, editors , *Low Temperature Plasma Technology* (CRC Press, 2013).

[14] N. De Geyter and R. Morent, *Nonthermal Plasma Sterilization of Living and Nonliving Surfaces*, Annu Rev Biomed Eng **14**, 255 (2012).

[15] M. J. Pavlovich, Z. Chen, Y. Sakiyama, D. S. Clark, and D. B. Graves, *Effect of Discharge Parameters and Surface Characteristics on Ambient-Gas Plasma Disinfection*, Plasma Processes and Polymers **10**, 69 (2013).

[16] R. J. Zaldivar, J. P. Nokes, P. M. Adams, K. Hammoud, and H. I. Kim, *Surface Functionalization without Lattice Degradation of Highly Crystalline Nanoscaled Carbon Materials Using a Carbon Monoxide Atmospheric Plasma Treatment*, Carbon N Y **50**, 2966 (2012).

[17] W. Liu, J. Zhan, Y. Su, T. Wu, C. Wu, S. Ramakrishna, X. Mo, S. S. Al-Deyab, and M. El-Newehy, *Effects of Plasma Treatment to Nanofibers on Initial Cell Adhesion and Cell Morphology*, Colloids Surf B Biointerfaces **113**, 101 (2014).

[18] J. Park, I. Henins, H. W. Herrmann, G. S. Selwyn, J. Y. Jeong, R. F. Hicks, D. Shim, and C. S. Chang, *An Atmospheric Pressure Plasma Source*, Appl Phys Lett **76**, 288 (2000).

[19] H. L. Chen, H. M. Lee, S. H. Chen, and M. B. Chang, *Review of Packed-Bed Plasma Reactor for Ozone Generation and Air Pollution Control*, Ind Eng Chem Res **47**, 2122 (2008).

[20] T. A. Kareem and A. A. Kaliani, *Glow Discharge Plasma Electrolysis for Nanoparticles Synthesis*, Ionics (Kiel) **18**, 315 (2012).

[21] N. Saito, J. Hieda, and O. Takai, *Synthesis Process of Gold Nanoparticles in Solution Plasma*, Thin Solid Films **518**, 912 (2009).

[22] X. Xu, *Dielectric Barrier Discharge — Properties and Applications*, Thin Solid Films **390**, 237 (2001).

[23] T. C. Corke, C. L. Enloe, and S. P. Wilkinson, *Dielectric Barrier Discharge Plasma Actuators for Flow Control*, Annu Rev Fluid Mech **42**, 505 (2010).

[24] U. Kogelschatz, *Dielectric-Barrier Discharges: Their History, Discharge Physics, and Industrial Applications* , Plasma Chemistry and Plasma Processing **23**, 1 (2003).

[25] B. Eliasson, M. Hirth, and U. Kogelschatz, *Ozone Synthesis from Oxygen in Dielectric Barrier Discharges*, J Phys D Appl Phys **20**, 1421 (1987).

[26] F. M. Aghamir, N. S. Matin, A. H. Jalili, M. H. Esfarayeni, M. A. Khodagholi, and R. Ahmadi, *Conversion of Methane to Methanol in an Ac Dielectric Barrier Discharge*, Plasma Sources Sci Technol **13**, 707 (2004).

[27] C.-J. Liu, B. Xue, B. Eliasson, F. He, Y. Li, and G.-H. Xu, *Methane Conversion to Higher Hydrocarbons in the Presence of Carbon Dioxide Using Dielectric-Barrier Discharge Plasmas*, Plasma Chemistry and Plasma Processing **21**, 301 (2001).

[28] R. Aerts, X. Tu, W. Van Gaens, J. C. Whitehead, and A. Bogaerts, *Gas Purification by Nonthermal Plasma: A Case Study of Ethylene*, Environ Sci Technol **47**, 6478 (2013).

[29] M. Baeva, H. Gier, A. Pott, J. Uhlenbusch, J. Höschele, and J. Steinwandel, *Studies on Gas Purification by a Pulsed Microwave Discharge at 2.46 GHz in Mixtures of N2/NO/O2 at Atmospheric Pressure*, Plasma Chemistry and Plasma Processing **21**, 225 (2001).

[30] G. Borcia, C. A. Anderson, and N. M. D. Brown, *Dielectric Barrier Discharge for Surface Treatment: Application to Selected Polymers in Film and Fibre Form*, Plasma Sources Sci Technol **12**, 335 (2003).

[31] N.-Y. Cui and N. M. D. Brown, *Modification of the Surface Properties of a Polypropylene (PP) Film Using an Air Dielectric Barrier Discharge Plasma*, Appl Surf Sci **189**, 31 (2002).

[32] F. Massines, A. Rabehi, P. Decomps, R. Ben Gadri, P. Ségur, and C. Mayoux, *Experimental and Theoretical Study of a Glow Discharge at Atmospheric Pressure Controlled by Dielectric Barrier*, J Appl Phys **83**, 2950 (1998).

[33] V. Nehra and A. Kumar, Atmospheric Non-Thermal Plasma Sources, n.d.

[34] R. Foest, M. Schmidt, and K. Becker, *Microplasmas, an Emerging Field of Low-Temperature Plasma Science and Technology*, Int J Mass Spectrom **248**, 87 (2006).

[35] L. Yu, C. O. Laux, D. M. Packan, and C. H. Kruger, *Direct-Current Glow Discharges in Atmospheric Pressure Air Plasmas*, J Appl Phys **91**, 2678 (2002).

[36] K. S. Novoselov, A. K. Geim, S. V. Morozov, D. Jiang, Y. Zhang, S. V. Dubonos, I. V. Grigorieva, and A. A. Firsov, *Electric Field Effect in Atomically Thin Carbon Films*, Science (1979) **306**, 666 (2004).

[37] W. Zhu and J. L. Lopez, *A Dc Non-Thermal Atmospheric-Pressure Plasma Microjet*, Plasma Sources Sci Technol **21**, 034018 (2012).

[38] K. Tachibana, *Current Status of Microplasma Research*, IEEJ Transactions on Electrical and Electronic Engineering **1**, 145 (2006).

[39] D. Schröder, S. Burhenn, D. Kirchheim, and V. S. der Gathen, *Enhanced Oxygen Dissociation in a Propagating Constricted Discharge Formed in a Self-Pulsing Atmospheric Pressure Microplasma Jet*, J Phys D Appl Phys **46**, 464003 (2013).

[40] A. Bogaerts et al., *The 2020 Plasma Catalysis Roadmap*, J Phys D Appl Phys **53**, 443001 (2020).

[41] Y. Fan and L. Yongfeng, *Synthesis and Application of Nanocarbon Materials Using Plasma Technology*, International Journal of Chemical Engineering and Applications **6**, 49 (2015).

[42] B. R. Locke, M. Sato, P. Sunka, M. R. Hoffmann, and J.-S. Chang, *Electrohydraulic Discharge and Nonthermal Plasma for Water Treatment*, Ind Eng Chem Res **45**, 882 (2006).

[43] E. Gjika, S. Pal-Ghosh, A. Tang, M. Kirschner, G. Tadvalkar, J. Canady, M. A. Stepp, and M. Keidar, *Adaptation of Operational Parameters of Cold Atmospheric Plasma for in Vitro Treatment of Cancer Cells*, ACS Appl Mater Interfaces **10**, 9269 (2018).

[44] L. Lin and Q. Wang, *Microplasma: A New Generation of Technology for Functional Nanomaterial Synthesis*, Plasma Chemistry and Plasma Processing **35**, 925 (2015).

[45] S. Horikoshi and N. Serpone, *In-Liquid Plasma: A Novel Tool in the Fabrication of Nanomaterials and in the Treatment of Wastewaters*, RSC Adv. **7**, 47196 (2017).

[46] D. T. Elg, H. E. Delgado, D. C. Martin, R. M. Sankaran, P. Rumbach, D. M. Bartels, and D. B. Go, *Recent Advances in Understanding the Role of Solvated Electrons at the Plasma-Liquid Interface of Solution-Based Gas Discharges*, Spectrochim Acta Part B At Spectrosc **186**, 106307 (2021).

[47] R. Gopalakrishnan, E. Kawamura, A. J. Lichtenberg, M. A. Lieberman, and D. B. Graves, *Solvated Electrons at the Atmospheric Pressure Plasma–Water Anodic Interface*, J Phys D Appl Phys **49**, 295205 (2016).

[48] S. Samukawa et al., *The 2012 Plasma Roadmap*, J Phys D Appl Phys **45**, 253001 (2012).

[49] P. J. Bruggeman et al., *Plasma–Liquid Interactions: A Review and Roadmap*, Plasma Sources Sci Technol **25**, 053002 (2016).

[50] M. G. Kong, G. Kroesen, G. Morfill, T. Nosenko, T. Shimizu, J. van Dijk, and J. L. Zimmermann, *Plasma Medicine: An Introductory Review*, New J Phys **11**, 115012 (2009).

[51] A. Jain, *A Treatment of Low-Energy Positron-CO Collisions Using a New Parameter-Free Positron Correlation Polarisation (PCOP) Potential*, Journal of Physics B: Atomic, Molecular and Optical Physics **23**, 863 (1990).

[52] M. Laroussi, *Nonthermal Decontamination of Biological Media by Atmospheric-Pressure Plasmas: Review, Analysis, and Prospects*, IEEE Transactions on Plasma Science **30**, 1409 (2002).

[53] M. Laroussi, D. A. Mendis, and M. Rosenberg, *Plasma Interaction with Microbes*, New J Phys **5**, 41 (2003).

[54] S. Lerouge, M. R. Wertheimer, and L. Yahia, *Plasma Sterilization: A Review of Parameters, Mechanisms, and Limitations*, Plasmas Polym **6**, 175 (2001).

[55] R. E. J. Sladek and E. Stoffels, *Deactivation of* Escherichia Coli *by the Plasma Needle*, J Phys D Appl Phys **38**, 1716 (2005).

[56] D. B. Graves, *The Emerging Role of Reactive Oxygen and Nitrogen Species in Redox Biology and Some Implications for Plasma Applications to Medicine and Biology*, J Phys D Appl Phys **45**, 263001 (2012).

[57] R. Foest, E. Kindel, A. Ohl, M. Stieber, and K.-D. Weltmann, *Non-Thermal Atmospheric Pressure Discharges for Surface Modification*, Plasma Phys Control Fusion **47**, B525 (2005).

[58] T. Shimizu et al., *Characterization of Microwave Plasma Torch for Decontamination*, Plasma Processes and Polymers **5**, 577 (2008).

[59] J. L. Walsh and M. G. Kong, *Contrasting Characteristics of Linear-Field and Cross-Field Atmospheric Plasma Jets*, Appl Phys Lett **93**, 111501 (2008).

[60] K.-D. Weltmann, R. Brandenburg, T. von Woedtke, J. Ehlbeck, R. Foest, M. Stieber, and E. Kindel, *Antimicrobial Treatment of Heat Sensitive Products by Miniaturized Atmospheric Pressure Plasma Jets (APPJs)*, J Phys D Appl Phys **41**, 194008 (2008).

[61] I. E. Kieft, E. P. v d Laan, and E. Stoffels, *Electrical and Optical Characterization of the Plasma Needle*, New J Phys **6**, 149 (2004).

[62] G. Farin and K. E. Grund, *Technology of Argon Plasma Coagulation with Particular Regard to Endoscopic Applications.*, Endosc Surg Allied Technol **2**, 71 (1994).

[63] P. H. Gleick, *Water in Crisis: Paths to Sustainable Water Use*, Ecological Applications **8**, 571 (1998).

[64] B. Tansel, *New Technologies for Water and Wastewater Treatment: A Survey of Recent Patents*, Recent Patents on Chemical Engineeringe **1**, 17 (2008).

[65] B. R. Locke, M. Sato, P. Sunka, M. R. Hoffmann, and J.-S. Chang, *Electrohydraulic Discharge and Nonthermal Plasma for Water Treatment*, Ind Eng Chem Res **45**, 882 (2006).

[66] B. R. Locke and K.-Y. Shih, *Review of the Methods to Form Hydrogen Peroxide in Electrical Discharge Plasma with Liquid Water*, Plasma Sources Sci Technol **20**, 034006 (2011).

[67] A. A. Joshi, B. R. Locke, P. Arce, and W. C. Finney, *Formation of Hydroxyl Radicals, Hydrogen Peroxide and Aqueous Electrons by Pulsed Streamer Corona Discharge in Aqueous Solution*, J Hazard Mater **41**, 3 (1995).

[68] J. W. Erisman, M. A. Sutton, J. Galloway, Z. Klimont, and W. Winiwarter, *How a Century of Ammonia Synthesis Changed the World*, Nat Geosci **1**, 636 (2008).

[69] T. Sakakura, N. Murakami, Y. Takatsuji, and T. Haruyama, *Nitrogen Fixation in a Plasma/Liquid Interfacial Reaction and Its Switching between Reduction and Oxidation*, The Journal of Physical Chemistry C **124**, 9401 (2020).

[70] S. Li, J. Medrano Jimenez, V. Hessel, and F. Gallucci, *Recent Progress of Plasma-Assisted Nitrogen Fixation Research: A Review*, Processes **6**, 248 (2018).

[71] T. Haruyama, T. Namise, N. Shimoshimizu, S. Uemura, Y. Takatsuji, M. Hino, R. Yamasaki, T. Kamachi, and M. Kohno, *Non-Catalyzed One-Step Synthesis of Ammonia from Atmospheric Air and Water*, Green Chemistry **18**, 4536 (2016).

[72] J. van Dijk, G. M. W. Kroesen, and A. Bogaerts, *Plasma Modelling and Numerical Simulation*, J Phys D Appl Phys **42**, 190301 (2009).

[73] J. van Dijk, K. Peerenboom, M. Jimenez, D. Mihailova, and J. van der Mullen, *The Plasma Modelling Toolkit Plasimo*, J Phys D Appl Phys **42**, 194012 (2009).

[74] D. Bessières, J. Paillol, A. Bourdon, P. Ségur, and E. Marode, *A New One-Dimensional Moving Mesh Method Applied to the Simulation of Streamer Discharges*, J Phys D Appl Phys **40**, 6559 (2007).

[75] R. Peyrous, *The Effect of Relative Humidity on Ozone Production by Corona Discharge in Oxygen or Air – A Numerical Simulation – Part I : Oxygen*, Ozone Sci Eng **12**, 19 (1990).

[76] Y. Sakiyama and D. B. Graves, *Corona-Glow Transition in the Atmospheric Pressure RF-Excited Plasma Needle*, J Phys D Appl Phys **39**, 3644 (2006).

[77] Y. Sakiyama and D. B. Graves, *Efficient Modeling of Atmospheric Pressure Surface Micro-Discharge Plasma Chemistry*, Plasma Sources Sci Technol **22**, 012003 (2013).

[78] W. Van Gaens and A. Bogaerts, *Kinetic Modelling for an Atmospheric Pressure Argon Plasma Jet in Humid Air*, J Phys D Appl Phys **46**, 275201 (2013).

[79] S. A. Norberg, E. Johnsen, and M. J. Kushner, *Formation of Reactive Oxygen and Nitrogen Species by Repetitive Negatively Pulsed Helium Atmospheric Pressure Plasma Jets Propagating into Humid Air*, Plasma Sources Sci Technol **24**, 035026 (2015).

[80] N. Y. Babaeva and M. J. Kushner, *Ion Energy and Angular Distributions into the Wafer–Focus Ring Gap in Capacitively Coupled Discharges*, J Phys D Appl Phys **41**, 062004 (2008).

[81] S. A. Norberg, W. Tian, E. Johnsen, and M. J. Kushner, *Atmospheric Pressure Plasma Jets Interacting with Liquid Covered Tissue: Touching and Not-Touching the Liquid*, J Phys D Appl Phys **47**, 475203 (2014).

[82] B. R. Locke and S. M. Thagard, *Analysis and Review of Chemical Reactions and Transport Processes in Pulsed Electrical Discharge Plasma Formed Directly in Liquid Water*, Plasma Chemistry and Plasma Processing **32**, 875 (2012).

[83] V. Korol, P. Husen, E. Sjulstok, C. Nielsen, I. Friis, A. Frederiksen, A. B. Salo, and I. A. Solov'Yov, *Introducing VIKING: A Novel Online Platform for Multiscale Modeling*, ACS Omega **5**, 1254 (2020).

[84] W. E. Van Gunsteren and H. J. C. Berendsen, Computer Simulation of Molecular Dynamics: Methodology, Applications, and Perspectives in Chemistry, n.d.

[85] M. F. Horstemeyer, *Multiscale Modeling: A Review*, in *Practical Aspects of Computational Chemistry: Methods, Concepts and Applications*, edited by M. K. Leszczynski Jerzy and Shukla (Springer Netherlands, Dordrecht, 2010), pp. 87–135.

[86] B. J. Alder and T. E. Wainwright, *Studies in Molecular Dynamics. I. General Method*, J Chem Phys **31**, 459 (1959).

[87] B. J. Alder and T. E. Wainwright, *Phase Transition for a Hard Sphere System*, The Journal of Chemical Physics.

[88] J. B. Gibson, A. N. Golandp M Milgram, G. H. VINEYARD Brookha, en XaHonal Laboratory, and X. York, DIFFUSION OF F CENTER INTO KC1 SINGLE CRYSTALS Dynamics of Radiation Damage*, 1960.

[89] A. Rahman, Correlations in the Motion of Atoms in Liquid Argon, n.d.

[90] F. H. Stillinger and A. Rahman, *Improved Simulation of Liquid Water by Molecular Dynamics*, J Chem Phys **60**, 1528 (1974).

[91] P. Vashishta and A. Rahman, Ionic Motion in A-AgI, 1978.

[92] R. L. Harrison, *Introduction to Monte Carlo Simulation*, in *AIP Conference Proceedings*, Vol. 1204 (2009), pp. 17–21.

[93] R. O. Dror, R. M. Dirks, J. P. Grossman, H. Xu, and D. E. Shaw, *Biomolecular Simulation: A Computational Microscope for Molecular Biology*, Annual Review of Biophysics.

[94] M. Karplus and G. A. Petsko, Molecular Dynamics Simulations in Biology, 1990.

[95] D. Frenkel and B. Smit, *Understanding Molecular Simulation from Algorithms to Applications*, Academic Press (2002).

[96] L. Verlet, Computer “Experiments” on Classical Fluids. II. Equilibrium Correlation Functions, 1968.

[97] H. J. C. Berendsen, J. P. M. Postma, W. F. Van Gunsteren, A. Dinola, and J. R. Haak, *Molecular Dynamics with Coupling to an External Bath*, J Chem Phys **81**, 3684 (1984).

[98] J. D. Durrant and J. A. McCammon, *Molecular Dynamics Simulations and Drug Discovery*, BMC Biol **9**, 71 (2011).

[99] G. Hong, A. J. Cornish, E. L. Hegg, and R. Pachter, *On Understanding Proton Transfer to the Biocatalytic [Fe—Fe]H Sub-Cluster in [Fe—Fe]H2ases: QM/MM MD Simulations*, Biochimica et Biophysica Acta (BBA) - Bioenergetics **1807**, 510 (2011).

[100] O. Borodin, *Polarizable Force Field Development and Molecular Dynamics Simulations of Ionic Liquids*, J Phys Chem B **113**, 11463 (2009).

[101] F. J. Luque, F. Dehez, C. Chipot, and M. Orozco, *Polarization Effects in Molecular Interactions*, WIREs Computational Molecular Science **1**, 844 (2011).

[102] T. A. Halgren and W. Damm, *Polarizable Force Fields*, Curr Opin Struct Biol **11**, 236 (2001).

[103] R. Day, B. J. Bennion, S. Ham, and V. Daggett, *Increasing Temperature Accelerates Protein Unfolding Without Changing the Pathway of Unfolding*, J Mol Biol **322**, 189 (2002).

[104] D. E. Shaw et al., *Anton, a Special-Purpose Machine for Molecular Dynamics Simulation*, Commun ACM **51**, 91 (2008).

[105] A. Gunaratne, A Penalty Function Method for Constrained Molecular Dynamics, Iowa State University, 2006.

[106] C. Richmonds, M. Witzke, B. Bartling, S. W. Lee, J. Wainright, C.-C. Liu, and R. M. Sankaran, *Electron-Transfer Reactions at the Plasma–Liquid Interface*, J Am Chem Soc **133**, 17582 (2011).

[107] P. Rumbach, N. Griggs, R. M. Sankaran, and D. B. Go, *Visualization of Electrolytic Reactions at a Plasma-Liquid Interface*, IEEE Transactions on Plasma Science **42**, 2610 (2014).

[108] A. J. Bard and L. R. Faulkner, *Electrochemical Methods: Fundamentals and Applications*, 2nd ed. (John Wiley and Sons, Inc, New York, 2001).

[109] C. Liu and A. J. Bard, *Electrostatic Electrochemistry at Insulators*, Nat Mater **7**, 505 (2008).

[110] D. J. Lacks and R. Mohan Sankaran, *Contact Electrification of Insulating Materials*, J Phys D Appl Phys **44**, 453001 (2011).

[111] S.-E. Yoon, J.-Y. Ahn, B.-K. Kim, and J.-S. Park, *Improvements in Co-Electrolysis Performance and Long-Term Stability of Solid Oxide Electrolysis Cells Based on Ceramic Composite Cathodes*, Int J Hydrogen Energy **40**, 13558 (2015).

[112] J. Gubkin, *Electrolytische Metallabscheidung an Der Freien Oberfläche Einer Salzlösung*, Annalen Der Physik Und Chemie **268**, 114 (1887).

[113] K. HARADA and S. SUZUKI, *Formation of Amino Acids from Elemental Carbon by Contact Glow Discharge Electrolysis*, Nature **266**, 275 (1977).

[114] K. HARADA and T. IWASAKI, *Syntheses of Amino Acids from Aliphatic Carboxylic Acid by Glow Discharge Electrolysis*, Nature **250**, 426 (1974).

[115] K. Baba, T. Kaneko, and R. Hatakeyama, *Ion Irradiation Effects on Ionic Liquids Interfaced with Rf Discharge Plasmas*, Appl Phys Lett **90**, 201501 (2007).

[116] A. Hickling and M. D. Ingram, *Glow-Discharge Electrolysis*, Journal of Electroanalytical Chemistry (1959) **8**, 65 (1964).

[117] A. R. Denaro and A. Hickling, *Glow-Discharge Electrolysis in Aqueous Solutions*, J Electrochem Soc **105**, 265 (1958).

[118] T. A. Kareem and A. A. Kaliani, *Glow Discharge Plasma Electrolysis for Nanoparticles Synthesis*, Ionics (Kiel) **18**, 315 (2012).

[119] F. Rezaei, P. Vanraes, A. Nikiforov, R. Morent, and N. De Geyter, *Applications of Plasma-Liquid Systems: A Review*, Materials **12**, 2751 (2019).

[120] N. De Geyter and R. Morent, *Nonthermal Plasma Sterilization of Living and Nonliving Surfaces*, Annu Rev Biomed Eng **14**, 255 (2012).

[121] F. Rezaei, A. Nikiforov, R. Morent, and N. De Geyter, *Plasma Modification of Poly Lactic Acid Solutions to Generate High Quality Electrospun PLA Nanofibers*, Sci Rep **8**, 2241 (2018).

[122] T. Habib, B. Caillier, and J. M. A. Caiut, *Plasma-Assisted Synthesis of Silver Nanoparticles*, in *2021 IEEE International Conference on Plasma Science (ICOPS)* (IEEE, 2021), pp. 1–1.

[123] N. Shirai and K. Sasaki, *Synthesis of Metal Nanoparticles Induced by Plasma-Assisted Electrolysis*, in *High-Energy Chemistry and Processing in Liquids* (Springer Nature Singapore, Singapore, 2022), pp. 57–72.

[124] N. Kaushik, N. Kaushik, N. Linh, B. Ghimire, A. Pengkit, J. Sornsakdanuphap, S.-J. Lee, and E. Choi, *Plasma and Nanomaterials: Fabrication and Biomedical Applications*, Nanomaterials **9**, 98 (2019).

[125] N. Boonyeun, R. Rujiravanit, and N. Saito, *Plasma-Assisted Synthesis of Multicomponent Nanoparticles Containing Carbon, Tungsten Carbide and Silver as Multifunctional Filler for Polylactic Acid Composite Films*, Polymers (Basel) **13**, 991 (2021).

[126] C. Richmonds and R. M. Sankaran, *Plasma-Liquid Electrochemistry: Rapid Synthesis of Colloidal Metal Nanoparticles by Microplasma Reduction of Aqueous Cations*, Appl Phys Lett **93**, 131501 (2008).

[127] N. Sano, H. Wang, M. Chhowalla, I. Alexandrou, and G. A. J. Amaratunga, *Synthesis of Carbon "onions" in Water*, Nature **414**, 506 (2001).

[128] S. A. Meiss, M. Rohnke, L. Kienle, S. Zein El Abedin, F. Endres, and J. Janek, *Employing Plasmas as Gaseous Electrodes at the Free Surface of Ionic Liquids: Deposition of Nanocrystalline Silver Particles*, ChemPhysChem **8**, 50 (2007).

[129] D. Higgins, C. Hahn, C. Xiang, T. F. Jaramillo, and A. Z. Weber, *Gas-Diffusion Electrodes for Carbon Dioxide Reduction: A New Paradigm*, ACS Energy Lett **4**, 317 (2019).

[130] A. C. Krueger and L. Kahlenberg, *Gas Electrodes*, Transactions of the American Electrochemical Society **58**, 107 (1930).

[131] R. Seeber, C. Zanardi, and G. Inzelt, *The Inherent Coupling of Charge Transfer and Mass Transport Processes: The Curious Electrochemical Reversibility*, ChemTexts **2**, 8 (2016).

[132] J. O. Bockris and H. Kita, *The Dependence of Charge Transfer and Surface Diffusion Rates on the Structure and Stability of an Electrode Surface: Copper*, J Electrochem Soc **109**, 928 (1962).

[133] A. Klemenc and H. F. Hohn, *Über Die Vorgänge in Der Lösung Und Im Gasraum Bei Der Glimmlichtelektrolyse*, Zeitschrift Für Physikalische Chemie **154A**, 385 (1931).

[134] D. Mariotti and R. M. Sankaran, *Perspectives on Atmospheric-Pressure Plasmas for Nanofabrication*, J Phys D Appl Phys **44**, 174023 (2011).

[135] K. H. Becker, K. H. Schoenbach, and J. G. Eden, *Microplasmas and Applications*, J Phys D Appl Phys **39**, R55 (2006).

[136] K. H. Schoenbach and K. Becker, *20 Years of Microplasma Research: A Status Report*, The European Physical Journal D **70**, 29 (2016).

[137] C. Bergamini, S. Gambetti, A. Dondi, and C. Cervellati, *Oxygen, Reactive Oxygen Species and Tissue Damage*, Curr Pharm Des **10**, 1611 (2004).

[138] H. Bayr, *Reactive Oxygen Species*, Crit Care Med **33**, S498 (2005).

[139] D. B. Graves, *The Emerging Role of Reactive Oxygen and Nitrogen Species in Redox Biology and Some Implications for Plasma Applications to Medicine and Biology*, J Phys D Appl Phys **45**, 263001 (2012).

[140] C. G. Avio, S. Gorbi, and F. Regoli, *Plastics and Microplastics in the Oceans: From Emerging Pollutants to Emerged Threat*, Mar Environ Res **128**, 2 (2017).

[141] T. Ogawa, N. Yonekura, M. Tsukada, S. Ihara, T. Yasuda, H. Tomura, K. Nakashima, and H. Kawazumi, *Electron-Impact Dissociation of Water as Studied by the Angular Difference Doppler Profiles of the Excited Hydrogen Atom*, J Phys Chem **95**, 2788 (1991).

[142] P. C. Cosby, *Electron-impact Dissociation of Oxygen*, J Chem Phys **98**, 9560 (1993).

[143] F. L. ARNOT, *Molecular Dissociation by Electron Impact*, Nature **129**, 617 (1932).

[144] Walker. Bleakney, E. U. Condon, and L. G. Smith, *Ionization and Dissociation of Molecules by Electron Impact*, J Phys Chem **41**, 197 (1937).

[145] M. A. Malik and K. H. Schoenbach, *New Approach for Sustaining Energetic, Efficient and Scalable Non-Equilibrium Plasma in Water Vapours at Atmospheric Pressure*, J Phys D Appl Phys **45**, 132001 (2012).

[146] M. Cole, P. Lindeque, C. Halsband, and T. S. Galloway, *Microplastics as Contaminants in the Marine Environment: A Review*, Mar Pollut Bull **62**, 2588 (2011).

[147] N. P. Ivleva, A. C. Wiesheu, and R. Niessner, *Microplastic in Aquatic Ecosystems*, Angewandte Chemie International Edition **56**, 1720 (2017).

[148] G. Peng, P. Xu, B. Zhu, M. Bai, and D. Li, *Microplastics in Freshwater River Sediments in Shanghai, China: A Case Study of Risk Assessment in Mega-Cities*, Environmental Pollution **234**, 448 (2018).

[149] G. Erni-Cassola, M. I. Gibson, R. C. Thompson, and J. A. Christie-Oleza, *Lost, but Found with Nile Red: A Novel Method for Detecting and Quantifying Small Microplastics (1 Mm to 20 Mm) in Environmental Samples*, Environ Sci Technol **51**, 13641 (2017).

[150] R. Ahmed, A. K. Hamid, S. A. Krebsbach, J. He, and D. Wang, *Critical Review of Microplastics Removal from the Environment*, Chemosphere **293**, 133557 (2022).

[151] Y. Zhang, G. Zhou, J. Yue, X. Xing, Z. Yang, X. Wang, Q. Wang, and J. Zhang, *Enhanced Removal of Polyethylene Terephthalate Microplastics through Polyaluminum Chloride Coagulation with Three Typical Coagulant Aids*, Science of The Total Environment **800**, 149589 (2021).

[152] Z. Li, C. Feng, Y. Wu, and X. Guo, *Impacts of Nanoplastics on Bivalve: Fluorescence Tracing of Organ Accumulation, Oxidative Stress and Damage*, J Hazard Mater **392**, 122418 (2020).

[153] S. Sharma and S. Chatterjee, *Microplastic Pollution, a Threat to Marine Ecosystem and Human Health: A Short Review*, Environmental Science and Pollution Research **24**, 21530 (2017).

[154] M. Cole, P. Lindeque, E. Fileman, C. Halsband, and T. S. Galloway, *The Impact of Polystyrene Microplastics on Feeding, Function and Fecundity in the Marine Copepod* Calanus Helgolandicus, Environ Sci Technol **49**, 1130 (2015).

[155] M. Cole, P. K. Lindeque, E. Fileman, J. Clark, C. Lewis, C. Halsband, and T. S. Galloway, *Microplastics Alter the Properties and Sinking Rates of Zooplankton Faecal Pellets*, Environ Sci Technol **50**, 3239 (2016).

[156] P. Schwabl, S. Köppel, P. Königshofer, T. Bucsics, M. Trauner, T. Reiberger, and B. Liebmann, *Detection of Various Microplastics in Human Stool*, Ann Intern Med **171**, 453 (2019).

[157] P. Schwabl, S. Köppel, P. Königshofer, T. Bucsics, M. Trauner, T. Reiberger, and B. Liebmann, *Detection of Various Microplastics in Human Stool*, Ann Intern Med **171**, 453 (2019).

[158] L. Wang, A. Kaeppler, D. Fischer, and J. Simmchen, *Photocatalytic TiO_2 Micromotors for Removal of Microplastics and Suspended Matter*, ACS Appl Mater Interfaces **11**, 32937 (2019).

[159] H. S. Auta, C. U. Emenike, and S. H. Fauziah, *Distribution and Importance of Microplastics in the Marine Environment: A Review of the Sources, Fate, Effects, and Potential Solutions*, Environ Int **102**, 165 (2017).

[160] M. Shen, T. Hu, W. Huang, B. Song, G. Zeng, and Y. Zhang, *Removal of Microplastics from Wastewater with Aluminosilicate Filter Media and Their Surfactant-Modified Products: Performance, Mechanism and Utilization*, Chemical Engineering Journal **421**, 129918 (2021).

[161] J. R. Jambeck, R. Geyer, C. Wilcox, T. R. Siegler, M. Perryman, A. Andrady, R. Narayan, and K. L. Law, *Plastic Waste Inputs from Land into the Ocean*, Science (1979) **347**, 768 (2015).

[162] R. Geyer, J. R. Jambeck, and K. L. Law, *Production, Use, and Fate of All Plastics Ever Made*, Sci Adv **3**, (2017).

[163] C. Zarfl and M. Matthies, *Are Marine Plastic Particles Transport Vectors for Organic Pollutants to the Arctic?*, Mar Pollut Bull **60**, 1810 (2010).

[164] A. Wegner, E. Besseling, E. M. Foekema, P. Kamermans, and A. A. Koelmans, *Effects of Nanopolystyrene on the Feeding Behavior of the Blue Mussel (* Mytilus Edulis *L.)*, Environ Toxicol Chem **31**, 2490 (2012).

[165] V. Hidalgo-Ruz, L. Gutow, R. C. Thompson, and M. Thiel, *Microplastics in the Marine Environment: A Review of the Methods Used for Identification and Quantification*, Environ Sci Technol **46**, 3060 (2012).

[166] C. J. Moore, *Synthetic Polymers in the Marine Environment: A Rapidly Increasing, Long-Term Threat*, Environ Res **108**, 131 (2008).

[167] K.-W. Lee, W. J. Shim, O. Y. Kwon, and J.-H. Kang, *Size-Dependent Effects of Micro Polystyrene Particles in the Marine Copepod* Tigriopus Japonicus, Environ Sci Technol **47**, 11278 (2013).

[168] G. Rossi, J. Barnoud, and L. Monticelli, *Polystyrene Nanoparticles Perturb Lipid Membranes*, J Phys Chem Lett **5**, 241 (2014).

[169] E. Besseling, B. Wang, M. Lürling, and A. A. Koelmans, *Nanoplastic Affects Growth of* S. Obliquus *and Reproduction of* D. Magna, Environ Sci Technol **48**, 12336 (2014).

[170] M. Amjad, A. Intisar, A. Afzal, and N. Hussain, *Biological Methods for the Removal of Microplastics from Water*, in (2023), pp. 65–78.

[171] K. H. D. Tang and T. Hadibarata, *The Application of Bioremediation in Wastewater Treatment Plants for Microplastics Removal: A Practical Perspective*, Bioprocess Biosyst Eng **45**, 1865 (2022).

[172] A. Mohammad R and A.-A. Qusay, *Eco-Friendly Microplastic Removal through Physical and Chemical Techniques: A Review*, Annals of Advances in Chemistry **7**, (2023).

[173] S. Kim, A. Sin, H. Nam, Y. Park, H. Lee, and C. Han, *Advanced Oxidation Processes for Microplastics Degradation: A Recent Trend*, Chemical Engineering Journal Advances **9**, 100213 (2022).

[174] M. Priyanka and M. P. Saravanakumar, *A Sustainable Approach for Removal of Microplastics from Water Matrix Using Colloidal Gas Aphrons: New Insights on Flotation Potential and Interfacial Mechanism*, J Clean Prod **334**, 130198 (2022).

[175] C. Akarsu, H. Kumbur, and A. E. Kideys, *Removal of Microplastics from Wastewater through Electrocoagulation-Electroflotation and Membrane Filtration Processes*, Water Science and Technology **84**, 1648 (2021).

[176] H. Wu, R. Liu, Y. Sun, Y. Wen, Q. Zhao, S. Lin, and Y. Wang, *Effect of MoS2 on Phenol Decomposition in Water after High-Voltage Pulse Discharge Treatment*, Chemosphere **294**, 133808 (2022).

[177] N. Jiang, X. Kong, X. Lu, B. Peng, Z. Liu, J. Li, K. Shang, N. Lu, and Y. Wu, *Promoting Streamer Propagation, Active Species Generation and Trichloroethylene Degradation*

Using a Three-Electrode Nanosecond Pulsed Sliding DBD Nanosecond Plasma, J Clean Prod **332**, 129998 (2022).

[178] M. Hatzisymeon, D. Tataraki, C. Tsakiroglou, G. Rassias, and C. A. Aggelopoulos, *Highly Energy-Efficient Degradation of Antibiotics in Soil: Extensive Cold Plasma Discharges Generation in Soil Pores Driven by High Voltage Nanopulses*, Science of The Total Environment **786**, 147420 (2021).

[179] K. Shang, R. Morent, N. Wang, Y. Wang, B. Peng, N. Jiang, N. Lu, and J. Li, *Degradation of Sulfamethoxazole (SMX) by Water Falling Film DBD Plasma/Persulfate: Reactive Species Identification and Their Role in SMX Degradation*, Chemical Engineering Journal **431**, 133916 (2022).

[180] T. Wang, Y. Cao, G. Qu, Q. Sun, T. Xia, X. Guo, H. Jia, and L. Zhu, *Novel Cu(II)–EDTA Decomplexation by Discharge Plasma Oxidation and Coupled Cu Removal by Alkaline Precipitation: Underneath Mechanisms*, Environ Sci Technol **52**, 7884 (2018).

[181] Q. Guo, Y. Wang, H. Zhang, G. Qu, T. Wang, Q. Sun, and D. Liang, *Alleviation of Adverse Effects of Drought Stress on Wheat Seed Germination Using Atmospheric Dielectric Barrier Discharge Plasma Treatment*, Sci Rep **7**, 16680 (2017).

[182] A. J. Yáñez-Pacios and J. M. Martín-Martínez, *Surface Modification and Improved Adhesion of Wood-Plastic Composites (WPCs) Made with Different Polymers by Treatment with Atmospheric Pressure Rotating Plasma Jet*, Int J Adhes Adhes **77**, 204 (2017).

[183] O. Galmiz, D. Pavliňák, M. Zemánek, A. Brablec, and M. Černák, *Hydrophilization of Outer and Inner Surfaces of Poly(Vinyl Chloride) Tubes Using Surface Dielectric Barrier Discharges Generated in Ambient Air Plasma*, Plasma Processes and Polymers **14**, 1600220 (2017).

[184] N. Jiang, X. Li, H. Guo, J. Li, K. Shang, N. Lu, and Y. Wu, *Plasma-Assisted Catalysis Decomposition of BPA over Graphene-CdS Nanocomposites in Pulsed Gas-Liquid Hybrid Discharge: Photocorrosion Inhibition and Synergistic Mechanism Analysis*, Chemical Engineering Journal **412**, 128627 (2021).

[185] Z. Gao, J. Zhou, M. Xue, S. Liu, J. Guo, Y. Zhang, C. Cao, T. Wang, and L. Zhu, *Theoretical and Experimental Insights into the Mechanisms of C6/C6 PFPiA Degradation by Dielectric Barrier Discharge Plasma*, J Hazard Mater **424**, 127522 (2022).

[186] J. Ren, J. Li, Y. Zhen, J. Wang, and Z. Niu, *Removal of Polyvinyl Chloride Microplastic by Dielectric Barrier Discharge Plasma*, Sep Purif Technol **290**, 120832 (2022).

[187] L. Zhou, T. Wang, G. Qu, H. Jia, and L. Zhu, *Probing the Aging Processes and Mechanisms of Microplastic under Simulated Multiple Actions Generated by Discharge Plasma*, J Hazard Mater **398**, 122956 (2020).

[188] F. Miao, Y. Liu, M. Gao, X. Yu, P. Xiao, M. Wang, S. Wang, and X. Wang, *Degradation of Polyvinyl Chloride Microplastics via an Electro-Fenton-like System with a TiO2/Graphite Cathode*, J Hazard Mater **399**, 123023 (2020).

[189] J. Ren, J. Li, Y. Zhen, J. Wang, and Z. Niu, *Removal of Polyvinyl Chloride Microplastic by Dielectric Barrier Discharge Plasma*, Sep Purif Technol **290**, 120832 (2022).

[190] M. E. Miller, F. J. Kroon, and C. A. Motti, *Recovering Microplastics from Marine Samples: A Review of Current Practices*, Mar Pollut Bull **123**, 6 (2017).

[191] J. Brandon, M. Goldstein, and M. D. Ohman, *Long-Term Aging and Degradation of Microplastic Particles: Comparing in Situ Oceanic and Experimental Weathering Patterns*, Mar Pollut Bull **110**, 299 (2016).

[192] H. He, M. Zhong, B. Adzima, D. Luebke, H. Nulwala, and K. Matyjaszewski, *A Simple and Universal Gel Permeation Chromatography Technique for Precise Molecular Weight Characterization of Well-Defined Poly(Ionic Liquid)s*, J Am Chem Soc **135**, 4227 (2013).

[193] A. M. Gulizia, E. Brodie, R. Daumuller, S. B. Bloom, T. Corbett, M. M. F. Santana, C. A. Motti, and G. Vamvounis, *Evaluating the Effect of Chemical Digestion Treatments on Polystyrene Microplastics: Recommended Updates to Chemical Digestion Protocols*, Macromol Chem Phys **223**, 2100485 (2022).

[194] A. Dutta, *Fourier Transform Infrared Spectroscopy*, in *Spectroscopic Methods for Nanomaterials Characterization* (Elsevier, 2017), pp. 73–93.

[195] S. Veerasingam et al., *Contributions of Fourier Transform Infrared Spectroscopy in Microplastic Pollution Research: A Review*, Crit Rev Environ Sci Technol **51**, 2681 (2021).

[196] M. Rogošić, H. J. Mencer, and Z. Gomzi, *Polydispersity Index and Molecular Weight Distributions of Polymers*, Eur Polym J **32**, 1337 (1996).

[197] M. Claessens, L. Van Cauwenberghe, M. B. Vandegehuchte, and C. R. Janssen, *New Techniques for the Detection of Microplastics in Sediments and Field Collected Organisms*, Mar Pollut Bull **70**, 227 (2013).

[198] A. Dehaut et al., *Microplastics in Seafood: Benchmark Protocol for Their Extraction and Characterization*, Environmental Pollution **215**, 223 (2016).

[199] A. I. Catarino, R. Thompson, W. Sanderson, and T. B. Henry, *Development and Optimization of a Standard Method for Extraction of Microplastics in Mussels by Enzyme Digestion of Soft Tissues*, Environ Toxicol Chem **36**, 947 (2017).

[200] E. Jabbari and N. A. Peppas, *Use of ATR-FTIR to Study Interdiffusion in Polystyrene and Poly(Vinyl Methyl Ether)*, Macromolecules **26**, 2175 (1993).

[201] M. Kiendrebeogo, M. R. Karimi Estahbanati, A. Khosravanipour Mostafazadeh, P. Drogui, and R. D. Tyagi, *Treatment of Microplastics in Water by Anodic Oxidation: A Case Study for Polystyrene*, Environmental Pollution **269**, 116168 (2021).

[202] J. Wang and X. Li, *Electrochemical Treatment of Wastewater Containing Chlorophenols Using Boron-Doped Diamond Film Electrodes*, J Cent South Univ **19**, 1946 (2012).

[203] M. Panizza, P. A. Michaud, G. Cerisola, and Ch. Comninellis, *Anodic Oxidation of 2-Naphthol at Boron-Doped Diamond Electrodes*, Journal of Electroanalytical Chemistry **507**, 206 (2001).

[204] L. Cai, J. Wang, J. Peng, Z. Wu, and X. Tan, *Observation of the Degradation of Three Types of Plastic Pellets Exposed to UV Irradiation in Three Different Environments*, Science of The Total Environment **628–629**, 740 (2018).

[205] M. Abraham, *GROMACS 2023.2 Manual*, 2023.2.

[206] J.-P. Hansen and I. R. McDonald, *Theory of Simple Liquids* (Academic Press, 1967).

[207] J. Lekner, *Motion of Electrons in Liquid Argon*, Physical Review **158**, 130 (1967).

[208] Y. Sakai, W. F. Schmidt, and A. Khrapak, *High- and Low-Mobility Electrons in Liquid Neon*, Chem Phys **164**, 139 (1992).

[209] Y. Sakai, S. Nakamura, and H. Tagashira, *Drift Velocity of Hot Electrons in Liquid Ar, Kr, and Xe*, IEEE Transactions on Electrical Insulation **EI-20**, 133 (1985).

[210] A. F. Borghesani, *Electron and Ion Transport in Dense Rare Gases*, IEEE Transactions on Dielectrics and Electrical Insulation **13**, 492 (2006).

[211] V. M. Atrazhev and I. V. Timoshkin, *Electron Scattering by a Cut-off Atomic Potential: Application to Electron Properties in Atomic Liquids*, Phys Rev B **54**, 11252 (1996).

[212] V. M. Atrazhev and I. V. Timoshkin, *Transport of Electrons in Atomic Liquids in High Electric Fields*, IEEE Transactions on Dielectrics and Electrical Insulation **5**, 450 (1998).

[213] N. A. Garland, D. G. Cocks, G. J. Boyle, S. Dujko, and R. D. White, *Unified Fluid Model Analysis and Benchmark Study for Electron Transport in Gas and Liquid Analogs*, Plasma Sources Sci Technol **26**, 075003 (2017).

[214] N. A. Garland, G. J. Boyle, D. G. Cocks, and R. D. White, *Approximating the Nonlinear Density Dependence of Electron Transport Coefficients and Scattering Rates across the Gas–Liquid Interface*, Plasma Sources Sci Technol **27**, 024002 (2018).

[215] A. F. Borghesani, D. Iannuzzi, and G. Carugno, *Excess Electron Mobility in Liquid Ar - Kr and Ar - Xe Mixtures*, Journal of Physics: Condensed Matter **9**, 5057 (1997).

[216] G. J. Boyle, R. P. McEachran, D. G. Cocks, and R. D. White, *Electron Scattering and Transport in Liquid Argon*, J Chem Phys **142**, (2015).

[217] M. H. Cohen and J. Lekner, *Theory of Hot Electrons in Gases, Liquids, and Solids*, Physical Review **158**, 305 (1967).

[218] R. E. Robson, R. D. White, and M. Hilderbrandt, *Fundamentals of Charged Particle Transport in Gases and Condensed Matter* (Taylor and Francis Group, 2017).

[219] B. B. Hamel, *Kinetic Model for Binary Gas Mixtures*, Phys Fluids **8**, 418 (1965).

[220] J. L. Yarnell, M. J. Katz, R. G. Wenzel, and S. H. Koenig, *Structure Factor and Radial Distribution Function for Liquid Argon at 85 °K*, Phys Rev A (Coll Park) **7**, 2130 (1973).

[221] A. Rotenberg, *Monte Carlo Equation of State for a Mixture of Hard Spheres*, J Chem Phys **43**, 4377 (1965).

[222] J. V. L. Singer and K. Singer, *Monte Carlo Calculation of Thermodynamic Properties of Binary Mixtures of Lennard-Jones (12-6) Liquids*, Mol Phys **24**, 357 (1972).

[223] I. R. McDonald, *NpT -Ensemble Monte Carlo Calculations for Binary Liquid Mixtures*, Mol Phys **23**, 41 (1972).

[224] M. F. Pas and B. J. Zwolinski, *Computation of the Transport Coefficients of Binary Mixtures of Argon-Krypton, Krypton-Xenon, and Argon-Xenon by Molecular Dynamics*, Mol Phys **73**, 483 (1991).

[225] M. Balcells, A. Giró, and J. A. Padró, *Correlations in the Ar-Kr Liquid Mixture*, Physica A: Statistical Mechanics and Its Applications **135**, 414 (1986).

[226] L. Verlet and J.-J. Weis, *Perturbation Theory for the Thermodynamic Properties of Simple Liquids*, Mol Phys **24**, 1013 (1972).

[227] K. C. Mo, K. E. Gubbins, G. Jacucci, and I. R. McDonald, *The Radial Distribution Function in Fluid Mixtures: Conformal Solution Theory and Molecular Dynamics Results*, Mol Phys **27**, 1173 (1974).

[228] M. Moosavi and E. K. Goharshadi, *Molecular Dynamic Simulations of Some Thermodynamic Properties of Mixtures of Argon with Neon, Krypton, and Xenon Using Two-Body and Three-Body Interaction Potentials*, Fluid Phase Equilib **274**, 51 (2008).

[229] G. Jacucci and I. R. McDonald, *Structure and Diffusion in Mixtures of Rare-Gas Liquids*, Physica A: Statistical Mechanics and Its Applications **80**, 607 (1975).

[230] C. Hoheisel and U. Deiters, *High Pressure Molecular Dynamics of the Partially Miscible Fluid Mixture Neon/Krypton*, Mol Phys **37**, 95 (1979).

[231] Y. Duan et al., A Point-Charge Force Field for Molecular Mechanics Simulations of Proteins Based on Condensed-Phase Quantum Mechanical Calculations, 1999.

APPENDICES

APPENDIX A - SUPPLEMENTARY INFORMATION FOR CHAPTER 2

Table S2.1: pH measurements in the cathode compartment of the plasma electrochemistry setup operated at a constant discharge current of $3\ mA$, and the needle was positioned approximately 1 mm away from the electrolyte's surface on the cathode side.

Exposure Time (mins)	Initial pH			Final pH		
	Trial 01	Trial 02	Trial 03	Trial 01	Trial 02	Trial 03
0	0	0	0	0	0	0
2	3.03	2.87	3.00	3.20	3.15	3.28
5	3.02	2.96	3.03	3.40	3.35	3.42
10	3.03	3.00	3.00	10.45	10.50	10.35
15	3.03	3.00	2.93	10.87	10.67	10.65
30	3.03	2.89	3.02	11.17	11.30	11.25

Table S2.2: pH measurements in the cathode compartment of the plasma electrochemistry setup operated at a constant discharge current of 3 mA, and the needle was positioned approximately 3 mm away from the electrolyte's surface on the cathode side.

Exposure Time (mins)	Initial pH			Final pH		
	Trial 01	Trial 02	Trial 03	Trial 01	Trial 02	Trial 03
0	0	0	0	0	0	0
2	2.98	3.00	3.02	3.25	3.39	3.27
5	3.03	2.97	2.96	3.38	3.40	3.40
10	2.95	3.02	3.01	10.40	10.21	10.38

15	3.03	3.02	3.00	10.75	10.81	10.67
30	3.03	2.89	2.99	11.25	11.32	11.20

Table S2.3: pH measurements in the cathode compartment of the plasma electrochemistry setup operated at a constant discharge current of 3 mA, and the needle was positioned approximately 1 mm away from the electrolyte's surface on the cathode side at experimental series 2 (with 180 mL of electrolyte solution).

Exposure Time (mins)	Initial pH			Final pH		
	Trial 01	Trial 02	Trial 03	Trial 01	Trial 02	Trial 03
0	0	0	0	0	0	0
2	3.02	2.94	3.01	3.03	3.05	3.02
5	2.97	3.00	3.00	3.09	3.05	3.05
10	3.03	3.02	2.98	3.05	3.02	3.09
15	3.00	2.97	3.02	3.07	3.11	3.08
30	3.00	3.02	2.98	3.08	3.10	3.07

Table S2.4: The average final pH in the cathode compartment of the plasma electrochemistry setup maintained at a consistent discharge current of 3 mA, and the needle was positioned approximately 1 mm away from the electrolyte’s surface on the cathode side.

Exposure Time (mins)	Average pH	Standard Deviation
0	0	0
2	3.21	0.07
5	3.39	0.04
10	10.43	0.08
15	10.73	0.12
30	11.24	0.07

Table S2.5: The average final pH in the cathode compartment of the plasma electrochemistry setup maintained at a consistent discharge current of 3 mA, and the needle was positioned approximately 3 mm away from the electrolyte’s surface on the cathode side.

Exposure Time (mins)	Average pH	Standard Deviation
0	0	0
2	3.30	0.08
5	3.39	0.01
10	10.33	0.10
15	10.74	0.07
30	11.26	0.06

Table S2.6: The average final pH in the cathode compartment of the plasma electrochemistry setup operated at a constant discharge current of 3 mA, and the needle was positioned approximately 1 mm away from the electrolyte's surface on the cathode side at experimental series 02 (with 180 mL of electrolyte solution).

Exposure Time (mins)	Average pH	Standard Deviation
0	0	0
2	3.03	0.02
5	3.06	0.02
10	3.05	0.04
15	3.08	0.02
30	3.08	0.02

Table S2.7: Calculated values for the number of H^+ ions reduced and changed in H^+ ions concentration in the cathode compartment of the plasma electrochemistry setup maintained at a consistent discharge current of 3 mA, and the needle was positioned approximately 1 mm away from the electrolyte's surface on the cathode side.

Exposure Time (Min)	Initial pH	Final pH	Initial H^+ ions $(\times 10^{18})$	Final H^+ ions $(\times 10^{18})$	The number of H^+ reduced $(\times 10^{18})$	Experimental change in H^+ concentration mol/L $(\times 10^{-4})$
2	3.03	3.20	8.43	5.70	- 2.73	- 3.02
2	2.87	3.15	12.2	6.39	- 5.79	- 6.41
2	3.00	3.28	9.03	4.74	- 4.29	- 4.75
5	3.02	3.40	8.63	3.60	- 5.03	- 5.57
5	2.96	3.35	9.90	4.03	- 5.87	- 6.50
5	3.03	3.42	8.43	3.43	- 5.00	- 5.53
10	3.03	10.45	8.43	0.00000032	- 8.43	- 9.33
10	3.00	10.50	9.03	0.00000029	- 9.03	- 10.00
10	3.00	10.35	9.03	0.00000040	- 9.03	- 10.00
15	3.03	10.87	8.43	0.00000012	- 8.43	- 9.33
15	3.00	10.67	9.03	0.00000019	- 9.03	- 10.00
15	2.93	10.65	10.6	0.00000020	- 10.6	- 11.70
30	3.03	11.17	8.43	0.000000061	- 8.43	- 9.33
30	2.89	11.30	11.6	0.000000045	- 11.6	- 12.9
30	3.02	11.25	8.63	0.000000051	- 8.63	- 9.55

Table S2.8: Calculated values for the number of H^+ ions reduced and changed in H+ ions concentration in the cathode compartment of the plasma electrochemistry setup maintained at a consistent discharge current of 3 mA, and the needle was positioned approximately 3 mm away from the electrolyte's surface on the cathode side.

Exposure Time (Min)	Initial pH	Final pH	Initial H^+ ions $(\times 10^{18})$	Final H^+ ions $(\times 10^{18})$	The number of H^+ reduced $(\times 10^{18})$	Experimental change in H^+ concentration $mol/L\ (\times 10^{-4})$
2	2.99	3.15	9.24	6.40	- 2.85	- 3.15
2	3.00	3.17	9.03	6.11	- 2.93	- 3.24
2	3.02	3.18	8.63	5.97	- 2.66	- 2.94
5	3.03	3.28	8.43	4.74	- 3.69	- 4.08
5	2.97	3.30	9.68	4.53	- 5.15	- 5.70
5	2.96	3.27	9.90	4.85	- 5.05	- 5.59
10	3.03	9.98	8.43	0.00000095	- 8.43	- 9.33
10	3.02	10.25	8.63	0.00000051	- 8.63	- 9.55
10	3.01	10.30	8.83	0.00000038	- 8.83	- 9.77
15	3.03	10.75	8.43	0.00000045	- 8.43	- 9.33
15	3.02	10.81	8.63	0.00000012	- 8.63	- 9.55
15	3.00	10.67	9.03	0.00000019	- 9.03	- 10.00
30	3.03	11.00	8.43	0.000000090	- 8.43	- 9.33
30	3.00	11.22	9.03	0.000000054	- 9.03	- 10.00
30	2.99	11.20	9.24	0.000000057	- 9.24	- 10.20

Table S2.9: The average change in the concentration of H^+ ions in the cathode compartment of the plasma electrochemistry setup maintained at a consistent discharge current of 3 mA, and the needle was positioned approximately 1 mm away from the electrolyte's surface on the cathode side.

Exposure Time (Min)	The average experimental change in H^+ concentration $mol/L\ (\times 10^{-4})$	Standard deviation $mol/L\ (\times 10^{-4})$
2	- 4.73	1.70
5	- 5.87	0.55
10	- 9.78	0.39
15	- 10.34	1.22
30	- 10.59	2.00

Table S2.10: The average change in the concentration of H^+ ions in the cathode compartment of the plasma electrochemistry setup maintained at a consistent discharge current of 3 mA, and the needle was positioned approximately 3 mm away from the electrolyte's surface on the cathode side.

Exposure Time (Min)	The average experimental change in H^+ concentration $mol/L\ (\times 10^{-4})$	Standard deviation $mol/L\ (\times 10^{-4})$
2	- 3.11	0.15
5	- 5.12	0.91
10	- 9.55	0.22
15	- 9.63	0.34
30	- 9.84	0.46

Table S2.11: Calculated values for the expected change in H^+ ions concentration in the cathode compartment of the plasma electrochemistry setup maintained at a consistent discharge current of 3 mA, and the needle was positioned approximately 1 mm and 3 mm away from the electrolyte's surface on the cathode side, assuming 100% conversion of the discharge current and considering only the hydrogen evolution reaction occurring in the catholyte.

Exposure Time (Min)	Expected change in H^+ concentration $mol/L\ (\times 10^{-4})$
2	-2.49
5	-6.22
10	-12.44
15	-18.66
30	-37.32

Table S2.12: The average change in the concentration of H^+ ions in the cathode compartment of the plasma electrochemistry setup maintained at a consistent discharge current of 2 mA at previous research work done by Witzke et al., [1].

Exposure Time (Min)	The average experimental change in H^+ concentration $mol/L\ (\times 10^{-4})$	Standard deviation $mol/L\ (\times 10^{-4})$
2	-1.55	0.65
5	-3.36	0.90
10	-5.89	1.77
15	-10.60	0.00
30	-10.96	0.000

Table S2.13: The average change in the concentration of H⁺ ions in the cathode compartment of the plasma electrochemistry setup maintained at a consistent discharge current of 4 mA at previous research work done by Witzke et al., [1].

Exposure Time (Min)	The average experimental change in H^+ concentration $mol/L\ (\times 10^{-4})$	Standard deviation $mol/L\ (\times 10^{-4})$
2	-1.66	-3.32
5	-4.15	-8.29
10	-8.30	-16.58
15	-12.44	-24.88
30	-24.89	

Table S2.14: Calculated values for the expected change in H⁺ ions concentration in the cathode compartment of the plasma electrochemistry setup maintained at a consistent discharge current of 2 mA and 4 mA at previous research work done by Witzke et al., [1].

Exposure Time (Min)	Expected change in H^+ concentration $mol/L\ (\times 10^{-4})$ at 2.0 mA	Expected change in H^+ concentration $mol/L\ (\times 10^{-4})$ at 4.0 mA
2	1.66	3.32
5	4.15	8.29
10	8.3	16.58
15	12.44	24.88
30	24.89	

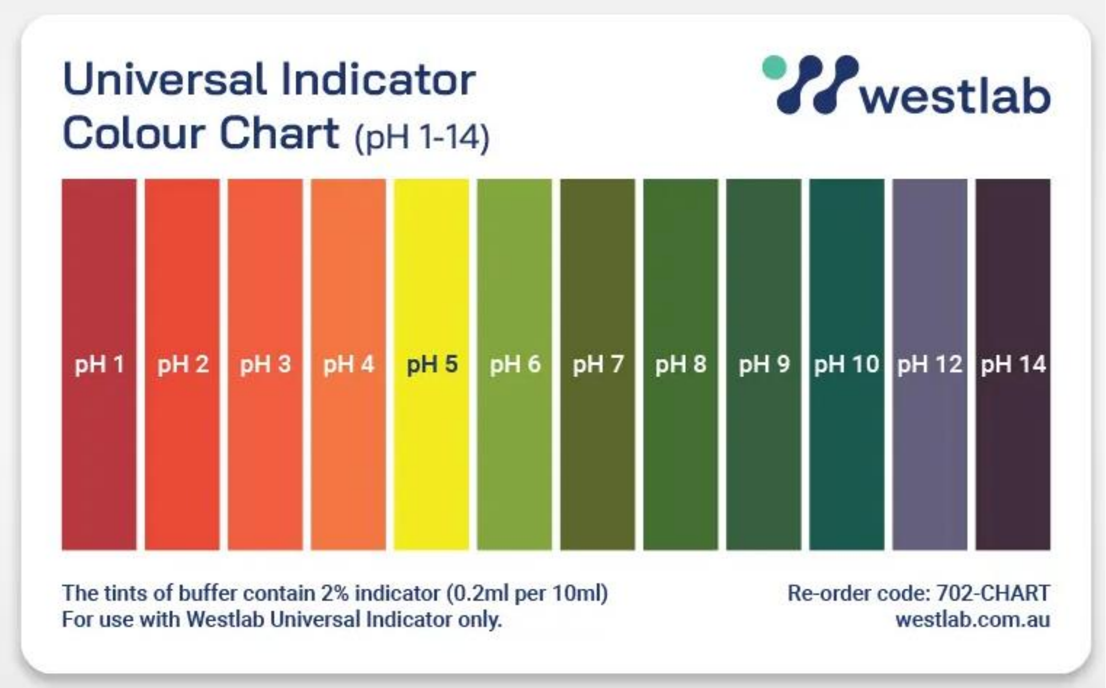

Universal Indicator Colour Chart (pH 1-14)

The tints of buffer contain 2% indicator (0.2ml per 10ml)
For use with Westlab Universal Indicator only.

Re-order code: 702-CHART
westlab.com.au

Figure S2.1 - Universal indicator colour chart

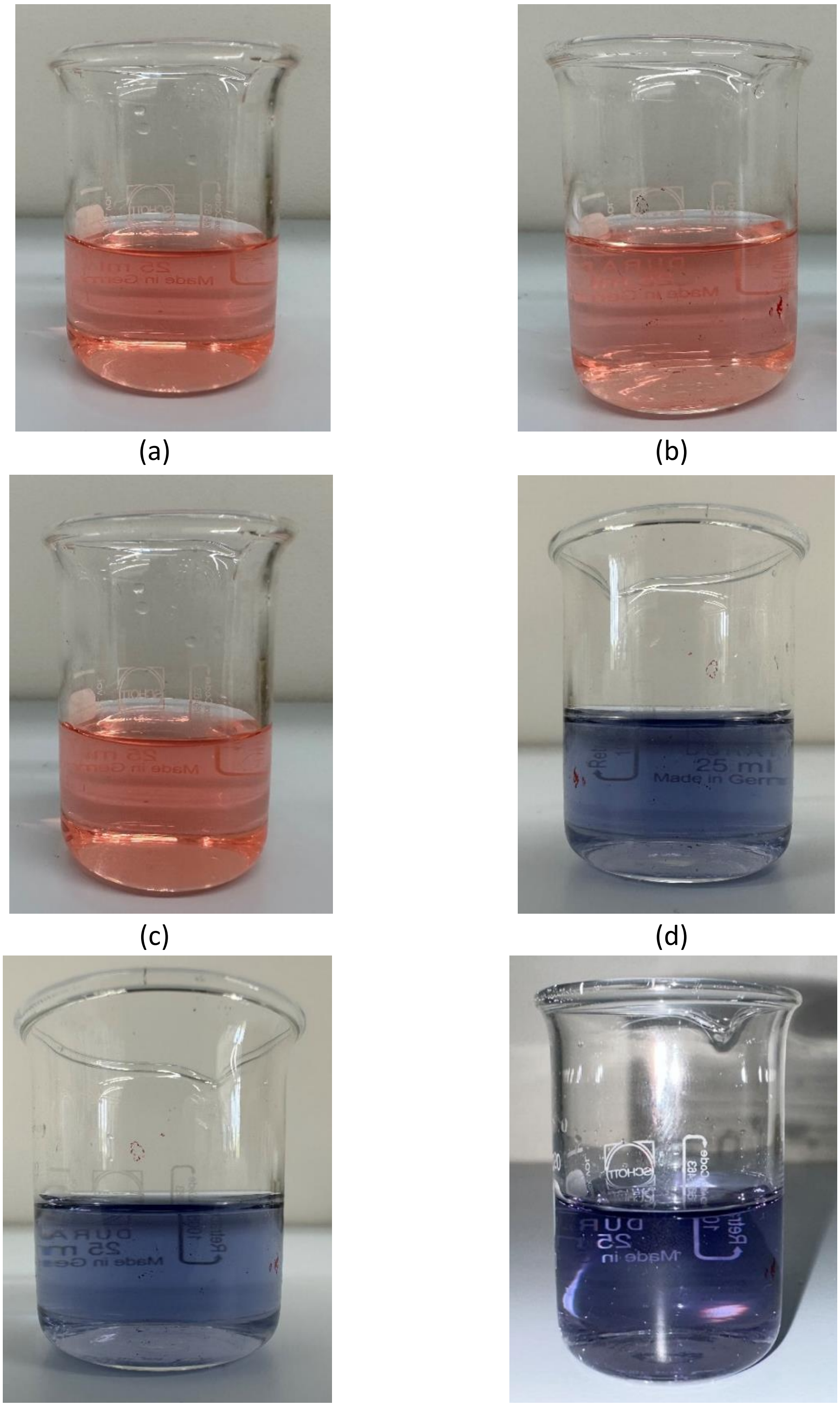

(a) (b)

(c) (d)

(e) (f)

Figure S2.2: A visual depiction of an electrolyte cathodic solution containing a pH-sensitive dye before and after the plasma treatment at different intervals. (a) before plasma treatment (b) t=2 mins, (c) t=5 mins , (d) t=10 mins, (e) t=15 mins and (f) t=30 mins.

APPENDIX B - SUPPLEMENTARY INFORMATION FOR CHAPTER 3

Table S3.1: Molecular weight distribution of polystyrene microplastics.

Treatment Condition	Mw (g/mol)			Average (g/mol)	Standard Deviation (g/mol)
	Trial 01	Trail 02	Trial 03		
Control	174103	172843	170369	172438.3	1899.61
NaCl 30 mins	151376	151367	150899	151214	272.84
NaCl 60 mins	149325	151043	148607	149658.3	1251.74
Na_2SO_4 30 mins	138421	136366	139938	138241.7	1792.74
Na_2SO_4 60 mins	128943	125025	131707	128558.3	3357.57

Table S3.2: PDI distribution of polystyrene microplastics.

Treatment Condition	PDI			Average	Standard Deviation
	Trial 01	Trail 02	Trial 03		
Control	2.56652	2.5788	2.4344	2.527	0.080
NaCl 30 mins	2.286	2.295	2.274	2.285	0.011
NaCl 60 mins	2.304	2.282	2.287	2.291	0.012
Na_2SO_4 30 mins	2.517	2.293	2.28	2.363	0.133
Na_2SO_4 60 mins	2.609	2.372	2.328	2.436	0.151

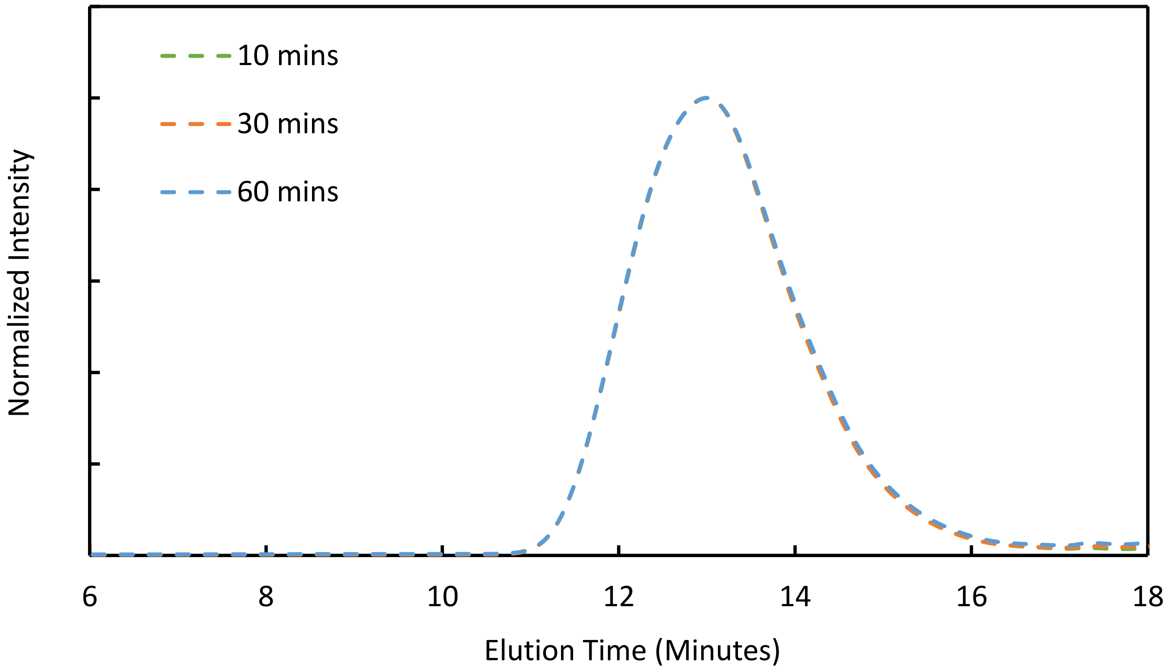

Figure S3.1: Gel permeation chromatography traces for PS treated under the following digestion conditions: 10 minutes, 30 minutes and 60 minutes with 0.6 M Sodium Chloride (NaCl).

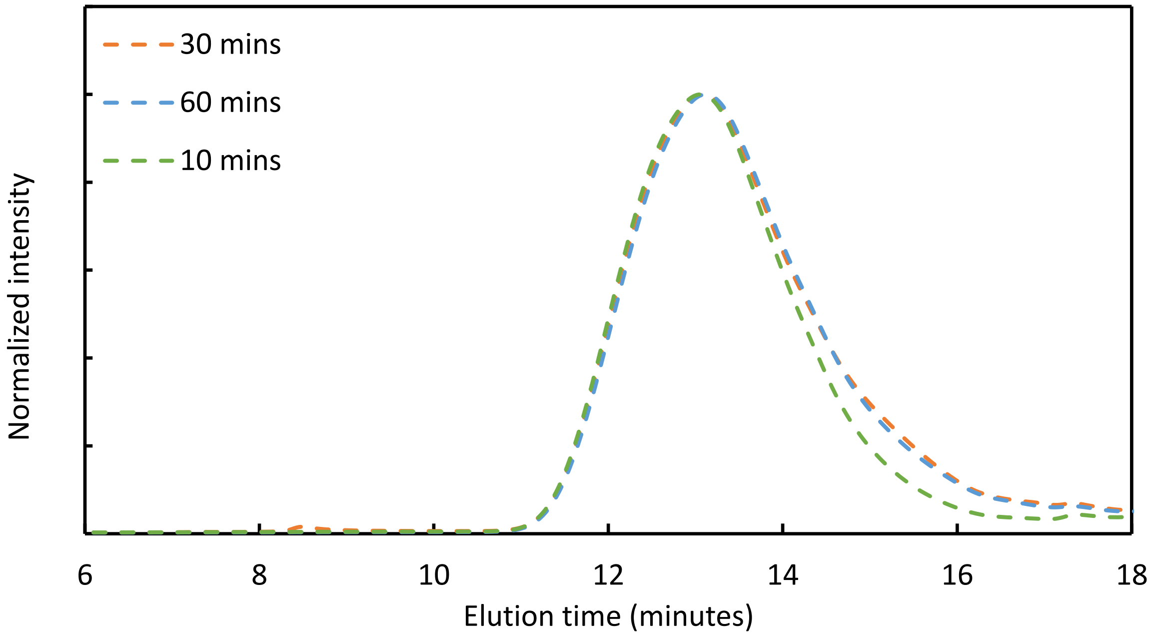

Figure S3.2: Gel permeation chromatography traces for PS treated under the following digestion conditions: 10 minutes, 30 minutes and 60 minutes with 0.3 M Sodium Sulphate (Na_2SO_4).

Figure S3.3 illustrates the FTIR spectra of pure PS MPs, specifically focusing on the high-frequency range spanning from 2700 to 3200 cm^{-1}. The high-frequency spectra of PS exhibit seven absorption bands. The peaks observed at 3001, 3024, 3059, 3081, and 3102 cm^{-1} correspond to the C-H stretching of benzene ring CH groups present in the PS side chain. The peaks at 2918 and 2847 cm^{-1} are also attributed to the CH_2 and CH groups' C-H stretching vibrations within the primary PS chain [200].

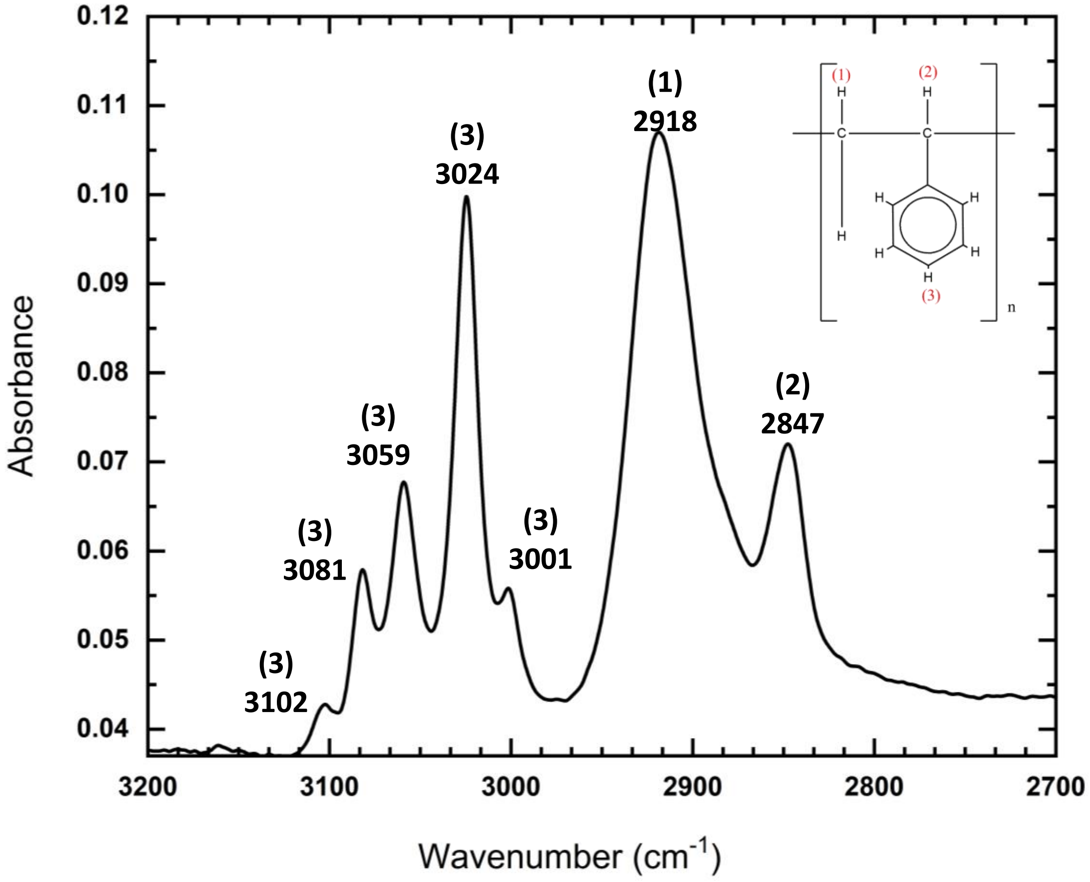

Figure S3.3: ATR-FTIR spectrum of PS in the high frequency: Peaks at 3001, 3024, 3059, 3081, and 3102 cm^{-1} correspond to the C-H stretching of benzene ring CH groups present in the PS side chain. The 2918 and 2847 cm^{-1} peaks are also attributed to the CH_2 and and CH groups' C-H stretching vibrations within the primary PS chain.

APPENDIX C - SUPPLEMENTARY INFORMATION FOR CHAPTER 4

```
      program latice
c
C     write(6,*)'HEADER ARGON LATICE'
C     write(6,*)'AUTHOR Kalpani Anuradha'
c
      character atnm*4,rsnm*4,lanm*4
      real x,y,z,r
      integer i,j,k,id,rid
c
      open(unit=20,file='ar.pdb',status='unknown')
c
      rid=1
      id=0
      r=3.6
      rsnm='Ar'
      atnm='Ar'
c
      do i=1,14
         x=(i-1)*r
         do j=1,14
            y=(j-1)*r
            do k=1,14
               z=(k-1)*r
               id=id+1
               write(20,500)id,rsnm,atnm,id,x,y,z,0.0,0.0
            end do
         end do
      end do
500   format('ATOM',3x,I4,2x,2A4,2x,I4,2x,3F8.3,2F6.2)
c
c
c
      end
```

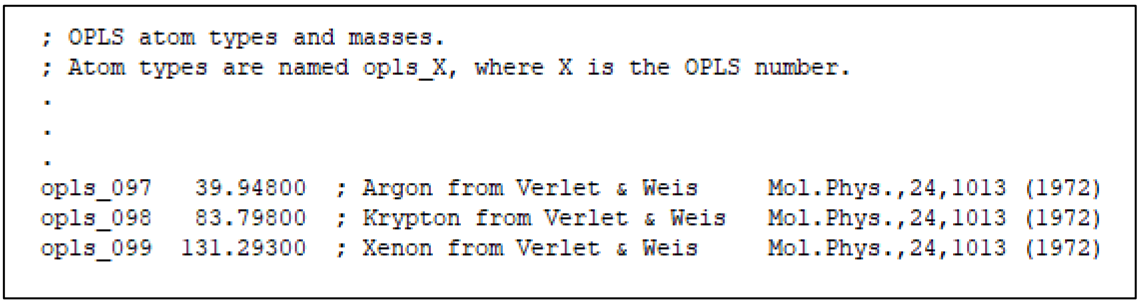

```
; OPLS atom types and masses.
; Atom types are named opls_X, where X is the OPLS number.
.
.
.
opls_097   39.94800  ; Argon from Verlet & Weis     Mol.Phys.,24,1013 (1972)
opls_098   83.79800  ; Krypton from Verlet & Weis   Mol.Phys.,24,1013 (1972)
opls_099  131.29300  ; Xenon from Verlet & Weis     Mol.Phys.,24,1013 (1972)
```

(a) atomtypes.atp

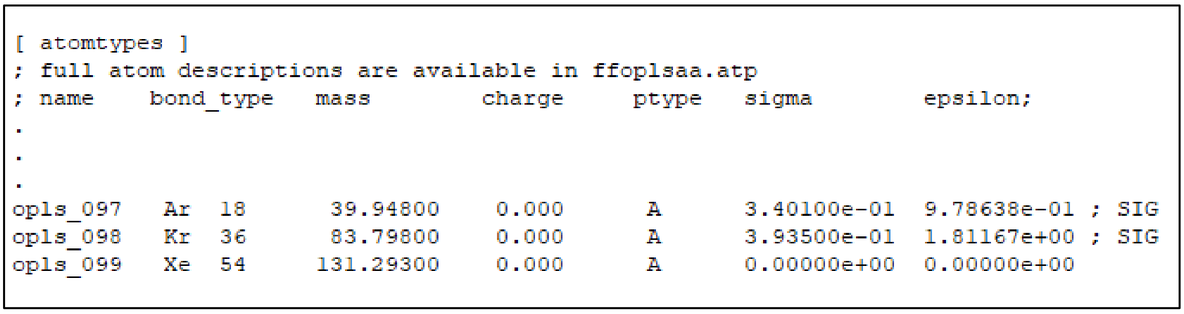

```
[ atomtypes ]
; full atom descriptions are available in ffoplsaa.atp
; name     bond_type   mass         charge     ptype   sigma         epsilon;
.
.
.
opls_097    Ar   18      39.94800    0.000       A      3.40100e-01  9.78638e-01 ; SIG
opls_098    Kr   36      83.79800    0.000       A      3.93500e-01  1.81167e+00 ; SIG
opls_099    Xe   54     131.29300    0.000       A      0.00000e+00  0.00000e+00
```

(b) ffnonbonded.itp

Figure S4.1: Extract of parameter files from the OPLS folder in GROMACS

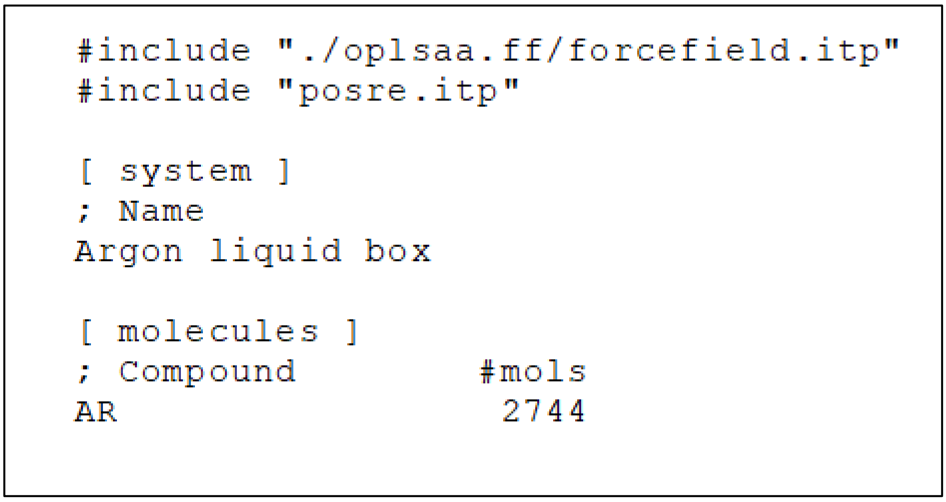

```
#include "./oplsaa.ff/forcefield.itp"
#include "posre.itp"

[ system ]
; Name
Argon liquid box

[ molecules ]
; Compound           #mols
AR                    2744
```

system.top

Figure S4.2: Topology (.top) file for liquid Ar

Sample parameter file (.mdp)

```
;
;    File 'mdout.mdp' was generated
;    By user: jc818833 (1413321852)
;    On host: ln02
;    At date: Mon Oct 24 09:32:04 2022
;
;    Created by:
;                 :-) GROMACS - gmx grompp, 2021.4-Ubuntu-2021.4-2 (-
:
;
;    Executable:   /usr/bin/gmx
;    Data prefix:  /usr
;    Working dir:  /home/jc818833/jc818833/research/24OCT_Ar85K
;    Command line:
;      gmx grompp -c eq01.pdb -f run01.mdp -n index.ndx -p system.top
-o run01.tpr -maxwarn 1

; VARIOUS PREPROCESSING OPTIONS
; Preprocessor information: use cpp syntax.
; e.g.: -I/home/joe/doe -I/home/mary/roe
include                  =
; e.g.: -DPOSRES -DFLEXIBLE (note these variable names are case
sensitive)
define                   =

; RUN CONTROL PARAMETERS
integrator               = md
; Start time and timestep in ps
tinit                    = 0
dt                       = 0.002
nsteps                   = 5000000
; For exact run continuation or redoing part of a run
init_step                = 0
; Part index is updated automatically on checkpointing (keeps files
separate)
simulation_part          = 1
; Multiple time-stepping
mts                      = no
; mode for center of mass motion removal
comm-mode                = Linear
; number of steps for center of mass motion removal
nstcomm                  = 1
; group(s) for center of mass motion removal
comm-grps                =

; LANGEVIN DYNAMICS OPTIONS
; Friction coefficient (amu/ps) and random seed
bd-fric                  = 0
ld-seed                  = 1993

; ENERGY MINIMIZATION OPTIONS
; Force tolerance and initial step-size
```

```
emtol                    = 10
emstep                   = 0.01
; Max number of iterations in relax-shells
niter                    = 20
; Step size (ps^2) for minimization of flexible constraints
fcstep                   = 0
; Frequency of steepest descents steps when doing CG
nstcgsteep               = 1000
nbfgscorr                = 10

; TEST PARTICLE INSERTION OPTIONS
rtpi                     = 0.05

; OUTPUT CONTROL OPTIONS
; Output frequency for coords (x), velocities (v) and forces (f)
nstxout                  = 500
nstvout                  = 0
nstfout                  = 0
; Output frequency for energies to log file and energy file
nstlog                   = 500
nstcalcenergy            = -1
nstenergy                = 500
; Output frequency and precision for .xtc file
nstxout-compressed       = 500
compressed-x-precision   = 1000
; This selects the subset of atoms for the compressed
; trajectory file. You can select multiple groups. By
; default, all atoms will be written.
compressed-x-grps        =
; Selection of energy groups
energygrps               = Ar

; NEIGHBORSEARCHING PARAMETERS
; cut-off scheme (Verlet: particle based cut-offs)
cutoff-scheme            = Verlet
; nblist update frequency
nstlist                  = 10
; Periodic boundary conditions: xyz, no, xy
pbc                      = xyz
periodic_molecules       = no
; Allowed energy error due to the Verlet buffer in kJ/mol/ps per atom,
; a value of -1 means: use rlist
verlet-buffer-tolerance  = 0.005
; nblist cut-off
rlist                    = 1.2
; long-range cut-off for switched potentials

; OPTIONS FOR ELECTROSTATICS AND VDW
; Method for doing electrostatics
coulombtype              = Cut-off
coulomb-modifier         = Potential-shift-Verlet
rcoulomb-switch          = 0
rcoulomb                 = 1.0
; Relative dielectric constant for the medium and the reaction field
epsilon_r                = 10000
```

```
epsilon_rf               = 1
; Method for doing Van der Waals
vdw-type                 = Cut-off
vdw-modifier             = Potential-shift-Verlet
; cut-off lengths
rvdw-switch              = 0
rvdw                     = 1.0
; Apply long range dispersion corrections for Energy and Pressure
DispCorr                 = No
; Extension of the potential lookup tables beyond the cut-off
table-extension          = 1
; Separate tables between energy group pairs
energygrp-table          =
; Spacing for the PME/PPPM FFT grid
fourierspacing           = 0.12
; FFT grid size, when a value is 0 fourierspacing will be used
fourier_nx               = 0
fourier_ny               = 0
fourier_nz               = 0
; EWALD/PME/PPPM parameters
pme_order                = 4
ewald_rtol               = 1e-05
ewald-rtol-lj            = 0.001
lj-pme-comb-rule         = Geometric
ewald_geometry           = 3d
epsilon_surface          = 0
implicit_solvent         = No

; OPTIONS FOR WEAK COUPLING ALGORITHMS
; Temperature coupling
Tcoupl                   = nose_hoover
nsttcouple               = -1
nh-chain-length          = 1
print-nose-hoover-chain-variables = no
; Groups to couple separately
tc-grps                  = Ar
; Time constant (ps) and reference temperature (K)
tau-t                    = 0.5
ref-t                    = 85
; pressure coupling
Pcoupl                   = Parrinello-Rahman
Pcoupltype               = Isotropic
nstpcouple               = -1
; Time constant (ps), compressibility (1/bar) and reference P (bar)
tau-p                    = 2.0
compressibility          = 4.5e-5
ref-p                    = 1.0
; Scaling of reference coordinates, No, All or COM
refcoord_scaling         = No

; OPTIONS FOR QMMM calculations
QMMM                     = no
; Groups treated with MiMiC
QMMM-grps                =
```

```
; SIMULATED ANNEALING
; Type of annealing for each temperature group (no/single/periodic)
annealing                =
; Number of time points to use for specifying annealing in each group
annealing-npoints        =
; List of times at the annealing points for each group
annealing-time           =
; Temp. at each annealing point, for each group.
annealing-temp           =

; GENERATE VELOCITIES FOR STARTUP RUN
gen_vel                  = yes
gen-temp                 = 85
gen-seed                 = 173529

; OPTIONS FOR BONDS
constraints              = none
; Type of constraint algorithm
constraint-algorithm     = Lincs
; Do not constrain the start configuration
continuation             = no
; Use successive overrelaxation to reduce the number of shake
iterations
Shake-SOR                = no
; Relative tolerance of shake
shake-tol                = 0.0001
; Highest order in the expansion of the constraint coupling matrix
lincs-order              = 4
; Number of iterations in the final step of LINCS. 1 is fine for
; normal simulations, but use 2 to conserve energy in NVE runs.
; For energy minimization with constraints it should be 4 to 8.
lincs-iter               = 1
; Lincs will write a warning to the stderr if in one step a bond
; rotates over more degrees than
lincs-warnangle          = 30
; Convert harmonic bonds to morse potentials
morse                    = no

; ENERGY GROUP EXCLUSIONS
; Pairs of energy groups for which all non-bonded interactions are
excluded
energygrp-excl           =

; WALLS
; Number of walls, type, atom types, densities and box-z scale factor
for Ewald
nwall                    = 0
wall_type                = 9-3
wall_r_linpot            = -1
wall-atomtype            =
wall-density             =
wall_ewald_zfac          = 3

; COM PULLING
pull                     = no
```

```
; AWH biasing
awh                      = no

; ENFORCED ROTATION
; Enforced rotation: No or Yes
rotation                 = no

; Group to display and/or manipulate in interactive MD session
IMD-group                =

; NMR refinement stuff
; Distance restraints type: No, Simple or Ensemble
disre                    = No
; Force weighting of pairs in one distance restraint: Conservative or
Equal
disre-weighting          = Conservative
; Use sqrt of the time averaged times the instantaneous violation
disre-mixed              = no
disre-fc                 = 1000
disre-tau                = 0
; Output frequency for pair distances to energy file
nstdisreout              = 100
; Orientation restraints: No or Yes
orire                    = no
; Orientation restraints force constant and tau for time averaging
orire-fc                 = 0
orire-tau                = 0
orire-fitgrp             =
; Output frequency for trace(SD) and S to energy file
nstorireout              = 100

; Free energy variables
free-energy              = no
couple-moltype           =
couple-lambda0           = vdw-q
couple-lambda1           = vdw-q
couple-intramol          = no
init-lambda              = 0
init-lambda-state        = -1
delta-lambda             = 0
nstdhdl                  = 10
fep-lambdas              =
mass-lambdas             =
coul-lambdas             =
vdw-lambdas              =
bonded-lambdas           =
restraint-lambdas        =
temperature-lambdas      =
calc-lambda-neighbors    = 1
init-lambda-weights      =
dhdl-print-energy        = no
sc-alpha                 = 0
sc-power                 = 0
sc-r-power               = 6
```

```
sc-sigma                 = 0.3
sc-coul                  = no
separate-dhdl-file       = yes
dhdl-derivatives         = yes
dh_hist_size             = 0
dh_hist_spacing          = 0.1

; Non-equilibrium MD stuff
acc-grps                 =
accelerate               =
freezegrps               =
freezedim                =
cos-acceleration         = 0
deform                   =

; simulated tempering variables
simulated-tempering      = no
simulated-tempering-scaling = geometric
sim-temp-low             = 300
sim-temp-high            = 300

; Ion/water position swapping for computational electrophysiology
setups
; Swap positions along direction: no, X, Y, Z
swapcoords               = no
adress                   = no

; User defined thingies
user1-grps               =
user2-grps               =
userint1                 = 0
userint2                 = 0
userint3                 = 0
userint4                 = 0
userreal1                = 0
userreal2                = 0
userreal3                = 0
userreal4                = 0
; Electric fields
; Format for electric-field-x, etc. is: four real variables:
; amplitude (V/nm), frequency omega (1/ps), time for the pulse peak
(ps),
; and sigma (ps) width of the pulse. Omega = 0 means static field,
; sigma = 0 means no pulse, leaving the field to be a cosine function.
electric-field-x         = 0 0 0 0
electric-field-y         = 0 0 0 0
electric-field-z         = 0 0 0 0

; Density guided simulation
density-guided-simulation-active = false
```

Table S4.1: Summary of file formats used in GROMACS MD simulation [205]

File type	**Description**
Structure files	
pdb	A molecular structure file following the Protein Data Bank (PDB) file format. This format serves to define the atomic positions within a molecular structure. The coordinates are extracted from the ATOM and HETATM records, extending until the file concludes or reaches an ENDMDL record. Notably, GROMACS software can read and write a simulation box within the CRYST1 entry of the pdb file. Moreover, the pdb format can also serve as a trajectory format, including multiple structures separated by ENDMDL, which can be read from or written to a single file. A pdb file should look like following;

```
ATOM    1  H1  LYS    1     14.260   6.590  34.480  1.00  0.00
ATOM    2  H2  LYS    1     13.760   5.000  34.340  1.00  0.00
ATOM    3  N   LYS    1     14.090   5.850  33.800  1.00  0.00
ATOM    4  H3  LYS    1     14.920   5.560  33.270  1.00  0.00
...
...
```

Parameter files	
mdp	Run parameter file, input for gmx grompp command. The beginning of APPENDIX B illustrates mdp files used in each step (energy minimization, equilibration and production run).
Topology files	
atp	The atp file provides essential atom type details, such as atom numbers and masses represented in atomic mass units.
itp	The extension "itp" stands for "Include Topology," and these files serve the purpose of being included in topology files, typically with the extension "top."

top	The file extension "top" is short for "topology." It serves as an ASCII file that is utilized by gmx grompp. When processed by gmx grompp, the "top" file is converted into a binary topology file known as "tpr.
ndx	The GROMACS index file is commonly named index.ndx allows users to define sets of atoms according to their preferences. This file can be read by various analysis programs and the preprocessor (gmx grompp). Many programs will generate default index groups without an index file. Hence, an index file is only necessary when custom groups are required. To define a group, the user writes its name enclosed in square brackets. The atom numbers corresponding to the group can be listed on multiple lines, and the numbering of atoms starts from 1.
Run input files	
tpr	The file extension "tpr" corresponds to a portable binary run input file. Within this file, you'll find the initial simulation structure, the molecular topology, and all the simulation parameters. It's important to note that due to its binary format, you cannot access the contents of this file using a standard text editor.
Trajectory files	
trr	Files bearing the ".trr" file extension store the trajectory data of a simulation. Inside this file, you'll find comprehensive data, including coordinates, velocities, forces, and energies, as specified in your mdp file using GROMACS. It's worth noting that this file employs a portable binary format and can be accessed using compatible tools or software.
xtc	The xtc format serves as a versatile trajectory data format. It utilizes the xdr routines designed for data read and write, initially developed for the Unix NFS system. The trajectory data is recorded with a precision reduction approach. Here's how it works: First, the coordinates (in nanometers) are multiplied by a scaling factor, typically set at 1000, to represent coordinates in picometers (pm). These are then rounded to integer values. Additional optimizations come into play, taking advantage of the tendency for atoms in close sequence

	to be physically close as well, such as in the case of a water molecule. For this purpose, the xdr library is expanded to include a specialized routine for recording 3-D float coordinates.
Energy files	
edr	The ".edr" file extension is used to denote a portable energy file. In this file, energy data is stored in accordance with the xdr protocol.
Other files	
xvg	Most of the output generated by GROMACS analysis tools is compatible with Grace, previously referred to as Xmgr. We choose to utilize Grace due to its high degree of flexibility and the fact that it is freely available software. It is capable of producing PostScript™ output, making it particularly well-suited for integration into various documents, including LaTeX files and other word processing applications.

The Lennard-Jones potential (V_{LJ}) between two atoms is defined as:

$$V_{LJ}(r_{ij}) = \frac{C_{ij}^{(12)}}{r_{ij}^{12}} - \frac{C_{ij}^{(6)}}{r_{ij}^{6}} \qquad \text{Equation S1.1}$$

In the equation 1.2 the parameters $C_{ij}^{(12)}$ and $C_{ij}^{(6)}$depend on pairs of atom types obtained from a matrix of LJ parameters. In the Verlet cut off scheme, the Lennard-Jones potential is adjusted by a constant value so that it becomes zero at the cut off distance. The force derived from the Lennard-Jones potential is obtained by taking the negative derivative of the potential concerning the distance between the atoms. The force expression is given by:

$$F_i(r_{ij}) = -\left(12\frac{C_{ij}^{(12)}}{r_{ij}^{13}} - 6\frac{C_{ij}^{(6)}}{r_{ij}^{7}}\right)\frac{r_{ij}}{r_{ij}} \qquad \text{Equation S1.2}$$

The Lennard-Jones potential can alternatively be expressed in the following form:

$$V_{LJ}(r_{ij}) = 4\varepsilon_{ij}\left(\left(\frac{\sigma_{ij}}{r_{ij}}\right)^{12} - \left(\frac{\sigma_{ij}}{r_{ij}}\right)^{6}\right) \qquad \text{Equation S1.3}$$

Where ϵ denotes the depth of the potential well, which indicates the strength of attraction between the particles, σ represents the distance at which the intermolecular potential becomes zero, serving as a measure of the closest approach between nonbonding particles known as the van der Waals radius. This radius is equivalent to half the distance between the centres of the nonbonding particles.

The GROMACS software was used to do the simulations, and more important details about this software can be found in Chapter 01. The set of non-bonded parameters includes van der Waals parameters V ($c6$ or σ, depending on the combination rule) and W ($c12$ or ϵ), specified in the file nonbonded.itp (APPENDIX C – Figure S4.2(b)) in the force field library for a given force field. Two combination rules can be used when creating the parameter matrix for the non-bonded LJ parameters in GROMACS.

For combination rule 1:

$$V_{ii} = C_i^{(6)} = 4\epsilon_i\sigma_i^6 \quad [kJ\ mol^{-1}\ nm^6] \qquad \text{Equation S1.4}$$

$$W_{ii} = C_i^{(12)} = 4\epsilon_i\sigma_i^{12} \quad [kJ\ mol^{-1}\ nm^{12}] \qquad \text{Equation S1.5}$$

For combination rules 2 and 3:

$$V_{ii} = \sigma_i \quad [nm] \qquad \text{Equation S1.6}$$

$$W_{ii} = \epsilon_i \quad [kJ\ mol^{-1}\ ] \qquad \text{Equation S1.7}$$

In the non-bonded parameter section, it is possible to provide some or all combinations for different atom types using the parameters *V* and *W* as defined earlier. If a specific combination is not provided, it will be calculated based on the parameters assigned to the corresponding atom types, following the combination rule. In GROMACS, the type 1 combination rule, which involves only geometric averages, can be specified in the input section of the force-field file as type 1:

$$C_{ij}^{(6)} = \left(C_{ii}^{(6)}C_{jj}^{(6)}\right)^{1/2} \qquad \text{Equation S1.8}$$

$$C_{ij}^{(12)} = \left(C_{ii}^{(12)}C_{jj}^{(12)}\right)^{1/2} \qquad \text{Equation S1.9}$$

Alternatively, the Lorentz-Berthelot rules can be employed when constructing the parameter matrix for non-bonded LJ parameters. In this case, an arithmetic average calculates the parameter σ, while a geometric average calculates the parameter ϵ (type 2 combination rule).

$$\sigma_{ij} = \frac{1}{2}\left(\sigma_{ii} + \sigma_{jj}\right) \qquad \text{Equation S1.10}$$

$$\epsilon_{ij} = \left(\varepsilon_{ii}\varepsilon_{jj}\right)^{1/2} \qquad \text{Equation S1.11}$$

The type 3 combination rule, which involves a geometric average for both parameters, is utilised explicitly by the OPLS (Optimised Potentials for Liquid Simulations) force field. The parameter ε (kJ/mol) represents the depth of the energy minimum, while the parameter σ

(nm) can be interpreted as the diameter specific to each atom. These parameters are established empirically using a combination of experimental data, first-principles physics, and fitting to quantum mechanical calculations [93,94].

The effectiveness of these parameters depends on the model systems being studied, and the appropriate force field must be chosen based on the specific application. For this thesis, the Optimized Potentials for Liquid Simulations All Atoms (OPLASS) and GROningen MOlecular Simulation (GROMOS) force fields were selected, which is an all-atom force field with point charges designed explicitly for liquid simulations [231].